POR Calabria
2014-2020
Fesr-Fse
il futuro è un lavoro quotidiano

UNIONE EUROPEA
FONDI STRUTTURALI E DI INVESTIMENTO EUROPEI

REPUBBLICA
ITALIANA

REGIONE
CALABRIA

UNIVERSITÀ
DELLA CALABRIA

Department of Civil Engineering

Doctoral Research in

Sciences and Engineering for the Environment, Construction, and Energy

Financed by "Programma Operativo Regionale Calabria FSE/FESR 2014 – 2020 (CCI 2014IT16M2OP006)"

Cycle XXXV

NUMERICAL MODELING OF FRACTURE PHENOMENA BY MEANS OF MOVING MESH METHOD

Academic/Scientific Sector
ICAR/08 – Structural Mechanics

Course Coordinator
Prof. Salvatore CRITELLI

Salvatore Critelli
26.06.2023 17:04:03
GMT+02:00

Scientific Supervisor
Prof. Paolo LONETTI

Paolo Lonetti
27.06.2023 08:56:23
GMT+01:00

Author
Dott. Domenico AMMENDOLEA

DOMENICO
AMMENDOLEA
27.06.2023 08:30:03
GMT+00:00

Abstract

In recent years, the impact of crack evolution on the bearing capacity of a structure has become one of the most important features in modern design processes to choose the best structural intervention, which must be as “sustainable” as possible both in terms of the materials used and from an economic point of view.

The important advances in computational fields have led to several numerical methods that can accurately reproduce crack propagation phenomena. Most of them have been developed in the framework of the Finite Element (FE) method because of its simplicity and flexibility in analyzing complex structures. Commonly, FE methods are classified into (*i*) smeared crack models and (*ii*) discrete crack approaches. Discrete crack approaches reproduce internal defects, including strain or discontinuity fields, into finite element formulations. In contrast, smeared crack models account for the presence of cracks at the constitutive level by using proper damage laws that degrade the mechanical properties of the material once crack conditions occur. Each method presents negative and positive features, thus denoting that it is somewhat challenging to find the best one. Developing advanced approaches ensuring a suitable compromise between low computational costs and reliable predictions is attracting considerable attention from national and international research communities.

The present thesis aims to develop a numerical model for reproducing crack propagation mechanisms in different structural components under generalized loading conditions. The proposed methodology combines the Moving Mesh (MM) technique and the Interaction integral method (M-integral) in an FE framework. In particular, based on the Arbitrary Lagrangian-Eulerian (ALE) formulation, the MM approach is used for tracing the variation in the geometry of the computational domain due to the crack advance. More precisely, the mesh node associated with the crack tip is moved consistently with the conditions dictated by classic fracture criteria developed in the context of Fracture Mechanics. To ensure the consistency of the mesh point's motion, the proposed strategy uses mesh regularization techniques based on proper rezoning equations. This feature drastically reduces the overall amount of re-meshing events, which typically affect the computational efficiency of standard crack propagation procedures, thereby saving relevant computational resources meanwhile avoiding convergence issues. Useful solutions to overcome the major issues of traditional FEM procedure for studying crack propagation mechanisms are much sought.

Another key aspect of the present thesis is a novel strategy for extracting fracture variables at the crack front, which are necessary for defining crack onset conditions, the direction of propagation, and the crack tip velocity. Specifically, the proposed model uses the M-integral method to extract Stress Intensity Factors (SIFs) at the crack front. In particular, in the framework of the MM strategy adopted, this work introduces the ALE formulation of the *M*-integral.

Comparisons with predictions of other numerical methodologies, analytical formulations, and, especially, experimental results are developed to check the reliability and efficacy of the proposed method. In this context, parametric analyses regarding mesh discretization and parameters involved in the numerical model serve to assess the computational efficiency and accuracy in predicting fracture variables and crack trajectories. The results show that the proposed approach is an efficient and robust and numerical tool for reproducing complex crack propagation phenomena.

The thesis is organized as follows: chapter 1 contains the introduction, which reports a brief literature review on the fracture phenomena and modeling approaches, the aims and scope. Chapters 2 and 3 present the developed method in a static framework. In particular, chapter 2 depicts the theoretical formulation, the numerical implementation, and the computational procedure, while chapter 3 shows numerical results to assess the proposed strategy's reliability and efficacy. Chapter 4 generalizes the proposed modeling approach to the context of dynamic Fracture Mechanics. Finally, chapter 5 outlines the conclusions and future perspectives of this work.

Abstract (Italian version)

Negli ultimi anni, l'impatto dell'evoluzione delle fessure sulle capacità operative di una struttura è diventato uno degli aspetti inderogabili nei moderni processi di progettazione, al fine di scegliere il miglior intervento strutturale, il quale deve essere il più possibile "sostenibile" sia in termini di materiali utilizzati che dal punto di vista economico.

I notevoli progressi nel campo computazionale hanno consentito lo sviluppo di numerosi metodi numerici in grado di riprodurre accuratamente i fenomeni di propagazione delle fessure. Alcuni di essi sono stati elaborati nell'ambito del Metodo degli Elementi Finiti (MEF) grazie alla sua capacità e flessibilità nel modellare geometrie complesse.

In generale, i modelli agli elementi finiti sono classificati in approcci discreti e modelli "smeared crack". Gli approcci discreti riproducono i difetti interni, inclusi i campi di deformazione o discontinuità nelle formulazioni degli elementi finiti. Al contrario, i modelli "smeared crack" tengono conto della presenza delle fessure a livello costitutivo adottando appropriate leggi di danno, che degradano le proprietà meccaniche del materiale una volta che si verificano le condizioni di propagazione. Ogni metodo presenta vantaggi e svantaggi, denotando così una certa difficoltà nell'individuare il migliore. Lo sviluppo di approcci avanzati che garantiscano un adeguato compromesso tra bassi costi computazionali e previsioni accurate sta attirando l'attenzione da parte della comunità di ricerca nazionale ed internazionale.

La presente tesi ha l'obiettivo di sviluppare un modello numerico per riprodurre i meccanismi di propagazione delle fessure in diversi componenti strutturali in condizioni di carico generali. La metodologia proposta combina la tecnica delle Mesh Mobili (MM) e il metodo dell'Interaction Integral (*M*-integral) nell'ambito degli Elementi Finiti (EF). In particolare, l'approccio MM, basato sulla formulazione Arbitraria Lagrangiana-Euleriana (ALE), è adottato per descrivere l'evoluzione della geometria del dominio computazionale a seguito dell'avanzamento della cricca. Più precisamente, il nodo della mesh associato all'apice del difetto viene spostato coerentemente alle condizioni imposte dai classici criteri di frattura sviluppati nell'ambito della Meccanica della Frattura. La strategia elaborata utilizza tecniche di regolarizzazione della mesh, basate su opportune equazioni di riorganizzazione, per garantire la conformità del movimento dei nodi della mesh. Questa caratteristica riduce drasticamente il ricorso ad azioni di re-mesh, che tipicamente influiscono sull'efficienza computazionale delle procedure standard di propagazione delle fessure, risparmiando così oneri computazionali ed allo stesso tempo vengono evitati problemi di convergenza. Infatti, si cercano soluzioni utili per superare i principali problemi delle procedure FEM tradizionali nello studio dei fenomeni di propagazione.

Un altro aspetto chiave della presente tesi è l’utilizzo di una nuova strategia per estrarre le variabili di frattura all’apice del difetto, i quali sono necessari per definire le condizioni di innesco della cricca, la direzione di propagazione e la velocità dell’apice della fessura. In particolare, il modello proposto adotta il metodo dell’M-integral per estrarre gli Stress Intensity Factors (SIFs) all’apice del difetto. Nell’ambito della strategia MM adottata, questo lavoro introduce la formulazione ALE dell’M-integral.

L’affidabilità e l’efficacia del modello elaborato viene verificata attraverso confronti con le previsioni di altre metodologie numeriche, le soluzioni analitiche ed i risultati sperimentali. Inoltre, per valutare l’efficienza e l’accuratezza di calcolo nella previsione delle variabili di frattura e il percorso delle fessure, vengono sviluppate delle analisi parametriche in funzione della configurazione della mesh e dei parametri coinvolti nel modello numerico. I risultati mostrano come l’approccio proposto sia uno strumento numerico robusto ed efficiente in grado di riprodurre complessi fenomeni di propagazione delle fessure.

La tesi è organizzata come segue: il capitolo 1 contiene l’introduzione, una breve rassegna della letteratura sui fenomeni di frattura e gli approcci di modellazione, gli obbiettivi e lo scopo. I capitoli 2 e 3 presentano il modello elaborato in ambito statico. In particolare, il capitolo 2 spiega la formulazione teorica, l’implementazione numerica e la procedura di calcolo, mentre il capitolo 3 mostra i risultati numerici ottenuti per valutare la sua affidabilità ed efficacia. Il capitolo 4 generalizza il metodo proposto in ambito dinamico. Infine, il capitolo 5 presenta le conclusioni e le prospettive future di questo lavoro.

List of Figures

List of Tables

Contents

1

INTRODUCTION

The prevention and assessment of damage and fracture processes inside material components represent a fundamental tool in the dimensioning of engineering constructions to ensure their technical safety and durability. The sudden fracture, technically named “brittle fracture”, is the most dangerous type of damage which may cause catastrophic collapses of civil constructions like civil buildings or bridges (Figure 1.1). Sudden failures can also induce severe consequences for the life of people, the environment, and even the economy. In several materials and engineering components, defects may result from manufacturing or op-

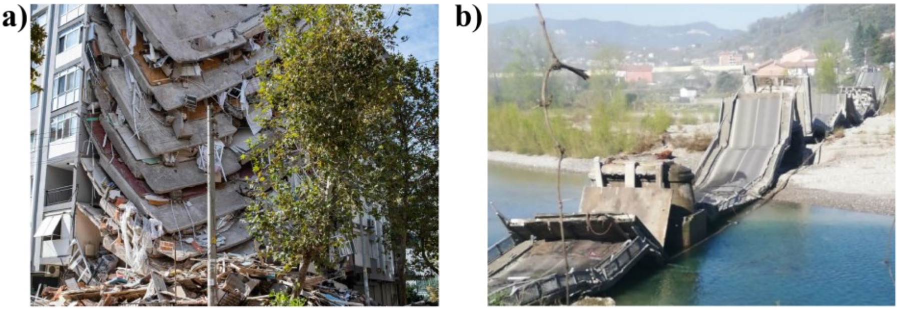

Figure 1.1. Catastrophic collapse of civil construction: (a) civil building in Turkey; (b) bridge in Albiano - Italy.

eration, which, unfortunately, cannot be avoided. Therefore, it is imperative to assess crack-life defects fracture mechanically. In the past years, the study of fracture mechanics has become an independent interdisciplinary scientific field that defines load parameters and criteria so that crack behavior can be quantified under static, dynamic, or cycling loading in homogeneous and heterogeneous materials.

1.1 Fracture phenomena

Quasi-brittle materials (*i.e.,* concrete, ceramic, glass fiber composites, etc.) are part of numerous key components commonly used in civil engineering structures because they possess high resistance against aggressive natural agents and extraordinary durability. Instead, they are highly vulnerable to mechanical actions induced by dynamic loadings (*i.e.,* seismic vibrations, wind forces, impact by foreign objects, etc.). Indeed, the unavoidable and preexisting material defects expand under dynamic loads via dangerous crack propagation mechanisms, thus com-

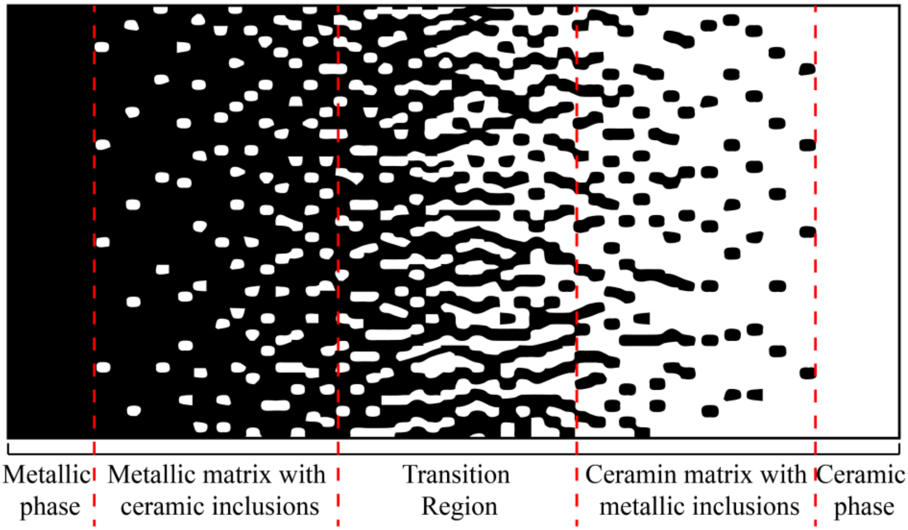

Figure 1.2. Example of Functionally Graded Materials (FGMs).

promising the overall material's integrity. Moreover, both cycling loading and, especially, high-temperature gradients serve as leading causes of extreme failure. Therefore, investigating thermo-mechanical-induced fractures helps limit safety hazards.

In addition, a novel class of composites (Figure 1.2), the Functionally Graded Materials (FGMs), are a receiving growing interest from the structural engineering fields (Shen, 2009). FGMs are multiphase materials mainly composed of two phases (usually one metal and the other ceramic) linked together to produce a smooth variable volume fraction along specific design directions (Cherradi et al., 1994). In particular, the metallic component increases material strength, while the ceramic part enhances its thermal properties. The graded macro-properties avoid material interfaces, reducing local stress concentrations.

Unfortunately, the ceramic phase makes FGMs vulnerable to brittle fracture mechanisms. In particular, the growth of a pre-existing crack inside an FGM material is a complex phenomenon since material heterogeneity influences the stress fields around the crack tip and, inevitably, the crack trajectory.

Technically, the fracture phenomenon is an irreversible process and it represents the culmination of a mechanical degradation action that produces the formation of new surfaces. It is necessary to use the principles of Fracture Mechanics to predict such a phenomenon. In the literature, Linear-Elastic Fracture Mechanics (LEFM) and Elastic-Plastic Fracture Mechanics (EPFM) are the main theories employed to investigate the fracture behavior in cracked solids.

The LEFM, originated by Griffith, is applicable to any material in which the inelastic deformation and the nonlinear effects are limited in a vanishingly small region at the crack tip (Bazant and Planas, 1998). Indeed, the stresses near the crack tip are so high that some kind of inelasticity must occur in the immediate proximity of the crack tip. This area can be neglected if the inelastic zone is small compared to the crack size or the component dimensions, thus verifying LEFM exactly.

The EPFM theory, also known as ductile Fracture Mechanics, overcomes the drawbacks of LEFM. It is adopted to determine the crack problem solution in materials, where the extent of inelastic deformation is large enough that it cannot be neglected.

There are three crack propagation modes depending on the applied load type: Mode I, Mode II, and Mode III (Figure 1.3). In Mode I, the

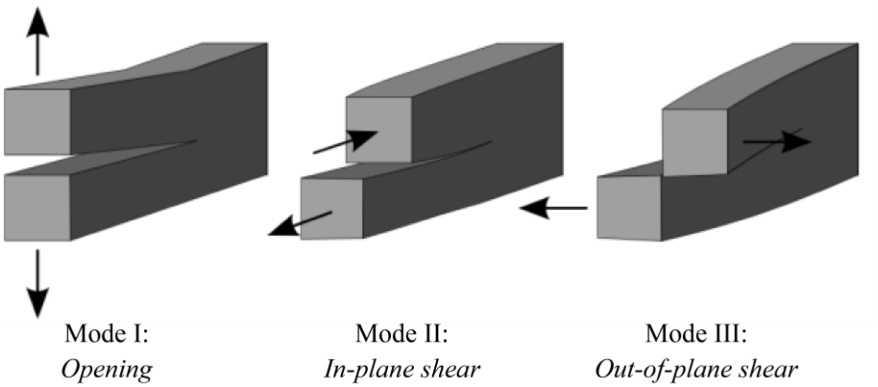

Figure 1.3. Fracture modes: Mode I (*opening*), Mode II (*in-plane shear*), and Mode III (*out-of-plane shear*).

fracture plane is perpendicular to the applied force. In Mode II, the fracture takes place under the action of shear stress and propagates in its direction. Finally, in Mode III, the fracture occurs by shear mode again, but it propagates in its direction perpendicular. In most cases, Mode I and Mode II, or a combination of them (called Mixed-Mode), are considered only, while Mode III is neglected.

Usually, in static conditions, the crack tip propagation occurs once a factor considering the stress state exceeds a critical threshold value. The latter represents the fracture toughness of the material. Instead, under dynamic conditions, the crack initiation process and the consequent propagation are more complex than what occurs in quasi-static circumstances (Barretta et al., 2015). Indeed, the crack tip advances unstably according to jumpy movements, involving sequences of crack initiation, fast propagation, and crack arrest events. This occurs because the material's fracture dynamic behavior is characterized by different critical threshold values, which become rate-dependent for high loading rates. In this context, inertia effects are significant, especially when the load changes abruptly. Finally, due to suddenly applied dynamic loading, stress waves spread across the material and notably influence the stress and strain fields near the crack tip region. Therefore, to assess the integrity of the structural components under dynamic loadings, it is fundamental to adopt proper analysis strategies able to account for all the above complexities and, further, capable of providing exhaustive information regarding the crack initiation conditions, the direction of crack propagation, and the velocity of dynamically advancing crack fronts. Within this framework, choosing an accurate and highly efficient numerical approach for investigating crack propagation phenomena is essential.

1.2 Overview of modeling approaches

The first approaches developed for simulating fracture mechanics have been analytical ((Sih, 1962), (Freund, 1990), (Tomlinson and Olden, 1999), (Anderson and Anderson, 2005)). These models are useful for analyzing problems with somewhat simple geometries and loading conditions. However, such analytical formulations are inapplicable to real structures because of their complexity of the geometries and loading conditions. For these cases, numerical simulations are certainly more suitable.

Recent advances in computational fields, in terms of hardware and software, have permitted the development of many innovative methods to reproduce crack propagation phenomena. Such methods are often classified into two main groups: smeared crack and discrete approaches.

Smeared crack models simulate the presence of internal discontinuities by adopting appropriate constitutive laws. In contrast, discrete modeling approaches reproduce internal cracks by including strain or displacement discontinuity fields into standard Finite Element (FE) formulations.

In the context of discrete approaches, the Finite Element Method (FEM) is one of the most widely used numerical modeling methods due to its ability and flexibility in replicating complex geometries (Tilbrook et al., 2006). It dates back to the early 1960s ((Clough, 1960)). The general principle of FEM is to divide the computational domain of the investigated problem into smaller sub-domains usually called finite elements. Such a subdivision is called space discretization, which results in constructing a computational mesh. Within each finite element, an approximate solution to the problem is formulated by expressing the field of the primary variable as the product of nodal values (i.e., the values of the primary variables at the node of the finite element) and approximated functions. To find the values that the primary variable assumes at each node of the computational mesh, the simple equations that model each finite element are assembled into a larger system of equations that models the entire problem. Once completed, the global system of equations is solved.

FEM has excellent robustness in dealing with problems like material heterogeneity, non-linear deformability, complex boundary conditions, etc. ((Kim and Paulino, 2004a), (Tilbrook et al., 2005), (Steigemann et al., 2010)). However, two fundamental drawbacks make it relatively inefficient. Firstly, dense meshes are needed close to the crack tip to approximate the stress fields' singularity. The second concerns the use of remeshing processes to trace the growth of arbitrarily growing cracks. Even if advanced algorithms manage remeshing automatically, the process requires considerable computer effort, thus spending significant computational time. Moreover, the transition from old to new mesh configurations may result in loss of accuracy issues, thus compromising the numerical solution’s reliability.

To overcome these difficulties, as an alternative to classical FE approaches, procedures based on advanced formulations are proposed in the context of the Extended Finite Element Method (X-FEM) and the Cohesive Zone Modeling (CZM). The CZM is an inter-element approach that can investigate quasi-static (Jin et al., 2002) and dynamic (KANDULA et al., 2005) crack propagation processes. This technique is suitable for analyzing fracture problems with crack paths known as a priori (for example, the delamination phenomena (Greco and Lonetti, 2009)). Instead, it involves a lot of complexity when the crack trajectories are unknown in advance. In addition, softening-based constitutive laws of interface elements cause non-convergence issues in numerical computation.

The research group of Belytschko proposed the Extended Finite Element Method (X-FEM) in 1999 (Belytschko and Black, 1999). The XFEM is an intra-element approach that enhances standard FEM formulation through special finite elements embedding discontinuous shape functions, which allow a precise representation of crack paths and singularity fields near crack tips ((Moës and Belytschko, 2002), (Menouillard and Belytschko, 2010), (Bayesteh and Mohammadi, 2013)). In this context, the crack trajectories are mesh-independent because discontinuities develop within the elements. Moreover, X-FEM avoids remeshing events in each step of the propagation. However, complications may occur in formulating finite elements and performing numerical integration. Using enriched shape functions naturally adds extra degrees of freedom to the governing equations of the problem. Especially in quasi-brittle materials and dynamic conditions, this feature may lead to numerical difficulties when multiple cracks originate and propagate (for example, the crack branching phenomenon). Finally, these methodologies require finer mesh discretization for the computational domain to handle random growing cracks, thus involving considerable computational resources to perform numerical simulations. This inconvenience implies that X-FEM strategies may be unpracticable with larger and articulated geometries.

As an alternative to FEM, the Boundary Element Method (BEM) and meshless approaches are usually employed, which are developed to either reduce or delete mesh discretization problems.

The Boundary Element Method (BEM) has been proposed since the late 1970s (Cheng and Cheng, 2005). The BEM transforms the basic governing equations of the computational domain into boundary integral equations and then it solves the corresponding algebraic relationships by discretizing only the boundary of the domain. Indeed, it is only necessary to arrange mesh nodes on the boundaries and crack surfaces for simulating the propagation process (Prasad et al., 1996). The BEM provides considerable computational savings because of the simplicity of re-meshing procedures. It is more suitable for solving problems of homogeneous and linearly elastic bodies only because it requires calculating Green’s functions. In contrast, it poses difficulties in solving numerical problems characterized by the presence of material heterogeneity, nonlinear material behavior, and damage evolution process.

Meshless methods (*i.e.,* the Particle Difference Method (PDM) (Lee et al., 2016), Element-Free Galerkin Method (PDM) (Belytschko and Tabbara, 1996), and the Cracking-Particle Method (CPM) (Rabczuk et al., 2010)) represent the computational domain as scattered nodes. Crack propagation processes takes place by simply moving the internal nodes (Bouhala et al., 2012). Although meshless methods avoid the recourse to re-meshing events and permit reproducing arbitrarily growing cracks with extraordinary versatility, the accuracy of numerical solutions depends on the number of computational nodes employed. Indeed, acceptable solutions need highly dense point clouds. Such a requirement makes these methods computationally expensive to perform numerical simulations of crack propagation problems characterized by complex crack trajectories, thus limiting their operative range to simple and relatively small geometries.

During the last decade, several attempts have been made to develop hybrid methodologies, which combine the advantages of two or more traditional approaches while minimizing their drawbacks as far as possible. Most of them assume the FEM as the basic method of the combination due to its user-friendliness and widespread use. For instance, the Scaled Boundary Finite Element Method (SB-FEM), developed by Ooi et al. (Ooi et al., 2013), combines the flexibility of the FEM in terms of handling complex geometric configurations and the computational efficiency of the BEM to manage remeshing procedures, which remain necessary for crack propagation simulations.

Other hybrid approaches enhance standard procedures through innovative numerical techniques. For instance, there are effective FE-based models that use the Moving Mesh (MM) technique ((Ponthot and Belytschko, 1998), (Koh et al., 1988)) to reproduce the propagation of a pre-existing crack. The MM is a powerful numerical technique that allows the movement of the mesh nodes of the computational domain as a function of some parameters, which can be unrelated to the investigated problem's mechanics. Consequently, a new mesh need not be generated for each domain configuration because the position of the mesh nodes changes consistently with geometry variations. In the MM context, the Arbitrary Lagrangian-Eulerian (ALE) formulation permits relocating the mesh nodes with great regularity and low computational honors. Due to this feature, it ensures reduced element distortions and, more interesting, it reduces the overall amount of remeshing events required to run the numerical analysis, thus saving computational resource, and making the approach more competitive than others. Finally, recent research works have implemented the ALE with success to reproduce crack propagation in homogeneous materials and delamination phenomena in composite structures ((Funari et al., 2018b), (Funari et al., 2018a)).

Regardless of the numerical methodology employed for simulating crack propagation phenomena, a key aspect of any numerical method regards the efficiency in extracting fracture variables at the crack front (*i.e.,* the Stress Intensity Factors (SIFs) and T-stress). In particular, the SIFS are fundamental to defining crack onset conditions, propagation direction, and, generally, crack tip velocity under mixed-mode loading conditions. In addition, the accuracy of the fracture variables is essential to predict reliable crack trajectories. One of the most used methods to extract SIFs is the Interaction Integral Method (also known as the *M*-integral method), proposed for the first time by Yau et al. (Yau et al., 1980) because of its simplicity and accuracy.

1.3 Aims, scope, and outline

The crack growth phenomena appear in several materials used in the most common civil engineering structures. They affect both the stiffness and the strength of the material itself. The knowledge of the failure behavior of a structural component is an essential aspect concerning key factors such as performance, reliability, and safety.

In recent years, the impact of crack evolution on the bearing capacity of a structure has become one of the most important features in modern design processes in both national and international contexts to identify optimal structural reinforcement strategies, which must be as "sustainable" as possible both from an economic point of view and, above all, in terms of the materials used. This requirement has produced a growing interest in developing numerical modeling techniques for simulating crack propagation phenomena inside commonly used materials.

Numerical simulations represent an efficient tool for scientific research since they allow to examine the complexities of physical phenomenon while simultaneously saving considerable economic resources. Unfortunately, most of numerical models reported in the literature have high computational costs.

Within this framework, the present thesis aims to develop a novel FE modeling strategy that combines the Moving Mesh (MM) Technique, based on the Arbitrary Lagrangian-Eulerian (ALE) formulation and the Interaction Integral Method for simulating crack propagation mechanisms in various structural components of civil engineering applications, made by homogeneous and heterogeneous materials, under general load conditions.

After the introduction, the rest of the thesis is organized as follows.

Chapter 2 presents the developed method in a static context. In particular, the first part of the chapter depicts an overview of the theoretical formulation of the proposed modeling approach, which contains the governing equations of the fracture mechanism problem, including the ALE formulation and the M-integral method. The second part describes the numerical implementation and the computational procedure that the proposed strategy uses for reproducing the propagation process.

Chapter 3 reports numerical results to assess the present methodology's reliability and efficacy through comparisons with experimental and numerical data reported in the scientific literature. At first, it analyzes coupled thermos-mechanical problems, but also purely mechanical or thermal ones. Next, it examines various numerical examples of mixed-mode crack propagation in two-dimensional structures made of Functionally Graded Materials (FGMs).

Chapter 4 generalizes the modeling approach presented in chapter 2 to the context of dynamic Fracture Mechanics for simulating crack propagation phenomena in quasi-brittle materials.

Finally, chapter 5 summarizes the main conclusions of the present thesis, together with some future perspectives of this work.

2

A coupled ALE – Interaction Integral formulation for static fracture analysis

The following chapter presents the main theoretical concepts employed to define the proposed model under quasi-static loading conditions. The first part reports an overview of the fundamental equations of the Fracture Mechanics, followed by a detailed description of the ALE formulation, in which the principles and equations governing the kinematic of the computational mesh are reported. Then, the M-integral method for extracting fracture variables at the crack front is presented. To this end, the ALE formulation of the M-integral is derived, which permits extracting fracture variables from a movable crack front. Finally, numerical implementation aspects are examined. The proposed modeling is presented without generality for a two-dimensional linear elastic continuum media. However, the presentation is quite general to be easily extended to three-dimensional problems.

2.1 Fundamental equations of the thermo-mechanical problem

Consider a two-dimensional cracked solid domain $\Omega \subset R^2$ made up of homogeneous or functionally graded materials, bounded by a contour $\Gamma = \Gamma_u \cup \Gamma_t = \Gamma_q \cup \Gamma_T$ (with $\Gamma_u \cap \Gamma_t = \Gamma_q \cap \Gamma_T = \varnothing$), in which Dirichlet and Neumann conditions are imposed (Figure 2.1). In particular, Γ_t and Γ_q are boundary portions of Γ where tractions $\mathbf{t}$ and heat flux $\mathbf{q}$ are imposed, while Γ_u and Γ_T part of Γ where displacements $\mathbf{u}$ and temperature $\mathbf{T}$ act. The solid presents an internal crack Γ_C that departs from the external boundary and develops up to a crack front C_T. In particular, C_T serves as the origin of a local system of coordinates (x_1, x_2), whose horizontal axis x_1 is tangent to the crack faces. Under the hypothesis of small strains and absence of interaction force between the crack faces, the governing equations of the problem are:

$$\begin{gathered}
\nabla \cdot \boldsymbol{\sigma} + \mathbf{f} = 0, \quad \forall P(\mathbf{X}) \in \Omega \\
\boldsymbol{\sigma} = \mathbf{C} : (\boldsymbol{\varepsilon} - \boldsymbol{\varepsilon}_{\mathrm{T}}) \\
\boldsymbol{\varepsilon} = \nabla^{sym} \mathbf{u} \\
\boldsymbol{\varepsilon}_{\mathrm{T}} = \alpha (T - T_0) \mathbf{I}
\end{gathered} \tag{2.1}$$

$$\begin{gathered}
-\nabla \cdot \mathbf{q} + \bar{Q} = 0, \quad \forall P(\mathbf{X}) \in \Omega \\
\mathbf{q} = -k \nabla T
\end{gathered} \tag{2.2}$$

Eqs. (2.1) are equilibrium, constitutive, and compatibly equations, while Eqs. (2.2) govern the heat transfer problem. In Eqs. (2.1), $\mathbf{f}$ is the

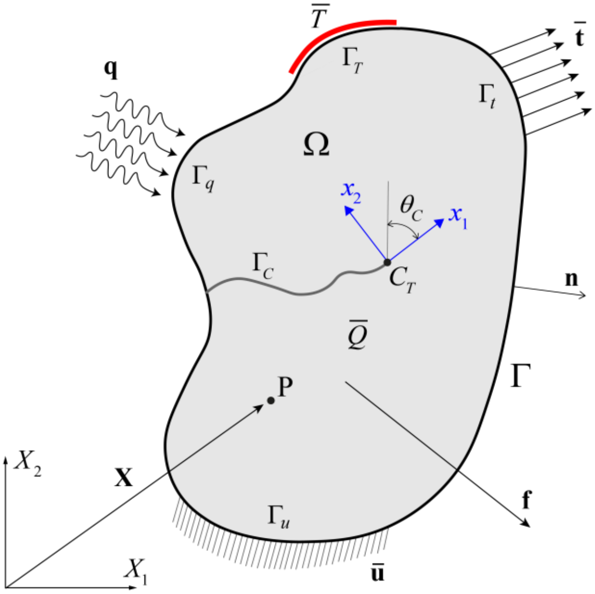

Figure 2.1. A two-dimensional domain with an initial pre-crack.

body force vector, $\boldsymbol{\sigma} = \boldsymbol{\sigma}(\mathbf{X})$ is the Cauchy stress tensor ($\mathbf{X}$ is the position vector), $\boldsymbol{\varepsilon}$ and $\boldsymbol{\varepsilon}_{\mathbf{T}}$ are the total and thermal strain tensors, $\mathbf{C}$ is the elastic tensor, $\mathbf{u}$ and T are the displacements and temperature fields, α is the coefficient of thermal expansion, T_o is the reference temperature, and $\mathbf{I}$ is the second-order identity tensor. In Eqs. (2.2), $\mathbf{q}$, $\bar{Q}$, and k represent the heat flux vector, the inner body heat source, and the thermal conductivity, respectively. Governing equations can be re-written by combining Eqs. (2.1) and Eqs. (2.2), as follows:

$$\nabla \cdot \left[\mathbf{C} : \left(\nabla^{sym} \mathbf{u} - \alpha \left(T - T_0 \right) \mathbf{I} \right) \right] + \mathbf{f} = \mathbf{0} \tag{2.3}$$

$$-\nabla \cdot \left(-k \nabla T \right) + \bar{Q} = 0 \tag{2.4}$$

Eq. (2.3) and Eq. (2.4) must be solved under the following Dirichlet and Neumann boundaries conditions:

$$\begin{aligned}&\mathbf{u}=\bar{\mathbf{u}} \quad \text{on } \Gamma_u\\&\mathbf{C}:\left(\nabla^{sym}\mathbf{u}-\alpha\left(T-T_0\right)\mathbf{I}\right)\cdot\mathbf{n}=\bar{\mathbf{t}} \quad \text{on } \Gamma_t\\&T=\bar{T} \quad \text{on } \Gamma_T\\&-k\nabla T\cdot\mathbf{n}=\bar{q} \quad \text{on } \Gamma_q\end{aligned} \tag{2.5}$$

where, $\mathbf{n}$ is the unit outward normal to Γ.

If the temperature field T is equal to zero, Eq. (2.4) cancels and Eq. (2.3) and Eqs. (2.5) become:

$$\nabla\cdot\left[\mathbf{C}:\left(\nabla^{sym}\mathbf{u}\right)\right]+\mathbf{f}=\mathbf{0} \tag{2.6}$$

$$\begin{aligned}&\mathbf{u}=\bar{\mathbf{u}} \quad \text{on } \Gamma_u\\&\mathbf{C}:\left(\nabla^{sym}\mathbf{u}\right)\cdot\mathbf{n}=\bar{\mathbf{t}} \quad \text{on } \Gamma_t\end{aligned} \tag{2.7}$$

In addition, for Functionally Graded Materials (FGMs), material properties like Young's modulus $E\left(\mathbf{X}\right)$, Poisson's ratio $\nu\left(\mathbf{X}\right)$, density $\rho\left(\mathbf{X}\right)$, and fracture toughness $K_{IC}\left(\mathbf{X}\right)$ are spatially varying.

The governing equations regarding mechanical field can be stated also through the following weak variational form:

$$-\int_{\Omega}\mathbf{C}:\left(\nabla^{sym}\mathbf{u}-\boldsymbol{\varepsilon}_{\mathbf{T}}\right)\cdot\nabla\delta\mathbf{u}\,d\Omega+\int_{\Omega}\mathbf{f}\cdot\delta\mathbf{u}\,d\Omega+\int_{\Gamma_t}\bar{\mathbf{t}}\cdot\delta\mathbf{u}\,d\Gamma=0 \tag{2.8}$$

In Eq. (2.8), $\mathbf{u}$ and $\delta\mathbf{u}$ represent the displacement field and a proper set of virtual displacements defined as:

$$\begin{aligned}&\mathbf{u}=\left\{\mathbf{u}\in H^1\left(\Omega\right)\middle|\,\mathbf{u}=\bar{\mathbf{u}} \text{ on } \Gamma_u\right\}\\&\delta\mathbf{u}=\left\{\delta\mathbf{u}\in H^1\left(\Omega\right)\middle|\,\delta\mathbf{u}=0 \text{ on } \Gamma_u\right\}\end{aligned} \tag{2.9}$$

Where, H^1 and $\bar{\mathbf{u}}$ are the Sobolev space and the prescribed displacement on Γ_u, respectively.

Similarly to the governing equations for solid mechanics, the weak form associated with the thermal problem can be stated as follows:

$$-\int_{\Omega} \left(-k\nabla T\right)\cdot \delta T \, d\Omega + \int_{\Omega} \bar{Q}\cdot \delta T \, d\Omega + \int_{\Gamma_q} \bar{q}\cdot \delta T \, d\Gamma = 0 \tag{2.10}$$

where, T and δT are the temperature field and the set of virtual temperatures, respectively, defined through the following expressions:

$$\begin{aligned} T &= \left\{ T \in H^1\left(\Omega\right) \middle| T = \bar{T} \text{ on } \Gamma_T \right\} \\ \delta T &= \left\{ \delta T \in H^1\left(\Omega\right) \middle| \delta T = 0 \text{ on } \Gamma_T \right\} \end{aligned} \tag{2.11}$$

Fracture Mechanics introduces additional equations aimed at evaluating crack growth phenomena in terms of crack onset circumstances and the direction of propagation. Since the fracture problem is crack-path dependent and crack trajectories are unknown in advance, all the equations should be expressed in an incremental form. To this end, the proposed method adopts a quasi-static rate-independent model, expressed through the following Karush-Kuhn-Tucker (KKT) conditions:

$$\begin{aligned} &\dot{\eta}_F \geq 0 \\ &f_F\left[K_I, K_{II}, \theta_c, K_C\left(\mathbf{X}\right)\right] \leq 0 \\ &\theta_c = k_F\left(K_I, K_{II}\right) \\ &f_F \dot{\eta}_F = 0 \end{aligned} \tag{2.12}$$

where, $\dot{\eta}_F$ represents the incremental crack tip displacements, f_F is a fracture function defined upon the mixed-mode Stress Intensity Factors (SIFs) K_I and K_{II}, and $K_C\left(\mathbf{X}\right)$ is the material fracture toughness. It is worth noting that K_C is constant for a homogeneous material, while it is spatially varying for FGMs because of heterogeneity. Furthermore,

θ_c is the kinking angle concerning the crack tip coordinate system (x_1, x_2), defined through a kinking function k_F. The fracture and kinking functions can be defined by adopting standard fracture criteria, such as the maximum hoop stress proposed by Erdogan and Sin (Erdogan and Sih, 1963) or the maximum energy release rate defined by Hussain et al. (Hussain et al., 1974). Note that the present model is quite general to work with any fracture criteria. Finally, an accurate evaluation of the SIFs is necessary at each crack tip displacement increment to define f_F and k_F, and, then, $\dot{\eta}_F$ and θ_c. To this aim, the proposed method uses the *M*-integral method because of its simplicity and accuracy.

2.2 Fundamentals of the Arbitrary Lagrangian-Eulerian (ALE) formulation

Continuum mechanics problems are generally analyzed using either a Lagrangian or a Eulerian approach.

Lagrangian approaches are formulated in a material system of coordinates (R_X), in which the material coordinate $\mathbf{X}$ identifies the *i*-th material particles of the continuum. Such approaches fix the mesh grid to the continuum, and the finite elements distort while the continuum deforms. Lagrangian approaches are practical for accurately analyzing the behavior of free surfaces or interfaces between different materials. However, when massive material deformations affect the continuum, the finite elements suffer from excessive deformations, thus causing loss of accuracy issues in numerical solutions.

On the other hand, Eulerian approaches are formulated in a spatial system of coordinates (R_x), in which the $\mathbf{x}$ coordinate identifies the spatial positions occupied by the material particles of the continuum over time. Such approaches adopt a fixed mesh and investigate the behavior of the continuum while it passes through the computational grid. For this reason, Eulerian approaches are more suitable than Lagrangian ones for analyzing the behavior of continuums affected by considerable distortions (*e.g.*, fluids). However, their weakness relies on the impossibility of accurately tracking the behavior of free surfaces or interfaces between different materials.

The ALE formulation combines the advantages of the Lagrangian and Eulerian approaches, reducing their leading drawbacks as far as possible. The ALE formulation introduces a third coordinate system R_χ (named mesh or referential coordinate system), in which the $\boldsymbol{\chi}$ coordinates represent the computational mesh nodes. This system has twofold fundamental properties: (*i*) it can move liberally into space according to specific conditions that may not be related to the mechanics of the investigated problem; (*ii*) it can move independently from material particles. Note that R_x and R_χ coincide at the beginning of the numerical simulation and R_χ can differ from R_X. The proposed approach adopts a Moving Mesh (MM) technique based on the ALE formulation to reproduce the evolution of geometry of the computational domain because of growing cracks. More precisely, the key idea is to represent the geometry variation produced by the crack advance by moving computational mesh points accordingly ((Ammendolea et al., 2021), (Greco

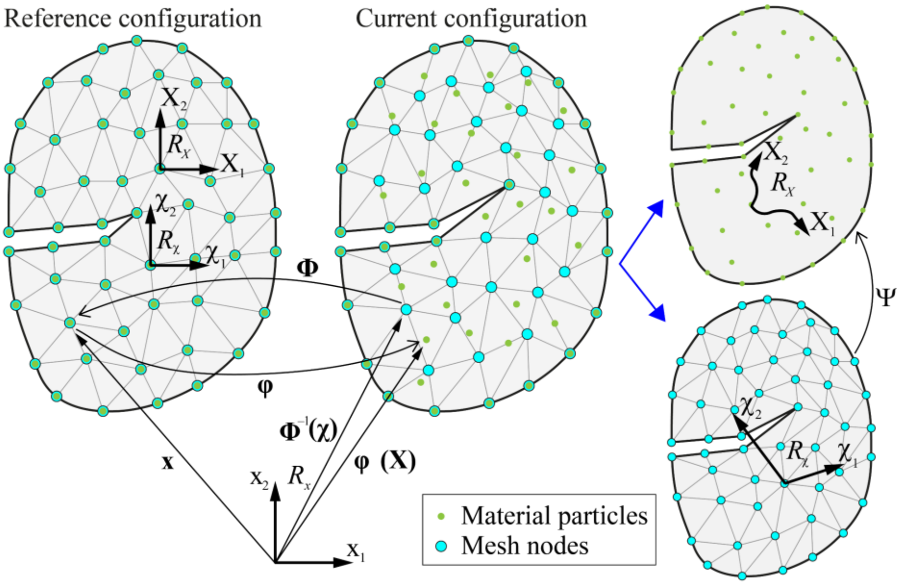

Figure 2.2. The Arbitrary Lagrangian-Eulerian formulation: relationships between Spatial, Material and Referential system of coordinates.

et al., 2021)). The ALE ensures large flexibility in moving the computational frame according to specific conditions. In the proposed modeling, the crack tip node is moved according to the fracture mechanics conditions defined by Eqs. (2.12). As a result, remeshing actions are limited and the computational efforts are strongly reduced.

Figure 2.2 shows how the proposed model uses the ALE formulation to reproduce the crack advance. Besides, it reports the relationship between the spatial, material, and referential frames. As one can see, the internal defects grow by passing from the reference to the current configuration, and the computational mesh adapts accordingly. In addition, according to the ALE formulation, material particles move differently from mesh nodes.

The links between the referential (R_χ), spatial (R_x), and materials (R_X) frames are expressed through proper bijective mapping functions. Specifically, $\boldsymbol{\varphi}(\mathbf{X})$ is the mapping function between the material and spatial domains and it describes the motion of particles in space. $\boldsymbol{\Phi}(\boldsymbol{\chi})$ links the referential and spatial domains and it describes the motion of the nodes of the computational mesh in space. Finally, $\boldsymbol{\Psi}(\boldsymbol{\chi})$ is the mapping function between referential and material frames. These functions are defined as follows:

$$\begin{aligned} \boldsymbol{\varphi} : R_X \to R_x \quad &\Big|\quad \mathbf{X} \mapsto \boldsymbol{\varphi}(\mathbf{X}) = \mathbf{x} \\ \boldsymbol{\Phi} : R_\chi \to R_x \quad &\Big|\quad \boldsymbol{\chi} \mapsto \boldsymbol{\Phi}(\boldsymbol{\chi}) = \mathbf{x} \\ \boldsymbol{\Psi} : R_\chi \to R_X \quad &\Big|\quad \boldsymbol{\chi} \mapsto \boldsymbol{\Psi}(\boldsymbol{\chi}) = \mathbf{X} \end{aligned} \tag{2.13}$$

Since the mesh changes during crack propagation, the governing equations of the structural problem and those associated with the heat transfer problem should be stated in the referential configuration. To this end, it is necessary to connect the gradient of vectorial fields in material and referential frames. Let a generic vectorial field be described through $\mathbf{v}^M(\mathbf{X})$ and $\mathbf{v}^R(\boldsymbol{\chi})$, in the material (M) and referential (R) domains, respectively. The gradient of $\mathbf{v}^M(\mathbf{X})$ in material domain can be expressed in the referential coordinates by performing spatial differencing of $\mathbf{v}^M(\mathbf{X}) = \mathbf{v}^R[\boldsymbol{\Psi}(\boldsymbol{\chi})]$:

$$\nabla^M \mathbf{v}^M = \frac{\partial \mathbf{v}^M}{\partial \mathbf{X}} = \frac{\partial \mathbf{v}^R}{\partial \boldsymbol{\chi}} \frac{\partial \boldsymbol{\chi}}{\partial \boldsymbol{\Psi}} = \nabla^R \mathbf{v}^R \mathbf{J}_{\boldsymbol{\Psi}}^{-1} \tag{2.14}$$

where, $\nabla^M(\cdot) = \partial(\cdot)/\partial\mathbf{X}$, $\nabla^R(\cdot) = \partial(\cdot)/\partial\boldsymbol{\chi}$, and $\mathbf{J}_{\boldsymbol{\Psi}}$ is the Jacobian matrix defined as: $\mathbf{J}_{\boldsymbol{\Psi}} = \partial\boldsymbol{\Psi}(\boldsymbol{\chi})/\partial\boldsymbol{\chi}$. From a mathematical point of view, the bijection condition of $\boldsymbol{\Psi}$ guarantees that the determinant of $\mathbf{J}_{\boldsymbol{\Psi}}$ is positive. At this point, Eq. (2.3) and Eq. (2.4) can be re-formulated in the referential frame as follows:

$$\begin{gathered}
\nabla^M \cdot \left[\mathbf{C}\left(\mathbf{X^M}\right) : \left[\nabla^{R,sym}\mathbf{u}\left(\mathbf{X^R}\right)\mathbf{J}_{\boldsymbol{\Psi}}^{-1} - \alpha\left[T\left(\mathbf{X^M}\right) - T_0\right]\mathbf{I}\right]\right] + \mathbf{f}\left(\mathbf{X^M}\right) = 0 \\
\mathbf{u}\left(\mathbf{X^M}\right) = \bar{\mathbf{u}} \quad \text{on} \quad \Gamma_u \\
\mathbf{C}\left(\mathbf{X^M}\right) : \left[\nabla^{R,sym}\mathbf{u}\left(\mathbf{X^R}\right)\mathbf{J}_{\boldsymbol{\Psi}}^{-1} - \alpha\left[T\left(\mathbf{X^M}\right) - T_0\right]\mathbf{I}\right] \cdot \mathbf{n} = \bar{\mathbf{t}} \quad \text{on} \quad \Gamma_t
\end{gathered} \tag{2.15}$$

$$\begin{gathered}
-\nabla^M \cdot \left[-k\nabla^R\left[T\left(\mathbf{X^R}\right)\right]\mathbf{J}_{\boldsymbol{\Psi}}^{-1}\right] + \bar{Q} = 0 \\
T(\mathbf{X^M}) = \bar{T} \quad \text{on} \quad \Gamma_T \\
-k\nabla^R\left[T\left(\mathbf{X^R}\right)\right]\mathbf{J}_{\boldsymbol{\Psi}}^{-1} \cdot \mathbf{n} = \bar{q} \quad \text{on} \quad \Gamma_q
\end{gathered} \tag{2.16}$$

Also, the weak form for solid mechanics and heat transfer can be re-written in the current frame, thus achieving the following formulae:

$$\begin{aligned}
&-\int_{\Omega_R}\left[\mathbf{C}\left(\mathbf{X^M}\right) : \left[\nabla^{R,sym}\mathbf{u}\left(\mathbf{X^R}\right)\mathbf{J}_{\boldsymbol{\Psi}}^{-1} - \boldsymbol{\varepsilon}_{\mathbf{T}}\left(\mathbf{X^M}\right)\right]\right]\left[\nabla^R\delta\mathbf{u}\left(\mathbf{X^R}\right)\mathbf{J}_{\boldsymbol{\Psi}}^{-1}\right]\bar{J}_\Omega d\Omega_R + \\
&+\int_{\Omega_R}\mathbf{f}\left(\mathbf{X^M}\right)\delta\mathbf{u^M}\bar{J}_\Omega d\Omega_R + \int_{\Gamma_t^R}\bar{\mathbf{t}}\left(\mathbf{X^M}\right)\cdot\mathbf{n}\delta\mathbf{u^M}\bar{J}_\Gamma d\Gamma_t = 0
\end{aligned} \tag{2.17}$$

$$\begin{aligned}
&\int_{\Omega_R}\left[-k\nabla^R\left[T\left(\mathbf{X^R}\right)\right]\mathbf{J}_{\boldsymbol{\Psi}}^{-1}\right]\left[\nabla^R\left(\delta T\right)\mathbf{J}_{\boldsymbol{\Psi}}^{-1}\right]\bar{J}_\Omega d\Omega_R + \\
&\qquad -\int_{\Omega_R}\bar{Q}\left(\mathbf{X^M}\right)\delta T\,\bar{J}_\Omega d\Omega_R - \int_{\Gamma_q^R}\mathbf{q}\left(\mathbf{X^M}\right)\mathbf{n}\delta T\,\bar{J}_\Gamma d\Gamma_q = 0
\end{aligned} \tag{2.18}$$

where, Ω_R, Γ_t^R and Γ_q^R are the area and the boundary of the body subjected to external and heat flux in the referential configuration, while

$\bar{J}_{\Omega}$ and $\bar{J}_{\Gamma}$ are the Jacobian related to the area and boundary, respectively.

In addition, further equations are introduced to smoothly deform the computational mesh consistently with the growth of internal defects while avoiding excessive distortions for finite elements. Indeed, the latter affects the accuracy of numerical results and requests for remeshing processes. These equations are consistent with rezoning or smoothing approaches based on Laplace (or Poisson) method. The Laplacian rezoning consists of solving the following partial differential equation within the computational domain:

$$\nabla^{M} \cdot \nabla^{M} \mathbf{x} = 0 \quad \text{on} \quad \Omega \tag{2.19}$$

where, $\mathbf{x} = [x_1 \quad x_2]$ is the vector position identifying the spatial coordinates of mesh nodes in the current configuration. Eq. (2.19) is solved with a proper set of boundary conditions to ensure that the mesh nodes move consistently with the evolution of internal discontinues, avoiding displacements on the external boundaries Γ:

$$\begin{aligned} \bar{\mathbf{x}} \cdot \mathbf{n}_{\mathbf{c}} &= \dot{\eta}_{\mathbf{F}} \quad \text{at} \quad C_T \\ \bar{\mathbf{x}} &= 0 \quad \text{on} \quad \Gamma \end{aligned} \tag{2.20}$$

where, $\bar{\mathbf{x}} = \mathbf{x} - \mathbf{X}$ is the nodal mesh displacement vector function, in which the material coordinates $\mathbf{X}$ are intended to be representative of the initial position of the mesh nodes; $\mathbf{n}_{\mathbf{c}}$ is the unit vector identifying the direction of crack propagation concerning the crack tip local system (x_1, x_2). Note that, the first condition of Eq. (2.20) imposes that the crack tip mesh node grows along the direction of crack propagation with an increment $\dot{\eta}_{\mathbf{F}}$, which derives from Eq. (2.12).

The weak form of the smoothing problem (Eq. (2.19)) is expressed as follows:

$$\int_{\Omega_R} \left[\nabla^R(\mathbf{x})\mathbf{J}_{\Psi}^{-1}\right]\left[\nabla^R(\delta\mathbf{x})\mathbf{J}_{\Psi}^{-1}\right]\bar{J}_{\Omega}\,d\Omega_R = 0 \tag{2.21}$$

Eq. (2.21) is based on the following set of the position vector field in the varied configuration and the corresponding weighting functions:

$$\begin{aligned} \mathbf{x} &= \left\{\mathbf{x} \in H^1(\Omega) \middle| \mathbf{x} = \mathbf{X} \text{ on } \Gamma\right\} \\ \delta\mathbf{x} &= \left\{\delta\mathbf{x} \in H^1(\Omega) \middle| \delta\mathbf{x} = 0 \text{ on } \Gamma\right\} \end{aligned} \tag{2.22}$$

Eq. (2.21) is completed by constraint conditions relative to the displacements of the crack tip and mesh nodes of the external boundary (Eq. (2.20)), which are introduced by means of the Lagrangian Multipliers Method (LMM), as follows:

$$\begin{aligned} &\int_{\Omega_R} \left[\nabla^R(\mathbf{x})\mathbf{J}_{\Psi}^{-1}\right]\cdot\left[\nabla^R(\delta\mathbf{x})\mathbf{J}_{\Psi}^{-1}\right]\bar{J}_{\Omega}\,d\Omega_R + \\ &\quad +\left[\delta(\boldsymbol{\lambda}\cdot\mathbf{n}_c)(\bar{\mathbf{x}}\cdot\mathbf{n}_c - \dot{\eta}_F) + (\boldsymbol{\lambda}\cdot\mathbf{n}_c)\,\delta(\bar{\mathbf{x}}\cdot\mathbf{n}_c)\right]_{\mathbf{X}=\mathbf{X}_{C_T}} + \\ &\qquad + \int_{\Gamma^R} \left[\delta(\boldsymbol{\lambda})\cdot\bar{\mathbf{x}} + \boldsymbol{\lambda}\cdot\delta(\bar{\mathbf{x}})\right]\bar{J}_{\Gamma}\,d\Gamma_R = 0 \end{aligned} \tag{2.23}$$

in which $\boldsymbol{\lambda}$ represents the LMM vector.

2.3 The ALE formulation of M-integral

The proposed approach adopts the interaction integral (*M*-integral) method to extract fracture variables at the crack front (i.e., the mixed-mode Stress Intensity Factors (SIFs)) because of its simplicity and accuracy. The *M*-integral arises from the *J*-integral applied to a superimposed field formed by two independent equilibrium states. The first are the displacement, stress, and strain fields corresponding to the problem under investigation, referred to as the actual (act) state ($\mathbf{u}^{act}, \boldsymbol{\varepsilon}^{act}, \boldsymbol{\sigma}^{act}$), for which the SIFs would be evaluated. The second is an auxiliary (aux) state consisting of displacement, stress, and strain fields ($\mathbf{u}^{aux}, \boldsymbol{\varepsilon}^{aux}, \boldsymbol{\sigma}^{aux}$) with known SIFs, usually obtained, for instance, from Williams' crack tip asymptotic solutions ($O\left(r^{1/2}\right)$ for the displacements and $O\left(r^{-1/2}\right)$ for stresses and strains). To derive the *M*-integral, let us consider the standard *J*-integral expression given as:

$$J = \int_{S_0} \left(W\delta_{1i} - \sigma_{ij} u_{j,1} \right) n_i dS + \int_{A_0} \beta \varepsilon_{ii} \frac{\partial T}{\partial x_1} dA \qquad \text{with } i, j = 1, 2 \tag{2.24}$$

where, W is the elastic strain energy defined as:

$$W = \frac{1}{2}\left(\sigma_{ij}\varepsilon_{ij} - \beta T \varepsilon_{ii} \right) \quad \text{with} \quad \beta = \begin{cases} \dfrac{E\alpha}{1-\nu} & \text{(plane stress)} \\ \dfrac{E\alpha}{1-2\nu} & \text{(plane strain)} \end{cases} \tag{2.25}$$

in which *E* is the Young's Modulus, ν is the Poisson's ratio, and α is the coefficient of thermal expansion. In Eq. (2.24) A_0 is the area enclosed by an arbitrary path S_0 surrounding the crack tip, δ_{ij} is the Kronecker delta, T is the temperature field, and n_i is the unit outward normal vector to S_0 (see Figure 2.3).

To improve the numerical calculation of Eq. (2.24) , the curvilinear integral is usually converted into an Equivalent Domain Integral (EDI) through the following three steps: first, constructing a closed path

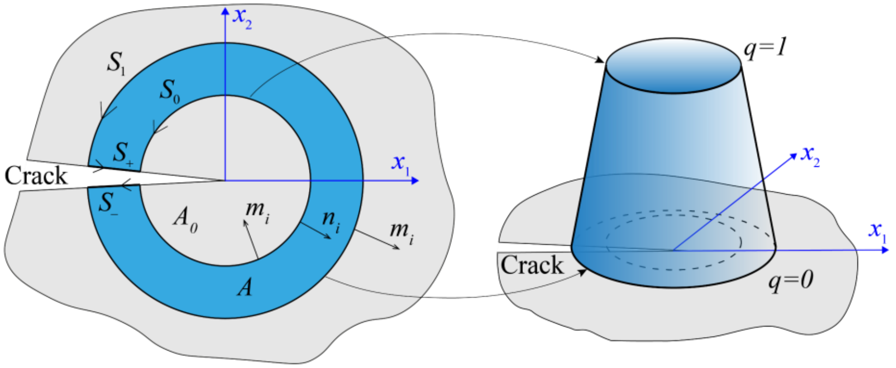

Figure 2.3. *J*-integral in the Equivalent Domain Integral (EDI) form with a schematic representation of the arbitrary function $q(x_1,x_2)$.

$S = S_1 + S_+ + S_- - S_0$, where S_1 is another closed contour surrounding S_0, and S_+, S_- are crack face paths. Then, integrating over S the integrand expression multiplied by a weighting function $q(x_1, x_2)$, which is equal to the unity on S_0 and zero on S_1 (Figure 2.3). In the absence of crack-face tractions and body forces, it occurs the following equivalence:

$$\int_{S_0} \left(W\delta_{1i} - \sigma_{ij}u_{j,1}\right) n_i dS = \int_{S} \left(\sigma_{ij}u_{j,1} - W\delta_{1i}\right) m_i q dS \tag{2.26}$$

where, $i, j = 1, 2$, $m_i = -n_i$ on S_0, and $m_1 = 0$, $m_2 = \pm 1$ on S_+ and S_-.

Finally, applying the divergence theorem and merging the resulting equation with the second integral of Eq. (2.24), the following expression is obtained:

$$\begin{aligned} J = {} & \int_{A} \left(\sigma_{ij}u_{j,1} - W\delta_{1i}\right) q_{,i} dA + \int_{A} \left(\sigma_{ij}u_{j,1} - W\delta_{1i}\right)_{,i} q dA + \\ & + \int_{A} \beta\varepsilon_{ii} \frac{\partial T}{\partial x_1} q dA + \int_{A_0} \beta\varepsilon_{ii} \frac{\partial T}{\partial x_1} dA \end{aligned} \tag{2.27}$$

where, A is the area enclosed by S. The last equation simplifies when the inner path S_0 shrinks to the tip, thus obtaining:

$$J=\int_A\left(\sigma_{ij}u_{j,1}-W\delta_{1i}\right)q_{,i}dA+\int_A\left(\sigma_{ij}u_{j,1}-W\delta_{1i}\right)_{,i}qdA+\int_A\beta\varepsilon_{ii}\frac{\partial T}{\partial x_1}qdA \quad (2.28)$$

By applying the *J*-integral to the superimposed state, it results:

$$J^{act+aux}=J^{act}+J^{aux}+M \quad (2.29)$$

where, J^{act} and J^{aux} represent the *J*-integral evaluated for the actual and the auxiliary states, respectively, while *M* is the *J*-integral of the mutual state (known as *M*-integral) that assumes the following expression:

$$\begin{aligned}M=&\int_A\left[\sigma_{ij}^{aux}u_{j,1}^{act}+\sigma_{ij}^{act}u_{j,1}^{aux}-\left(\frac{1}{2}\sigma_{jk}^{aux}\varepsilon_{jk}^{act}+\frac{1}{2}\sigma_{jk}^{act}\varepsilon_{jk}^{aux}\right)\delta_{1i}\right]q_{,i}dA+\\&+\int_A\left[\sigma_{ij}^{aux}u_{j,1}^{act}+\sigma_{ij}^{act}u_{j,1}^{aux}-\left(\frac{1}{2}\sigma_{jk}^{aux}\varepsilon_{jk}^{act}+\frac{1}{2}\sigma_{jk}^{act}\varepsilon_{jk}^{aux}\right)\delta_{1i}\right]_{,i}qdA+\text{ with } i,j,k=1,2\\&+\int_A\beta\varepsilon_{ii}^{aux}\frac{\partial T^{act}}{\partial x_1}qdA\end{aligned} \quad (2.30)$$

Focusing the attention on the third term of the first and second integral of Eq. (2.30):

$$\begin{aligned}&\frac{1}{2}\left(\sigma_{jk}^{act}\varepsilon_{jk}^{aux}+\sigma_{jk}^{aux}\varepsilon_{jk}^{act}\right)\delta_{1i}=\frac{1}{2}\left(C_{jklm}\varepsilon_{lm}^{act}\varepsilon_{jk}^{aux}+\sigma_{jk}^{aux}\varepsilon_{jk}^{act}\right)\delta_{1i}=\\&\frac{1}{2}\left(\sigma_{lm}^{aux}\varepsilon_{lm}^{act}+\sigma_{jk}^{aux}\varepsilon_{jk}^{act}\right)\delta_{1i}=\frac{1}{2}\left(\sigma_{jk}^{aux}\varepsilon_{jk}^{act}+\sigma_{jk}^{aux}\varepsilon_{jk}^{act}\right)\delta_{1i}=\sigma_{jk}^{aux}\varepsilon_{jk}^{act}\delta_{1i}\end{aligned} \quad (2.31)$$

Eq. (2.30) reduces as follows:

$$
\begin{aligned}
M = & \int_A \left[\sigma_{ij}^{aux} u_{j,1}^{act} + \sigma_{ij}^{act} u_{j,1}^{aux} - \sigma_{jk}^{aux} \varepsilon_{jk}^{act} \delta_{1i} \right] q_{,i} dA + \\
& + \int_A \left[\sigma_{ij}^{aux} u_{j,1}^{act} + \sigma_{ij}^{act} u_{j,1}^{aux} - \sigma_{jk}^{aux} \varepsilon_{jk}^{act} \delta_{1i} \right]_{,i} qdA + \int_A \beta \varepsilon_{ii}^{aux} \frac{\partial T^{act}}{\partial x_1} qdA
\end{aligned} \tag{2.32}
$$

Next, let us expand the derivative of the second integral:

$$
\begin{aligned}
M = & \int_A \left[\sigma_{ij}^{aux} u_{j,1}^{act} + \sigma_{ij}^{act} u_{j,1}^{aux} - \sigma_{jk}^{aux} \varepsilon_{jk}^{act} \delta_{1i} \right] q_{,i} dA + \\
& + \int_A \left[\sigma_{ij,i}^{aux} u_{j,1}^{act} + \sigma_{ij}^{aux} u_{j,1i}^{act} + \sigma_{ij,i}^{act} u_{j,1}^{aux} + \sigma_{ij}^{act} u_{j,1i}^{aux} - \sigma_{jk,1}^{aux} \varepsilon_{jk}^{act} - \sigma_{jk}^{aux} \varepsilon_{jk,1}^{act} \right] qdA \\
& + \int_A \beta \varepsilon_{ii}^{aux} \frac{\partial T^{act}}{\partial x_1} qdA
\end{aligned} \tag{2.33}
$$

The equilibrium conditions for the actual and auxiliary fields imply that $\sigma_{ij,i}^{act} = 0$ and $\sigma_{ij,i}^{aux} = 0$. Also, the compatibility conditions for the actual state involve that $\sigma_{ij}^{aux} u_{j,1i}^{act} - \sigma_{jk}^{aux} \varepsilon_{jk,1}^{act} = 0$. Hence, Eq. (2.33) becomes:

$$
\begin{aligned}
M = & \int_A \left[\sigma_{ij}^{aux} u_{j,1}^{act} + \sigma_{ij}^{act} u_{j,1}^{aux} - \sigma_{jk}^{aux} \varepsilon_{jk}^{act} \delta_{1i} \right] q_{,i} dA + \\
& + \int_A \left[\sigma_{ij}^{act} u_{j,1i}^{aux} - \sigma_{jk,1}^{aux} \varepsilon_{jk}^{act} \right] qdA + \int_A \beta \varepsilon_{ii}^{aux} \frac{\partial T^{act}}{\partial x_1} qdA
\end{aligned} \tag{2.34}
$$

Note that the first integral of Eq. (2.34) is always present; the third is activated in the presence of a temperature field, while the second is non-zero for heterogeneous materials only. For the latter, the current model adopts the incompatibility formulation proposed by Kim and Paulino (Kim and Paulino, 2004b). This formulation assumes the auxiliary displacement and stress fields associated with the Williams' crack tip asymptotic solutions. In this context, equilibrium and constitutive relationships are satisfied, but compatibility is violated:

$$\begin{cases} \varepsilon_{ij}^{aux} = S_{ijkl}(\mathbf{X})\,\sigma_{kl}^{aux} \\ \varepsilon_{ij}^{aux} \neq \dfrac{1}{2}\left(u_{i,j}^{aux} + u_{j,i}^{aux}\right) \end{cases} \quad \text{with } i,j=1,2 \tag{2.35}$$

In addition, by using the approach proposed by Yu et al. (Yu et al., 2009), one assumes an extra strain field (ε_{ij}^{aux0}) satisfying compatibility conditions and defined as follows:

$$\begin{aligned} \varepsilon_{ij}^{aux0} &= S_{ijkl}^{tip}\sigma_{kl}^{aux} \\ \varepsilon_{ij}^{aux0} &= \frac{1}{2}\left(u_{i,j}^{aux} + u_{j,i}^{aux}\right) \end{aligned} \tag{2.36}$$

where, S_{ijkl}^{tip} is the compliant tensor calculated at the crack tip. However, the strain field defined by Eq. (2.36) is different from the one described in Eq. (2.35). In other words, $\varepsilon_{ij}^{aux} \neq \varepsilon_{ij}^{aux0}$. This further condition is in accordance with the incompatibility formulation and will be helpful in the definition of an *M*-integral expression more suitable from a numerical implementation viewpoint.

In view of Eq. (2.36), the first term in the second integral of Eq. (2.34) can be expressed as follows:

$$\begin{aligned} \sigma_{ij}^{act}u_{j,i1}^{aux} &= \sigma_{ij}^{act}\,\frac{1}{2}\left(u_{j,i1}^{aux} + u_{i,j1}^{aux}\right) = \sigma_{ij}^{act}\,\varepsilon_{ij,1}^{aux0} = \\ &= \sigma_{ij}^{act}\left(S_{ijkl}^{tip}\sigma_{kl}^{aux}\right)_{,1} = \sigma_{ij}^{act}S_{ijkl}^{tip}\sigma_{kl,1}^{aux} \end{aligned} \tag{2.37}$$

Substituting Eq. (2.37) in Eq. (2.34), because of $\varepsilon_{ij} = S_{ijkl}\left(\mathbf{X}\right)\sigma_{kl}$, one obtains:

$$\begin{aligned} M &= \int_A \left[\sigma_{ij}^{aux}u_{j,1}^{act} + \sigma_{ij}^{act}u_{j,1}^{aux} - \sigma_{jk}^{aux}\varepsilon_{jk}^{act}\delta_{1i}\right]q_{,i}dA + \\ &+ \int_A \sigma_{ij}^{act}\left[S_{ijkl}^{tip} - S_{ijkl}\left(\mathbf{X}\right)\right]\sigma_{kl,1}^{aux}q\,dA + \int_A \beta\varepsilon_{ii}^{aux}\frac{\partial T^{act}}{\partial x_1}q\,dA \end{aligned} \tag{2.38}$$

Since the crack tip moves during propagation according to the ALE formulation, Eq. (2.38) should be evaluated with reference to the moving frame, like the fundamental equations of the fracture mechanics problem. Only the actual field must be projected into the moving frame because the auxiliary field is independent of the movement. Hence, Eq. (2.38) becomes:

$$\begin{aligned} M = & \int_{A_R} \left(\sigma_{ij}^{aux} u_{j,h}^{R} \left(X_h^R \right)_{,n}^{M} \left(X_n^M \right)_{,1}^{C} \right) q_{,h} \left(X_h^R \right)_{,n}^{M} \left(X_n^M \right)_{,i}^{C} \bar{J}_A dA_R + \\ & + \int_{A_R} \left(C_{ijkl} u_{k,h}^{R} \left(X_h^R \right)_{,n}^{M} \left(X_n^M \right)_{,l}^{C} u_{j,1}^{aux} \right) q_{,h} \left(X_h^R \right)_{,n}^{M} \left(X_n^M \right)_{,i}^{C} \bar{J}_A dA_R + \\ & - \int_{A_R} \left(C_{jkpq} u_{p,h}^{R} \left(X_h^R \right)_{,n}^{M} \left(X_n^M \right)_{,q}^{C} \varepsilon_{ij}^{aux} \delta_{1i} \right) q_{,h} \left(X_h^R \right)_{,n}^{M} \left(X_n^M \right)_{,i}^{C} \bar{J}_A dA_R + \\ & + \int_{A_R} C_{ijkl} u_{k,h}^{R} \left(X_h^R \right)_{,n}^{M} \left(X_n^M \right)_{,l}^{C} \left[S_{ijkl}^{tip} - S_{ijkl} \right] \cdot \varepsilon_{kl,1}^{aux} q \left[\Xi_i \left(\Psi_i \left(X_i^R \right) \right) \right] \bar{J}_A dA_R + \\ & + \int_{A_R} \beta \varepsilon_{ii}^{aux} T_{,h} \left(X_h^R \right)_{,n}^{M} \left(X_n^M \right)_{,1}^{C} q \left[\Xi_i \left(\Psi_i \left(X_i^R \right) \right) \right] \bar{J}_A dA_R \end{aligned} \tag{2.39}$$

In Eq. (2.39), A_R is the domain area in the referential system, $\bar{J}_A$ is the Jacobian related to the area, and Ξ is the mapping function that links the absolute moving frame with the crack tip local coordinate system. According to the relationships between the *J*-integral and SIFs for two-dimensional crack problems, the following expression is valid for the superimposed state:

$$M = \frac{\left(2K_I^{act} K_I^{aux} + 2K_{II}^{act} K_{II}^{aux} \right)}{E_{tip}^{'}} \tag{2.40}$$

where, $E_{tip}^{'} = E_{tip}$ for plane stress and $E_{tip}^{'} = E_{tip} / \left(1 - \nu_{tip}^2 \right)$ for plane strain.

The SIFs of the actual field are computed through two *M*-integral evaluated by combining the actual state with a pure mode I (aux-I) and a pure mode II (aux-II) auxiliary fields, namely $M^{act,aux-I}$ and $M^{act,aux-II}$, which provide the following simplified expression of the actual SIFs:

$$\begin{aligned} K_I^{act} &= \frac{E'_{tip} M^{act,aux-I}}{2K_I^{aux-I}} \quad \left(K_{II}^{aux-I} = 0\right) \\ K_{II}^{act} &= \frac{E'_{tip} M^{act,aux-II}}{2K_{II}^{aux-II}} \quad \left(K_I^{aux-II} = 0\right) \end{aligned} \tag{2.41}$$

2.3.1 Williams' asymptotic solutions

The Williams' asymptotic solutions, in terms of displacements, for pure mode-I and pure mode-II are the following:

$$\begin{cases} u_1^{aux} = \dfrac{K_I^{aux}}{8\mu_{tip}\pi}\sqrt{2\pi r}\left[\left(2\kappa_{tip}-1\right)\cos\left(\dfrac{\theta}{2}\right)-\cos\left(\dfrac{3\theta}{2}\right)\right] \\ u_2^{aux} = \dfrac{K_I^{aux}}{8\mu_{tip}\pi}\sqrt{2\pi r}\left[\left(2\kappa_{tip}+1\right)\sin\left(\dfrac{\theta}{2}\right)-\sin\left(\dfrac{3\theta}{2}\right)\right] \end{cases} \quad (\text{Mode I}) \tag{2.42}$$

$$\begin{cases} u_1^{aux} = \dfrac{K_{II}^{aux}}{8\mu_{tip}\pi}\sqrt{2\pi r}\left[\left(2\kappa_{tip}+3\right)\sin\left(\dfrac{\theta}{2}\right)+\sin\left(\dfrac{3\theta}{2}\right)\right] \\ u_2^{aux} = -\dfrac{K_{II}^{aux}}{8\mu_{tip}\pi}\sqrt{2\pi r}\left[\left(2\kappa_{tip}-3\right)\cos\left(\dfrac{\theta}{2}\right)+\cos\left(\dfrac{3\theta}{2}\right)\right] \end{cases} \quad (\text{Mode II}) \tag{2.43}$$

Instead, the stresses fields are defined as follows:

$$\begin{cases} \sigma_{11}^{aux} = \dfrac{K_I^{aux}}{\sqrt{2\pi r}}\cos\left(\dfrac{\theta}{2}\right)\left[1-\sin\left(\dfrac{\theta}{2}\right)\sin\left(\dfrac{3\theta}{2}\right)\right] \\ \sigma_{12}^{aux} = \dfrac{K_I^{aux}}{\sqrt{2\pi r}}\sin\left(\dfrac{\theta}{2}\right)\cos\left(\dfrac{\theta}{2}\right)\cos\left(\dfrac{3\theta}{2}\right) \\ \sigma_{22}^{aux} = \dfrac{K_I^{aux}}{\sqrt{2\pi r}}\cos\left(\dfrac{\theta}{2}\right)\left[1+\sin\left(\dfrac{\theta}{2}\right)\sin\left(\dfrac{3\theta}{2}\right)\right] \end{cases} \quad (\text{Mode I}) \tag{2.44}$$

$$\begin{cases} \sigma_{11}^{aux} = -\dfrac{K_{II}^{aux}}{\sqrt{2\pi r}} \sin\left(\dfrac{\theta}{2}\right)\left[2+\cos\left(\dfrac{\theta}{2}\right)\cos\left(\dfrac{3\theta}{2}\right)\right] \\ \sigma_{12}^{aux} = \dfrac{K_{II}^{aux}}{\sqrt{2\pi r}} \cos\left(\dfrac{\theta}{2}\right)\left[1-\sin\left(\dfrac{\theta}{2}\right)\sin\left(\dfrac{3\theta}{2}\right)\right] \\ \sigma_{22}^{aux} = \dfrac{K_{II}^{aux}}{\sqrt{2\pi r}} \sin\left(\dfrac{\theta}{2}\right)\cos\left(\dfrac{\theta}{2}\right)\cos\left(\dfrac{3\theta}{2}\right) \end{cases} \quad \text{(Mode II)} \qquad (2.45)$$

In Eqs. (2.42)-(2.45) (r,θ) are the polar coordinates in the crack tip coordinate system, μ_{tip} denotes the shear modulus, and κ_{tip} is the Kolosov' constant, which is equal to:

$$\kappa_{tip} = \begin{cases} \dfrac{3-\nu_{tip}}{1-\nu_{tip}} & \text{(plane stress)} \\ 3-4\nu_{tip} & \text{(plane strain)} \end{cases} \qquad (2.46)$$

2.4 Numerical implementation

2.4.1 Galerkin approximation

The weak form of the governing equations of the solid mechanics (Eq. (2.17)) and those associated with the heat transfer problem (Eq. (2.18)), the smoothing regularization managing the mesh motion (Eq. (2.23)), and the fracture conditions (Eq. (2.12)) are implemented in a FE code based on a Galerkin approximation. The geometry of the computational domain is discretized into many finite elements (N^e), thus representing the fields of the problem through the product between isoperimetric shape functions and nodal variables. In this way, displacement, temperature, and nodal mesh motion fields, as well as Lagrangian multipliers, are expressed as follows:

$$\begin{aligned} \mathbf{u} &= \sum_{i=1}^{N_e} \mathbf{N}_{\mathrm{i}}^{\mathrm{U}} \mathbf{U}_{\mathrm{i}}, \quad \mathbf{T} = \sum_{i=1}^{N_e} \mathbf{N}_i^{T} \mathbf{T}_i \\ \mathbf{X}^{M} &= \sum_{i=1}^{N_e} \mathbf{N}_i^{ALE} \mathbf{X}_i^{M}, \quad \boldsymbol{\lambda} = \sum_{i=1}^{N_e} \mathbf{N}_i^{\lambda} \boldsymbol{\Lambda}_i \end{aligned} \tag{2.47}$$

where, $\left(\mathbf{N}_{\mathrm{i}}^{\mathrm{U}}, \mathbf{N}_{\mathrm{i}}^{\mathrm{T}}, \mathbf{N}_{\mathrm{i}}^{\mathrm{ALE}}, \mathbf{N}_{\mathrm{i}}^{\lambda}\right)$ are the matrix collecting interpolation functions and $\left(\mathbf{U}_{\mathrm{i}}, \mathbf{T}_{\mathrm{i}}, \mathbf{X}_{\mathrm{i}}^{\mathrm{M}}, \boldsymbol{\Lambda}_{\mathrm{i}}\right)$ are the vector variables of the *i*-th element. Introducing Eq. (2.47) into Eqs. (2.17), (2.18), and (2.23), one obtained the following global system of equations:

$$\begin{aligned} &\mathbf{KU} = \mathbf{F} \\ &\mathbf{HT} = \mathbf{Q} \\ &\mathbf{AX}^{\mathbf{M}} + \mathbf{R}\boldsymbol{\Lambda} = \mathbf{0} \\ &\mathbf{RX}^{\mathbf{M}} - \mathbf{C} = \mathbf{0} \end{aligned} \tag{2.48}$$

where, $\mathbf{U}$ and $\mathbf{T}$ are the global displacements and nodal temperature variables; $\mathbf{K}, \mathbf{F}$ represent the global stiffness matrix and the load vector for the solid mechanics problem; $\mathbf{H}, \mathbf{Q}$ are the global conductivity matrix and the load vector for the heat transfer problem; $\mathbf{A}, \mathbf{R}$ are the ALE matrix and vector, respectively. Finally, $\mathbf{C}$ represents the vector collecting the positions of the crack tip evaluated by solving the constrained optimization problem given by Eq. (2.12).

2.4.2 Computational procedure

The proposed methodology has been implemented in COMSOL Multiphysics, a commercially available software that provides an efficient FE environment to handle complex models in a customized version. In addition, it offers linking apps to expand standard capabilities, like the LiveLink for MATLAB platform, which integrates COMSOL

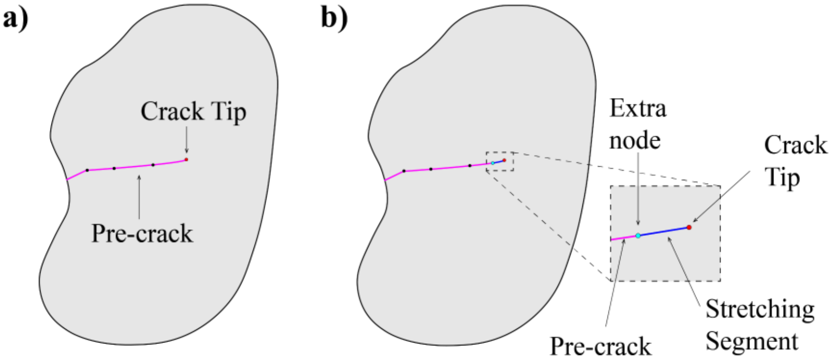

Figure 2.4. Description of the propagation procedure: (a) input geometry; (b) formation of the stretching segment.

with MATLAB functionalities. This app permits handling modeling and analysis steps through MATLAB script functions. The proposed model adopts this app to configure a user-made subroutine to automatically manage the crack propagation process.

The first step sets the geometry of the problem under investigation (Figure 2.4-a) and the material properties. At this stage, the initial pre-crack is a polyline that departs from the external boundary and develops up to an internal crack tip. In the present methodology, the ALE moves the crack tip once fracture onset conditions occur, thus simulating the crack propagation process. This movement must develop in such a way as to preserve the shape of the initial pre-crack with the crack tip to move. To ensure this condition, the procedure fragments the initial polyline representing the pre-crack by adding an extra node close to the crack tip, thus giving rise to a short segment (Figure 2.4-b), denoted as the stretching segment. The new segment will stretch during the propagation, leaving the remaining pre-crack unaltered. Therefore, the extra

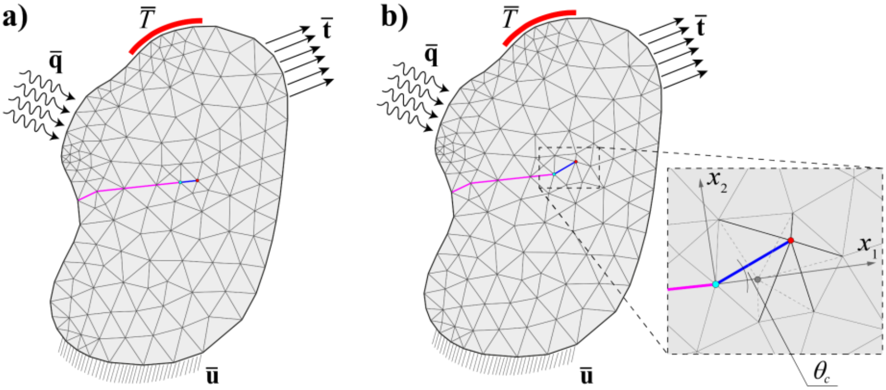

Figure 2.5. Description of the propagation procedure: (a) setting of the boundaries conditions and meshing the geometry domain; (b) propagation phase.

node serves as an anchor point for the stretching segment and represents a novel internal crack.

Once built the geometry, the procedure sets the boundary conditions and meshes the computational domain (Figure 2.5-a). Afterward, the analysis starts, and external loadings are progressively increased. For each increment, the code extracts mixed-mode SIFs (K_I, K_{II}) at the crack front through the *M*-integral (Eqs. (2.39)-(2.41)). The extracted SIFs are used to evaluate the kinking angle $\overline{\theta}$ through the kinking function k_F. Next, K_I, K_{II}, and $\overline{\theta}$ are used to check crack onset conditions through the fracture function f_F assuming $f_F\left(K_I, K_{II}, \overline{\theta}\right)=0$. Note that, both k_F and f_F can be defined using classic fracture criteria developed in the context of Fracture Mechanics. In particular, the proposed method adopts the Maximum Hoop Stress Criterion proposed by Erdogan and Sih (Erdogan and Sih, 1963), which provides the following expressions for the kinking angle:

$$\theta_c = k_F\left(K_I, K_{II}\right) = \begin{cases} 2\tan^{-1}\left(\dfrac{K_I}{4K_{II}} - \dfrac{1}{4}\sqrt{\left(\dfrac{K_I}{K_{II}}\right)^2 + 8}\right) & for\, K_{II} > 0 \\ 2\tan^{-1}\left(\dfrac{K_I}{4K_{II}} + \dfrac{1}{4}\sqrt{\left(\dfrac{K_I}{K_{II}}\right)^2 + 8}\right) & for\, K_{II} < 0 \end{cases} \quad (2.49)$$

In addition, such a criterion can be used to define the following fracture function:

$$f_F = f_F\left(K_I, K_{II}, \theta_c, K_{IC}\right) = \frac{K_I \cos^3\left(\dfrac{\theta_c}{2}\right) - 3K_{II}\cos^2\left(\dfrac{\theta_c}{2}\right)\sin\left(\dfrac{\theta_c}{2}\right)}{K_{IC}} - 1 \quad (2.50)$$

Although the proposed model is defined in the present work using the Maximum Hoop Stress Criterion proposed by Erdogan and Sin (Erdogan and Sih, 1963), it is quite flexible to be defined using different fracture criteria, such as the Maximum Energy Release Rate Criterion defined by Hussain et al. (Hussain et al., 1974).

When crack onset conditions are satisfied ($f_F = 0$), then $\bar{\theta} = \theta_c$ and the propagation process starts (Figure 2.5-b). The mesh node of the crack tip moves according to the ALE condition defined by Eq. (2.20) and fracture conditions of Eq. (2.12).

The movement of the crack tip implies the extension of the stretching segment along θ_c. As the segment stretches, the elements around the crack tip distort because of the nodal movements. Larger distortions need re-meshing processes to restore regularity in the mesh frame and avoid losing accuracy. The mesh distortion is checked through the first

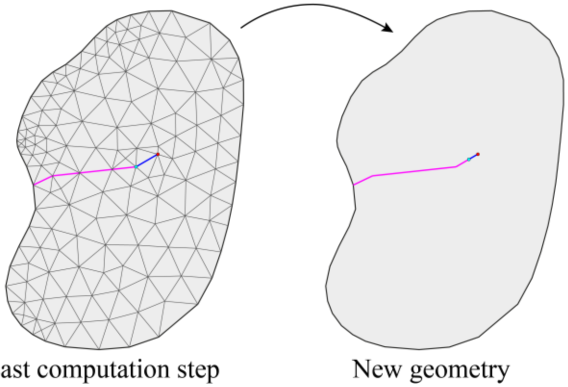

Figure 2.6. Description of the propagation procedure: formation of a novel geometry based on the last computation step (if $\theta_c >$ Toll. (θ_c)).

invariant of the isochoric Green-Lagrange strain ($\mathbf{E}^{MC}$) evaluated concerning the computational mesh and defined as:

$$\Upsilon = I_1\left(\mathbf{E}^{\mathrm{MC}}\right) = tr\frac{1}{2}\left(\frac{\mathbf{F}^{\mathrm{T}}\mathbf{F}}{\det(\mathbf{F})} - \mathbf{I}\right) \quad \text{with} \quad \mathbf{F} = \frac{\partial \boldsymbol{\Phi}^{-1}(\chi)}{\partial \chi} \tag{2.51}$$

Remeshing occurs only when Υ_{Max} (the maximum value of Υ inside the mesh configuration) is larger than a specified threshold Toll.(Υ).

The possibility of managing remeshing by checking mesh configuration distortion at each crack tip displacement increment saves relevant computational resources. Standard FEM procedures perform remeshing actions at any incremental step, thus spending considerable computational time to trace the entire trajectory of arbitrarily growing cracks. Besides, in the proposed strategy, the computational mesh is modified with great regularity due to rezoning methods. Then, it reduces the possibility of localized, highly distorted elements.

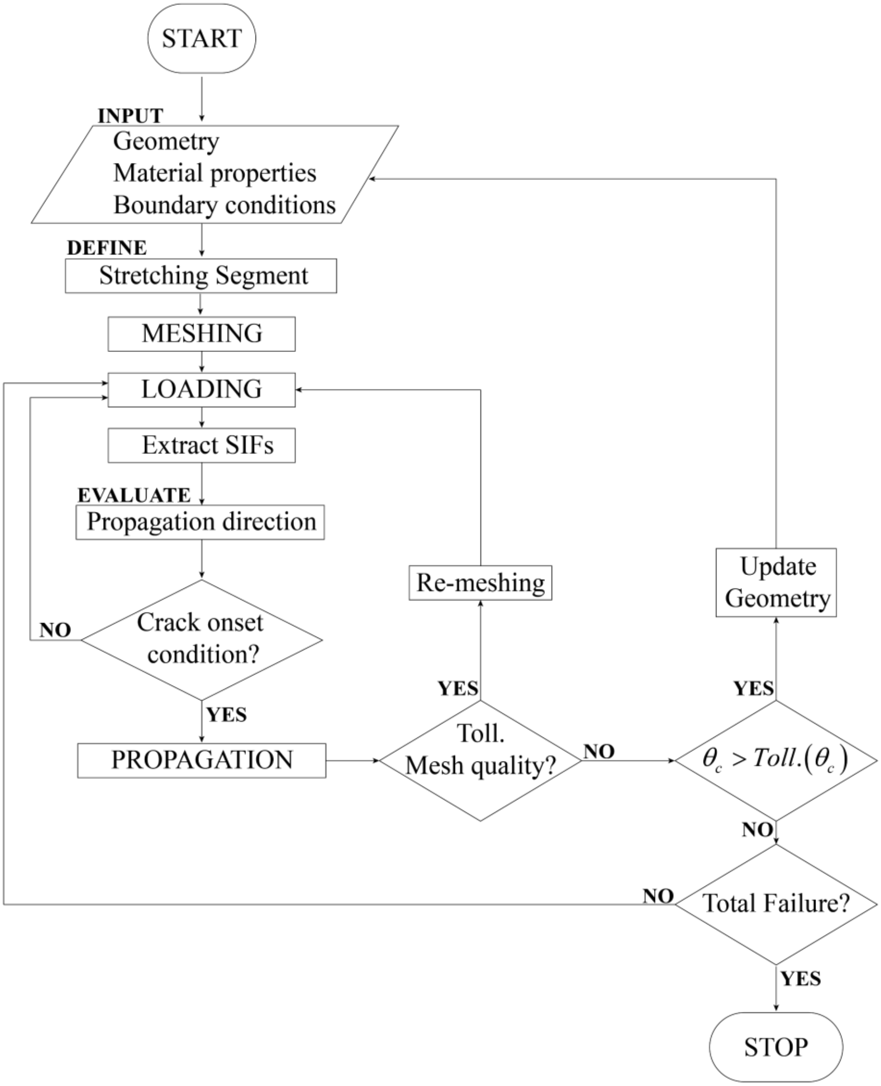

Figure 2.7. Flowchart of the propagation process.

The stretching segment deforms until the variation angle concerning the initial pre-crack direction is lower than a pre-selected tolerance value $Toll(\theta_c)$ (Figure 2.5-b). In numerical simulations, such a threshold was set equal to 2° so that the proposed model can correctly describe any type of crack trajectory. When this condition is satisfied, the propagation process arrests. If the structure has not reached the maximum capacity, the procedure updates the model's geometry using the configuration obtained during the last analysis step (Figure 2.6). The new geometry is adopted as novel input for the code, using boundary conditions of the last converged analysis step. This implies that a new stretching segment is created on the novel geometry.

The procedure transfers analysis data from the previous distorted elements to the new computational points. Then, it re-starts the analysis. The propagation continues until the non-convergence conditions due to collapse mechanics are reached. Figure 2.7 shows a flowchart summarizing the steps and concepts of the developed subroutine.

3

Static fracture analysis: Numerical results

This chapter proposes two sets of numerical results aimed at checking the reliability and efficacy of the present method in reproducing crack propagation processes under quasi-static conditions.

The first set of results deals with the failure analysis of homogeneous linear elastic material structures subjected to thermal and mechanical loadings. In particular, the following three practical examples are considered:

- A simply supported beam subjected to a four-point bending test.
- A cruciform plate under mechanical and thermal loadings.

- A rectangular plate with two holes affected by multiple cracks subjected to complex thermo-mechanical loadings.

The second set of results concerns the failure simulation of the Functionally Graded Materials (FGMs) structures. In particular, the following two-dimensional structures under mixed-mode crack propagation mechanisms are investigated:

- A notched glass-epoxy beam under a four-point bending test.
- A glass-epoxy plate with two cracks emanating from two holes.
- A glass-epoxy plate with branched cracks subjected to uniform tension.

For each case, the results obtained through the proposed methodology are compared with data reported in the literature. Such references include predictions gained both experimentally and by existing numerical strategies. In addition, the study involves specific analyses to assess (i) the accuracy of SIFs extraction during the crack propagation, (ii) mesh sensitivity, and (iii) the influence of the shape of the q function used by the M-integral method. Such aspects are analyzed by focusing attention on the number of remeshing events involved and the computational time spent to perform numerical simulations.

Propagation processes involve an incremental static step-by-step procedure according to a displacement-based approach. In other words, this implies identifying the increment of external loads that produces a prescribed displacement variation of a selected control point. For each

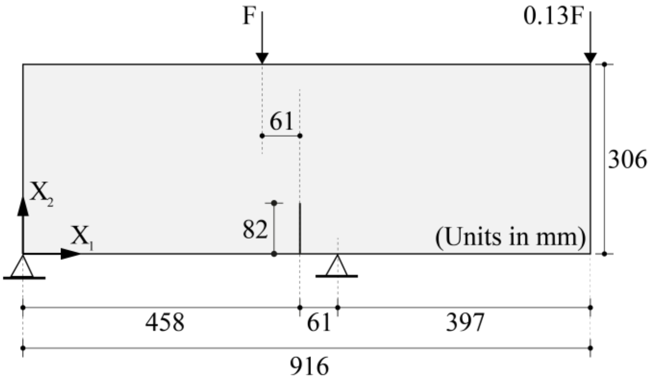

Figure 3.1. A simply supported beam subjected to a four-point bending test: a schematic of geometry and boundaries conditions.

load increment, the method (through the *M*-integral approach) extracts Stress Intensity Factors (SIFs) at the crack front, which are essential to check crack onset conditions and identify the crack propagation direction. All investigated examples were reproduced numerically using the same discretization approach, consisting of plane stress or strain 9-node triangular finite elements for the computational mesh. All the numerical analyses were performed with a standard PC equipped with an Intel Core i7-9750H running at 2.60 GHz with 16 GB RAM.

3.1 A simply supported beam subjected to a four-point bending test.

Figure 3.1 shows the geometry and the boundary conditions of a simply supported beam under a four-point bending test. The beam has a length of 916 mm, a height of 306 mm, and a thickness of 152 mm. Further, it has a vertical pre-crack of 82 mm starting from the mid-span. The Young’s modulus, Poisson’s ratio, and fracture toughness are equal

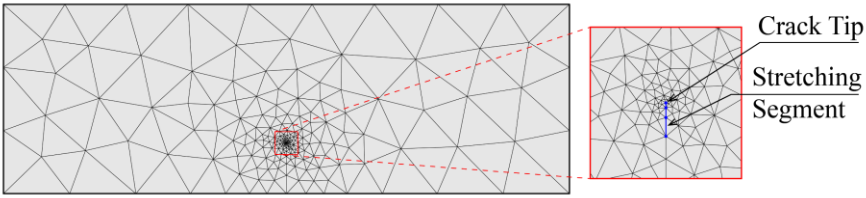

Figure 3.2. A simply supported beam subjected to a four-point bending test: initial mesh configuration adopted in numerical simulations (Mesh M1).

to $E=24.8$ GPa, $\nu=0.18$, and $K_{IC}=1.65$ MPa(m)$^{1/2}$, respectively. Plane stress conditions are assumed. Boundary conditions comprehend two hinges on the lower side ($X_2=0$) at $X_1=0$ and $X_1=519$ mm.

Figure 3.2 reports the mesh configuration employed in the numerical simulation. It comprises 217 nodes and 403 triangular elements, arranged fine near the crack tip and coarse elsewhere. As depicted in the zoomed view, the stretching segment (identified with the blue line) was discretized through three elements of variable length.

Several works have analyzed the fracture behavior of the beam through advanced numerical strategies, providing load-displacement curves and crack paths. Among these, Liao et al. (Liao et al., 2018) have replicated crack propagation by mixing the weak form Quadrature Element Method (QEM) with the Subregion Generalized Variational Principle (SGVP). Dai et al. (Dai et al., 2015) have adopted an automatic remeshing algorithm in the framework of the Scaled Boundary Finite Element Method (SBFEM). Finally, Yang et al. (Yang et al., 2015) have used a non-matching SBFEM-FEM coupled method.

Figure 3.3 compares the results obtained through the present methodology with numerical evaluations achieved by Liao et al. (Liao et al.,

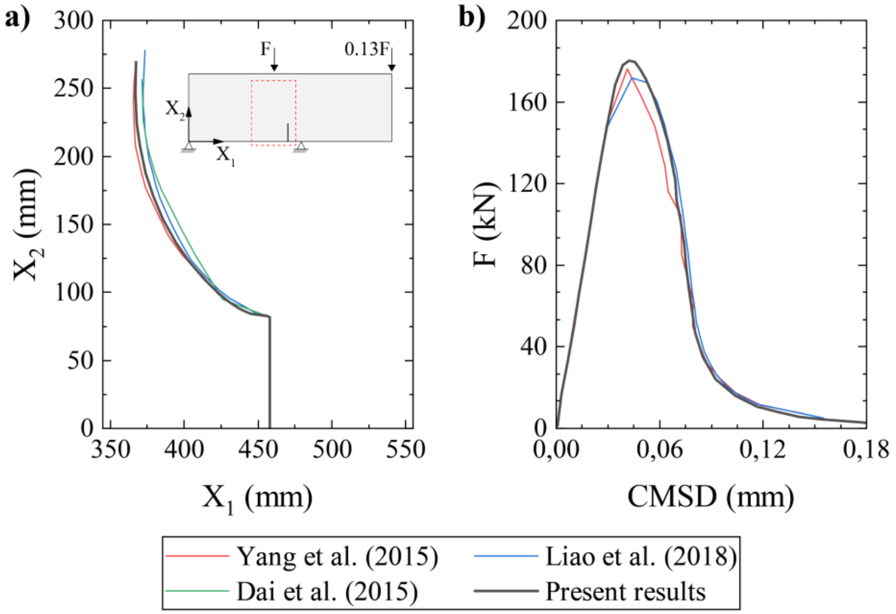

Figure 3.3. A simply supported beam subjected to a four-point bending test: comparisons in terms of (a) crack paths and (b) F-CMSD curves between the present method and numerical data reported in the literature.

2018), Dai et al. (Dai et al., 2015), and Yang et al.(Yang et al., 2015). Figure 3.3-a reports the crack path, while Figure 3.3-b shows the load (F) versus crack mouth sliding displacement (CMSD). One can observe that the proposed method is in good agreement with predictions gained by other numerical approaches, thus denoting a proper level of accuracy.

3.1.1 Parametric study in terms of mesh configurations

A parametric study is carried out to assess the computational efficiency and the accuracy of the proposed approach in terms of mesh configurations. The study compared the mesh configurations reported in

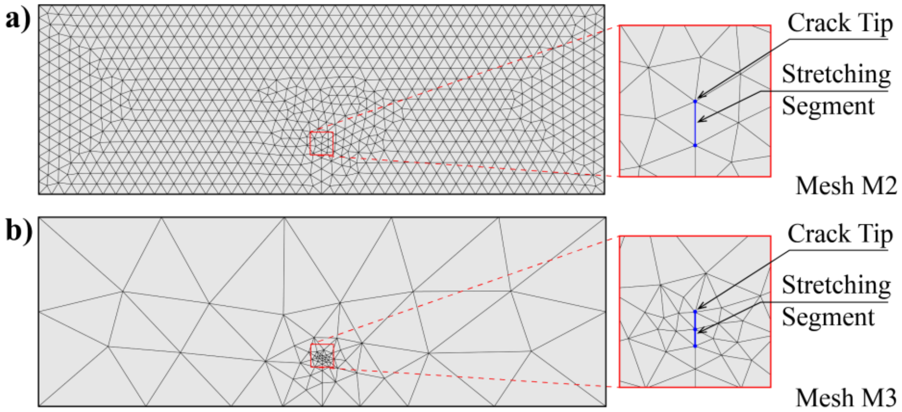

Figure 3.4. A simply supported beam subjected to a four-point bending test: schematic representation of (a) Mesh M2 and (b) Mesh M3.

Figure 3.2, Figure 3.4-a, and Figure 3.4-b, identified in the sequel as Mesh M1, Mesh M2, and Mesh M3, respectively. The Mesh M2 is a relatively uniform mesh having 1700 triangular elements and 910 nodes. The stretching segment comprises a single element only. The Mesh M3 presents an extra coarse configuration of 70 nodes and 121

Table 3.1 – A simply supported beam subjected to a four-point bending test: details of the meshes used in the parametric analysis.

	Triangular Elements				Stretching segment		
Type	DOFs	Number	Maximum size (mm)	Minimum size (mm)	Number of elements	Maximum size (mm)	Minimum size (mm)
M1	217	403	122.30	0.87	3	4.930	1.31
M2	910	1700	23.79	11.62	1	11.62	11.62
M3	70	121	198.50	4.44	2	4.10	4.10

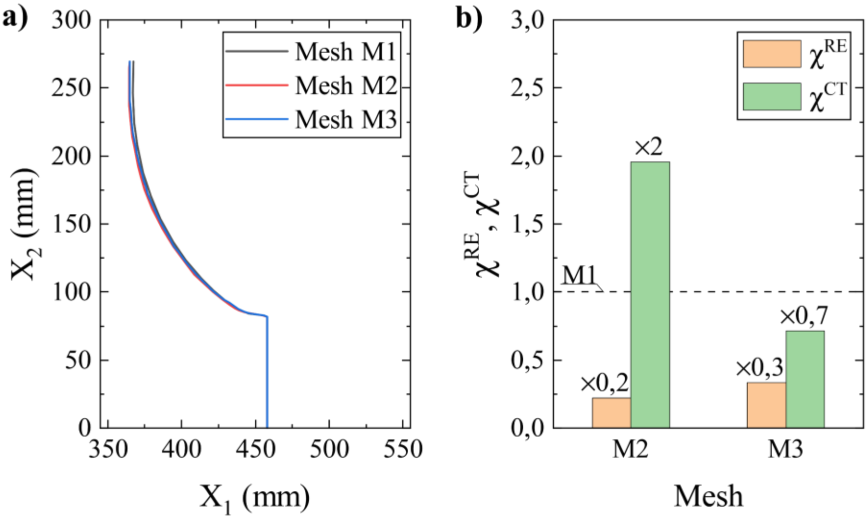

Figure 3.5. A simply supported beam subjected to a four-point bending test: comparisons between Mesh M1, Mesh M2, and Mesh M3 in terms of (a) crack path and (b) multiplicative factors of the number of remeshing events (χ^{RE}) and computational time (χ^{CT}).

triangular elements arranged fine only in the region close to the crack tip, where two elements compose the stretching segment. Table 3.1 reports detailed information about the examined meshes. The accuracy of the proposed method appears to be unaffected by the configuration of the computational mesh since the crack trajectories (see, Figure 3.5-a) are somewhat the same with improved mesh discretization.

Furthermore, the mesh configurations involve different computational times and remeshing processes to perform the simulation. To compare the data in a dimensionless context, the results of the Mesh M1 are assumed as a reference and the following factors are introduced:

$$\chi^{RE} = \frac{RE_i}{RE_R}, \quad \chi^{CT} = \frac{CT_i}{CT_R} \tag{3.1}$$

where, (RE_i, CT_i) and (RE_R, CT_R) represent the number of remeshing events and the computational time involved by the i-th investigated mesh and the referential one, respectively.

Figure 3.5-b reports the results in terms of bar columns.

As one can see, the Mesh M2 spent twice the time of the Mesh M1 to perform the entire simulation, while the Mesh M3 time is lower by 1/3 than Mesh M1. These results could be related to the total number of degrees of freedom (DOFs) of each mesh configuration. Indeed, as written previously, the Mesh M2 has 910 DOFs, while the Mesh M1 and the Mesh M3 involve 217 and 70 DOFs, respectively. Typically, the computational time increases with the number of DOFs in standard FE frameworks regardless of the simulation type. Instead, the highest number of remeshing events occurred using Mesh M1, while Mesh M2 and Mesh M3 require 1/5 and 1/3 of the remeshing events of Mesh M1, respectively. This happens because of the coarser mesh adopted to discretize the stretching segment. Refined stretching segments lead to many triangular elements near the crack tip. During the propagation, such elements are likely to meet elevated distortion conditions, thus involving a frequent recourse to remeshing actions.

In addition, the parametric study focused on mesh evolution during propagation. Figure 3.6 depicts the total number of elements involved in the meshes during the simulations and the ratio between the total number of triangular elements at the analysis's beginning and end. The results show that the consistency of refinement varies differently for the three meshes during the propagation. As expected, Mesh M3 has the

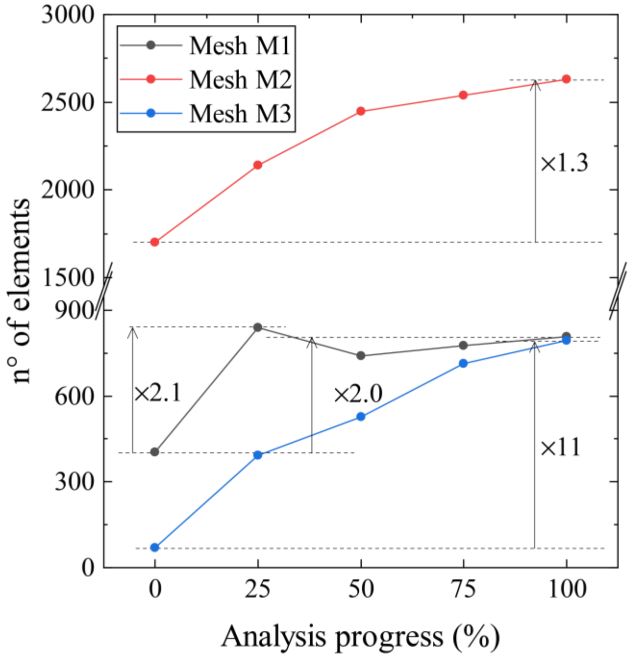

Figure 3.6. A simply supported beam subjected to a four-point bending test: variation of the total number of finite elements for the Mesh M1, Mesh M2, and Mesh M3 during the analysis.

larger refinement since the number of elements at the end of the simulation is 11 times bigger than that of the initial configuration. On the other hand, for Mesh M2 and Mesh M3, the increase is about 2 and 1.3 times bigger, respectively. All the aspects mentioned earlier highlight the present method's flexibility to adapt the mesh configuration during the analysis. In particular, the motion of the refined mesh region around the crack tip guarantees considerable computational saving.

Two relevant aspects can be identified concerning the advantages offered by the proposed approach compared to standard FEM procedures. The first deals with the computational mesh to use in the numerical model. Standard FEM procedures require refined mesh discretization for the entire geometry of the model to handle randomly growing cracks. Contrarily, the ALE approach requires a mesh refinement only around the crack tip region, thus leading coarse meshes elsewhere. The second regards the remeshing actions. Standard FEM involves continuous remeshing processes to adapt the mesh configuration at the crack trajectory, thus affecting computational efficiency. In the proposed methodology, remeshing actions occur only when mesh elements suffer from relevant distortions, thus reducing the possibility of computational issues when transferring the solution of the problem from the old to the novel mesh configuration.

3.2 A cruciform plate under mechanical and thermal loadings

The second example aims to assess the ability of the present method to predict crack propagation under mechanical and thermal loadings. Figure 3.7 depicts the geometry, boundary conditions, and initial mesh configuration. An initial notch is located at the bottom-right corner of the plate, inclined of β with respect to the horizontal axis. The plate has the following dimensions: side length L=1000 mm, pre-crack a_0=0.2L, and β=135°. Plane strain conditions are assumed. The Young's Modulus (E), the Poisson's ratio (ν), and the coefficient of thermal expansion (α_T) are equal to E=218400 Pa, ν=0.3, and α_T=1.67x10-5 1/°C, respectively. At the bottom, the left, and the right boundaries, the plate presents line constraints in which sliding translations are free only.

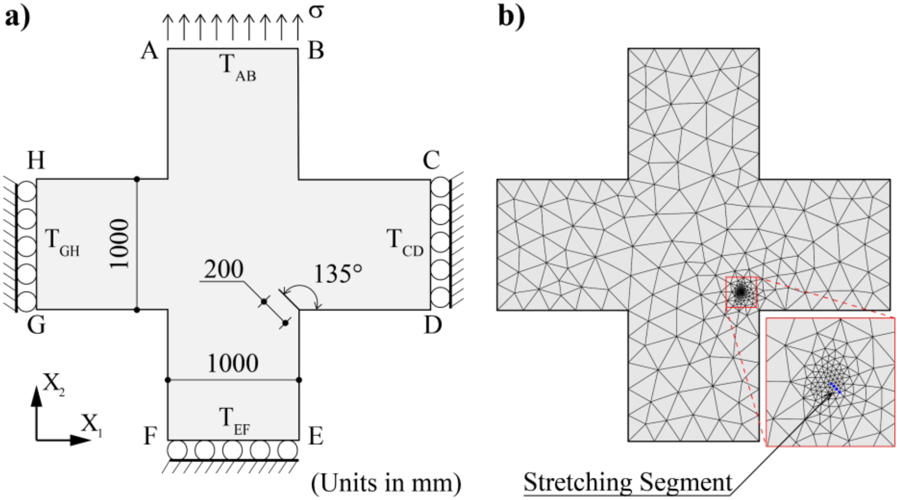

Figure 3.7. A cruciform plate under mechanical and thermal loadings: (a) geometry and boundaries conditions; (b) initial mesh configuration used in the simulation.

The study examined the plate under three different boundary conditions as listed in Table 3.2 and named in the sequel as case 1, case 2, and case 3. Case 1 involves a uniform tension σ=10 Pa, acting at the upper boundary (AB); case 2 comprises a thermal loading only induced

Table 3.2 – A cruciform plate under mechanical and thermal loadings: boundary conditions.

Boundary conditions	Temperature (°C)				Traction (Pa)
	Top (AB)	Bottom (FE)	Right (CD)	Left (GH)	Top (AB)
case 1	0	0	0	0	10
case 2	10	-10	0	0	0
case 3	10	-10	5	5	10

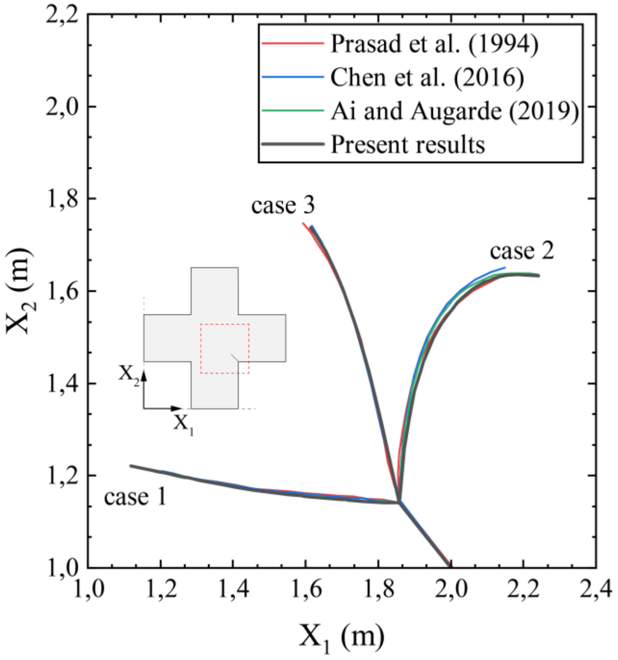

Figure 3.8. A cruciform plate under mechanical and thermal loadings: a comparison in terms of crack paths between the present method and numerical results provided by Prasad et al. (Prasad et al., 1994), Chen et al. (Chen et al., 2016), and Ai and Augarde (Ai and Augarde, 2019).

by a uniform temperature gradient T_{AB}=+10°C and T_{EF}=-10°C acting on the top (AB) and bottom (EF) boundaries; case 3 involves the simultaneous presence of uniform tractions equal to σ=10 Pa at the top (AB), and temperature gradients of T_{AB}=+10°C and T_{EF}=-10°C at the upper (AB) and bottom (EF) boundaries, together with T_{CD}=T_{GH}=-5°C at the right (CD) and left (GH) sides.

The initial mesh configuration (Figure 3.7-b) employed in numerical simulations involves 510 triangular elements fine arranged near the crack tip and the stretching segment has three elements (see zoomed

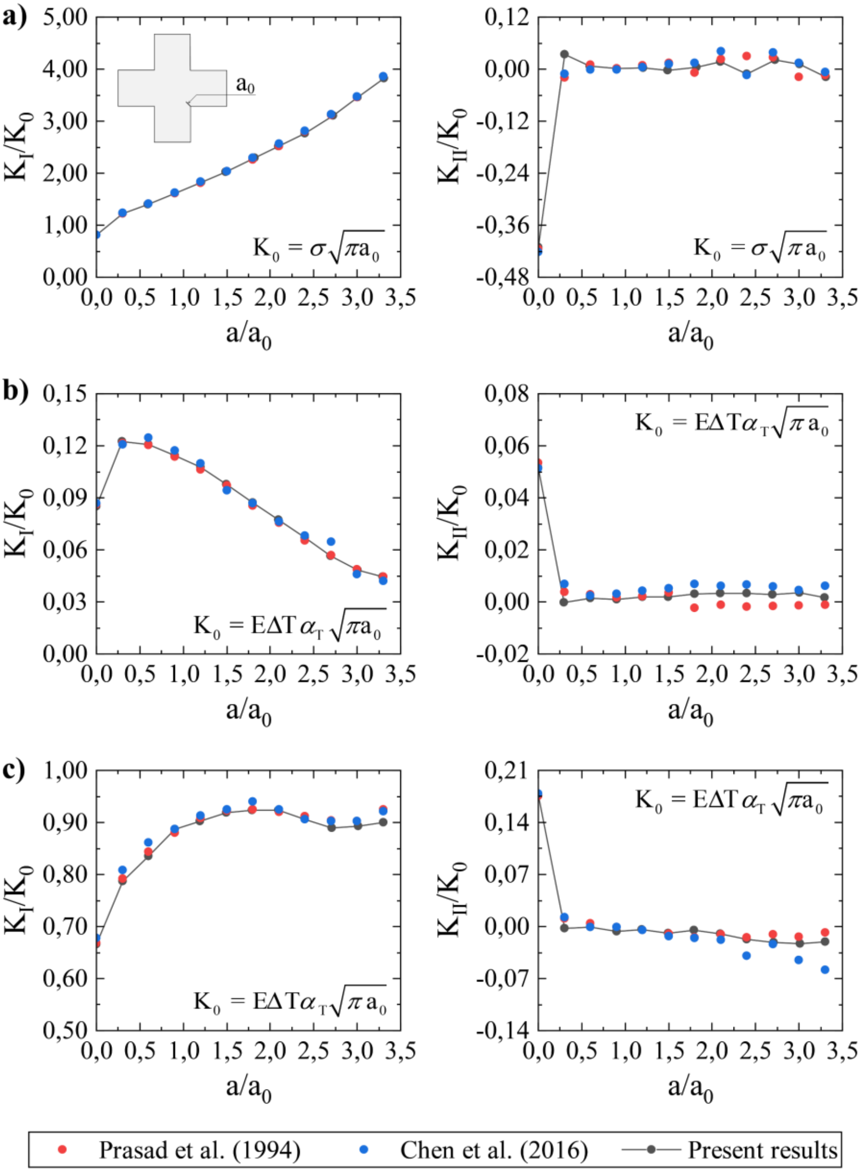

Figure 3.9. A cruciform plate under mechanical and thermal loadings: comparisons in terms of SIFs evaluation versus crack advance between the proposed approach and numerical results provided by Prasad et al. (Prasad et al., 1994), and Chen et al. (Chen et al., 2016).

view). Furthermore, the top and bottom boundaries present five elements to accurately represent the temperature field.

Recent works have predicted the fracture behavior of the plate through advanced numerical strategies, providing SIFs evaluations and crack trajectories. Among these, Prasad et al. (Prasad et al., 1994) have obtained crack paths and SIFs evaluations through the Boundary Element Method (BEM). Ai and Augarde (Ai and Augarde, 2019) have replicated the crack propagation using a meshless approach, and Chen et al. (Chen et al., 2016) have adopted the Singular Edge-Based Smoothed Finite Element Method (ES-FEM). Figure 3.8 compares the crack paths obtained through the proposed method with those gained by Prasad et al. (Prasad et al., 1994), Chen et al. (Chen et al., 2016), and Ai and Augarde. (Ai and Augarde, 2019). The results show that the proposed approach is in good agreement with existing methodologies for each boundary condition examined. In addition, such predictions denote the relevant role of thermal actions since the crack trajectories develop differently.

Finally, Figure 3.9 a-b-c report the values of SIFs during crack advance for cases 1, 2, and 3, respectively. As one can see, the SIFs evaluated by the present model match quite well those obtained by other authors. These results confirm the accuracy of the ALE formulation of the *M*-integral to extract fracture parameters at a movable crack front.

3.3 A rectangular plate with two holes affected by multiple cracks subjected to complex thermo-mechanical loadings

Figure 3.10 shows a rectangular plate of width L=20 mm and height H=10 mm with two holes of radius R=2 mm and two horizontal

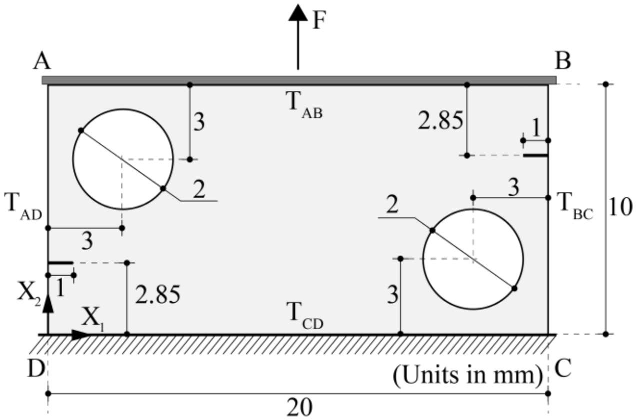

Figure 3.10. A plate under tension with two holes and two cracks: a schematic of geometry and boundary conditions.

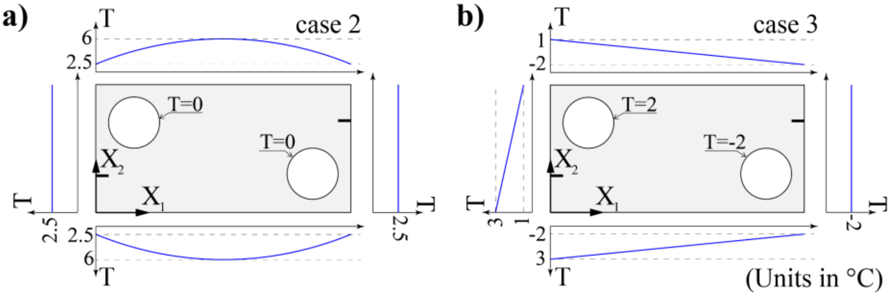

Figure 3.11. A plate under tension with two holes and two cracks: temperature profiles for (a) case 2 and (b) case 3.

pre-crack of length a_0=1 mm. The notches are one on the left and the other on the right boundary. In particular, they are distant 2.85 mm from the upper and lower edge, respectively. The holes are near the top-left and bottom-right corners. The distance between the center of the holes and the vertical and horizontal boundaries of the plate is equal to 3 mm.

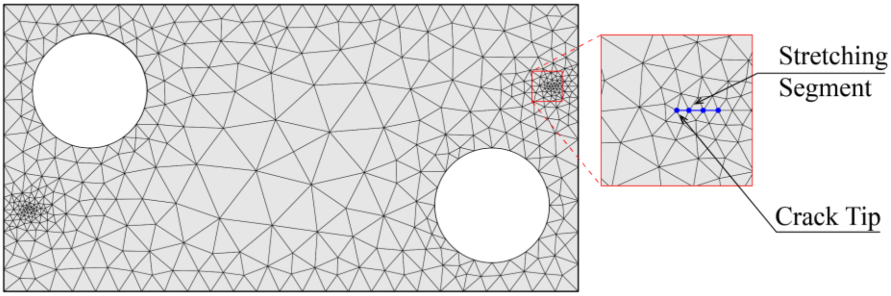

Figure 3.12. A plate under tension with two holes and two cracks: mesh configuration adopted in the numerical model.

Boundary conditions include a fixed constraint at the bottom and a rigid inner constraint at the top boundary. The Young's modulus, the Poisson's ratio, and the coefficient of thermal expansion are equal to E=0.2 MPa, ν=0.3, and α_T=1.00x10-5 1/°C. Plane stress conditions are assumed for the finite elements of the computational mesh.

This case aims to assess the ability of the proposed approach to handle multiple cracks growing within an articulated geometry under complex thermo-mechanical loadings. In particular, three loading configurations are considered: the first (case 1) comprises a traction force (F) on the top boundary; the second (case 2) and the third (case 3) combine a traction force (F) and temperature distributions on the external boundaries as reported in Figure 3.11. Case 1 has been investigated by many authors through several numerical models. Among these, Ooi et al. (Ooi et al., 2012) have adopted the Scaled Boundary Finite Element Method (SBFEM) to predict multiple crack propagation, while Ai et al. (Ai et al., 2019) have used a hybrid strategy based on the Cracking particles Method (CPM) and the Configurational Forces (CF) approach.

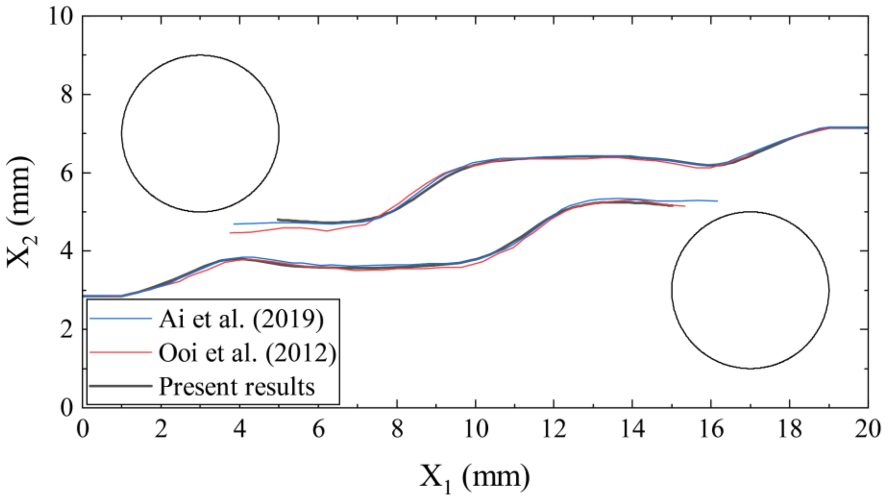

Figure 3.13. A plate under tension with two holes and two cracks: crack path for case 1. Comparisons between the present method and numerical results provide by Ooi et al. (Ooi et al., 2012) and Ai et al. (Ai et al., 2019).

On the other hand, cases 2 and 3 are investigated for the first time in the present work.

Firstly, the results regarding case 1 are discussed. In particular, this case serves as a reference to highlight the effect of the temperature on the crack paths and the bearing capacity of the plate.

By observing the geometry and boundary conditions of the problem, the crack path is expected to be symmetrical. A symmetrical path can be achieved in a FE framework by using symmetric mesh or adopting highly fine discretization. For this reason, the mesh employed to discretize the plate is refined (Figure 3.12). It involves 803 triangular elements whose characteristic size (h) varies between 0.12 mm and 2.16 mm. The finite elements are arranged finely around tip regions, and each stretching segment is discretized using 3-line elements. Instead,

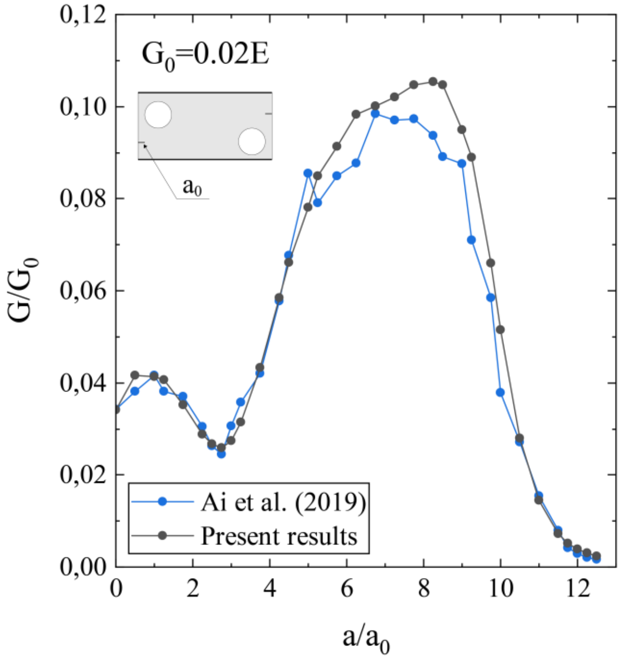

Figure 3.14. A plate under tension with two holes and two cracks: variation of the energy release rate during crack propagation for case 1. Comparison between the present method and numerical results provided by Ai et al. (Ai et al., 2019).

the holes have 20 elements, and the upper and bottom boundaries are subdivided into 25 elements of the same length. Figure 3.13 compares the crack trajectories predicted by the proposed method with those gained by Ooi et al. (Ooi et al., 2012) and Ai et al. (Ai et al., 2019). The results are in line with the predictions achieved by the other Authors. Furthermore, as expected, the crack paths are symmetric with the same extension.

Figure 3.14 reports Energy Release Rate (G) calculated through the proposed approach and the one developed by Ai et al. (Ai et al., 2019).

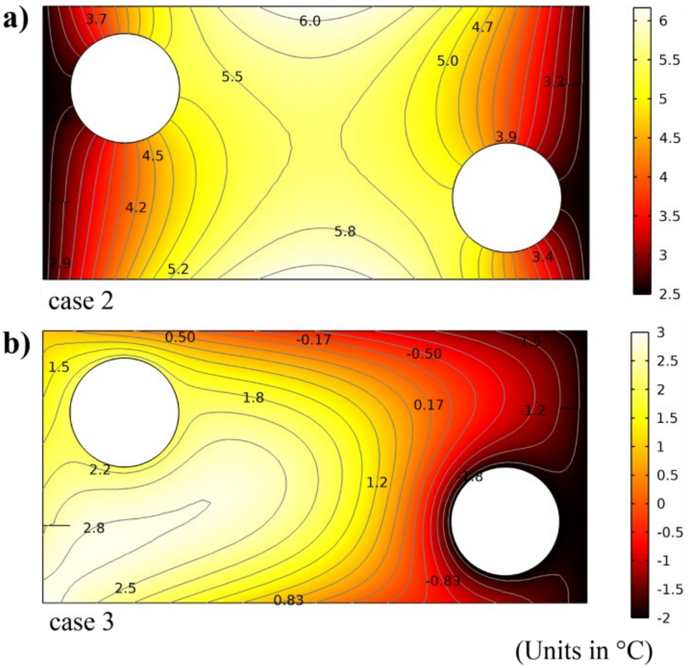

Figure 3.15. A plate under tension with two holes and two cracks: temperature distribution for (a) case 2 and (b) case 3.

The crack curves are almost the same, with the exception of the central part of the plot (i.e., for $5<a/a_0<8.5$), where the proposed method predicts values a little higher than that reported by Ai et al. (Ai et al., 2019). This increment occurs when the two cracks reach the center of the plate and interact reciprocally. Probably, during these steps, the interaction produces complex stress distributions in the region between the cracks, thus affecting the evaluation of the Energy Release Rate (G). However, it is worth noting that the maximum difference is about 15% and does not affect the accuracy of the results.

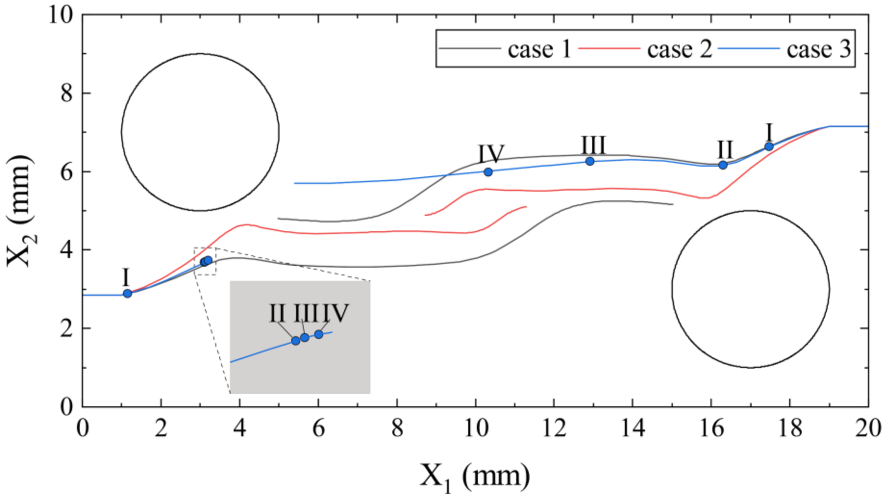

Figure 3.16. A plate under tension with two holes and two cracks: comparisons in terms of crack paths between case 1, case 2, and case 3.

In the last part of this section, results for cases 2 and 3 are examined. The mesh configuration is the same as that utilized for case 1.

Figure 3.15-a and b illustrate the temperature distributions for case 2 and case 3, respectively. In particular, case 3 presents a non-uniform temperature distribution, thus representing a significant test to check the efficiency of the proposed method because external action effects on the plate are not symmetric.

Figure 3.16 compares the crack paths for the three cases. like case 1, the crack paths of case 2 are symmetric, but the thermal gradient alters the crack trajectories. At the beginning of the numerical analysis, the holes attract the cracks; next, they kink horizontally and proceed simultaneously toward the middle of the plate. At this point, mutual interactions arise, involving new kinking in crack trajectories, that likely

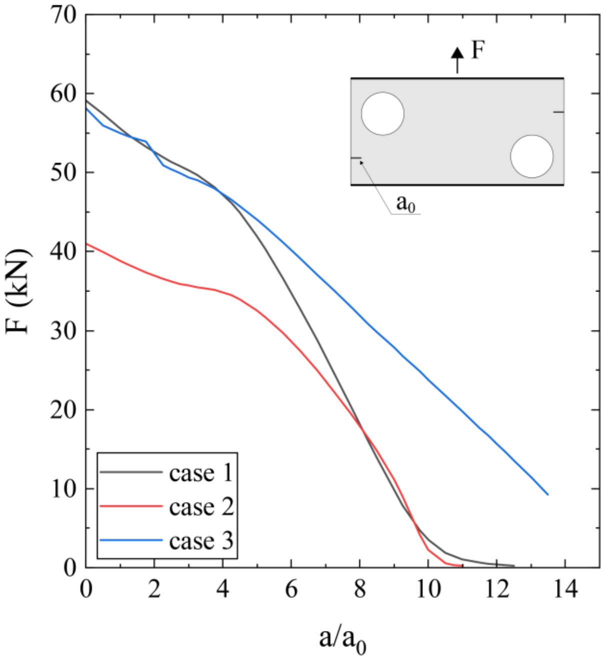

Figure 3.17. A plate under tension with two holes and two cracks: comparisons in terms of load vs crack advance between case 1, case 2, and case 3.

lead to the coalescence of the crack paths. This condition determines the collapse of the plate. Instead, in case 3, the crack fronts grow differently. At the beginning of the propagation process, the top-right front suffers from a rapid propagation downwards, while the bottom-left presents an imperceptible advance (point I). Next, both cracks grow almost simultaneously up to points marked by the Roman number II in the figure. From this point, the upper front kinks and continues to grow almost horizontally, whereas the bottom one manifests short crack advances (points III and IV).

It is important to emphasize that the proposed method can reproduce complex mechanisms starting from a mesh configuration refined only around the crack tip. During the propagation, the ALE modifies the mesh, thus providing fast time computation and accurate results.

Finally, Figure 3.17 compares cases 1, 2, and 3 in terms of load versus displacement curves. For case 2 the thermal gradient reduces the bearing capacity to about 44% regarding case 1, while in case 3, the plate reaches the same peak load as case 1, but the thermal gradient determines a more gradual softening behavior. These results highlight the considerable negative influence of the thermal gradient on the fracture behavior of the plate.

3.4 A notched glass-epoxy beam under a four-point bending test

Figure 3.18-a shows a glass-epoxy beam under a four-point bending test. It is formed by a central graded region of length 37 mm, flanked by two pieces made of pure epoxy (on the left) and glass-rich (on the right) materials. In the graded region, material properties change according to a horizontal abscissa ξ, which varies from 0 to 1 by passing from the epoxy to the glass part. The beam is 120 mm long and has a rectangular cross-section of width 6 mm and height 22 mm, with a vertical notch d=5.5 mm at $\xi = 0.17$. Figure 3.18-b depicts the computational mesh adopted in the simulations, involving 318 plane stress triangular elements refined near the crack tip and coarse elsewhere. Furthermore, the stretching segment presents is discretized using three el-

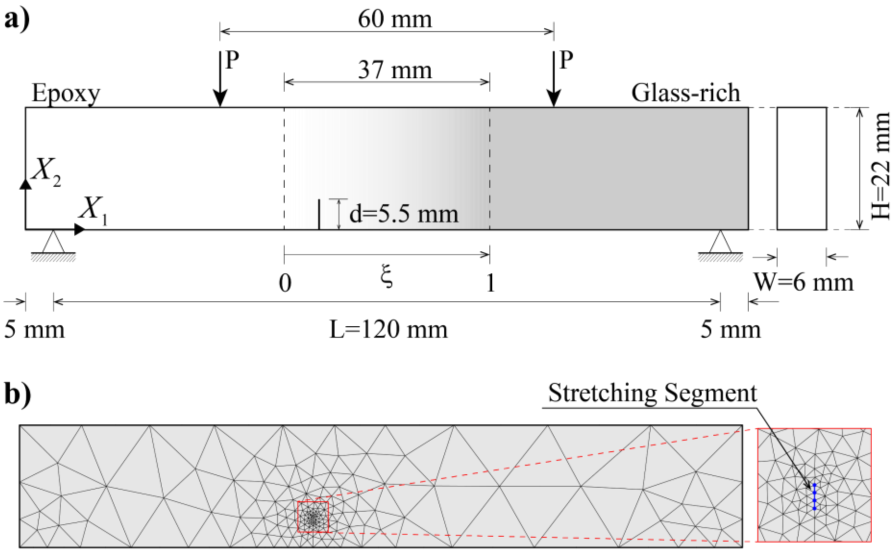

Figure 3.18. A notched glass-epoxy beam under a four-point bending test: (a) geometry and boundaries conditions; (b) initial mesh configuration employed in the analysis.

ements. Table 3.3 reports Young's Modulus, Poisson's ratio, and fracture toughness for different ξ. The material properties have been implemented through piecewise functions in terms of X_1 (*i.e.*, the horizontal global coordinate starting from the bottom-left extremity of the beam (see Figure 3.18-a)). In the graded region, these properties vary according to linear interpolation functions, whereas along the side portions of the beam, they remain constant (Figure 3.19).

Rousseau and Tippur (Rousseau and Tippur, 2000) have investigated the beam experimentally, reporting the crack path picture and the crack initiation angle (θ_0). These results represent an important benchmark that several Authors have referred to assess their numerical procedures on crack growth phenomena in FGMs. Kim and Paulino (Kim

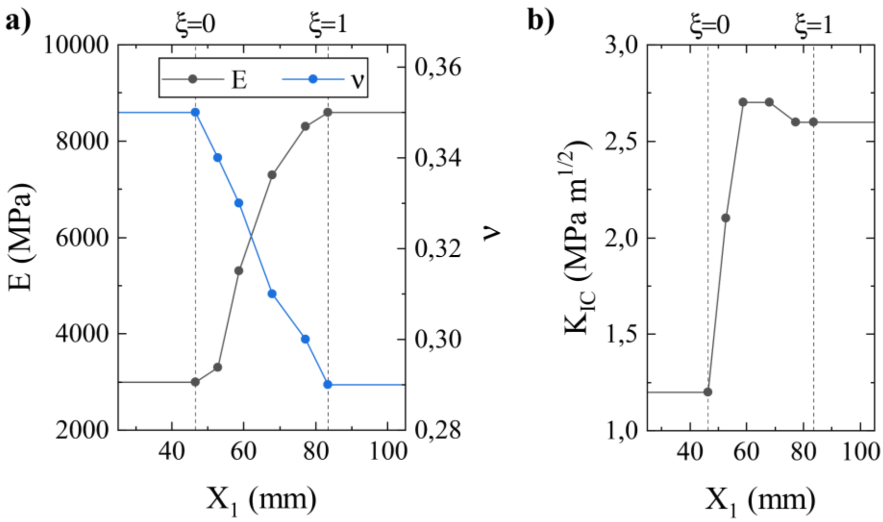

Figure 3.19. A notched glass-epoxy beam under a four-point bending test: functions implemented in the numerical model to accounting for graded variation of material properties in terms of (a) Young's Modulus (E), Poisson ratio (ν) and (b) Fracture toughness (K_{IC}).

Table 3.3 – A notched glass-epoxy beam under a four-point bending test: variation of material properties inside the graded region.

ξ	*E (MPa)*	ν	K_{IC} *(MPa* $\sqrt{m}$*)*
0.00	3000	0.35	1.2
0.17	3300	0.34	2.1
0.33	5300	0.33	2.7
0.58	7300	0.31	2.7
0.83	8300	0.30	2.6
1.00	8600	0.29	2.6

and Paulino, 2007) adopted a FE framework based on an automatic crack growth algorithm, while Ooi et al. (Ooi et al., 2015) used the Scaled Boundary Finite Element Method (SB-FEM). Figure 3.20-a

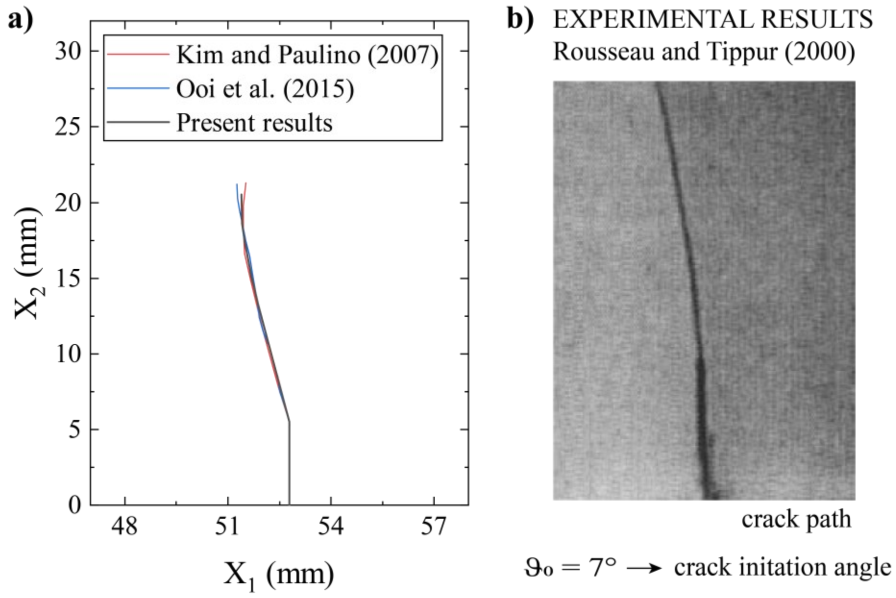

Figure 3.20. A notched glass-epoxy beam under a four-point bending test: (a) a comparison in terms of crack paths between the present method and numerical results obtained by Kim and Paulino (Kim and Paulino, 2007), and Ooi et al. (Ooi et al., 2015); (b) experimental results provided by Rousseau and Tippur (Rousseau and Tippur, 2000).

Table 3.4 – A notched glass-epoxy beam under a four-point bending test: values of crack initiation angle (θ_0) and maximum carrying load (P).

	θ_0 (°)	P (N)
Rousseau and Tippur (2000)	7	-
Kim and Paulino (2007)	6.98	249.3
Ooi et al. (2015)	6.82	247
Proposed method	7.07	248.2

compares the crack paths obtained through the proposed method with those achieved by Kim and Paulino (Kim and Paulino, 2007) and Ooi et al. (Ooi et al., 2015). In addition, Figure 3.20-b reports experimental

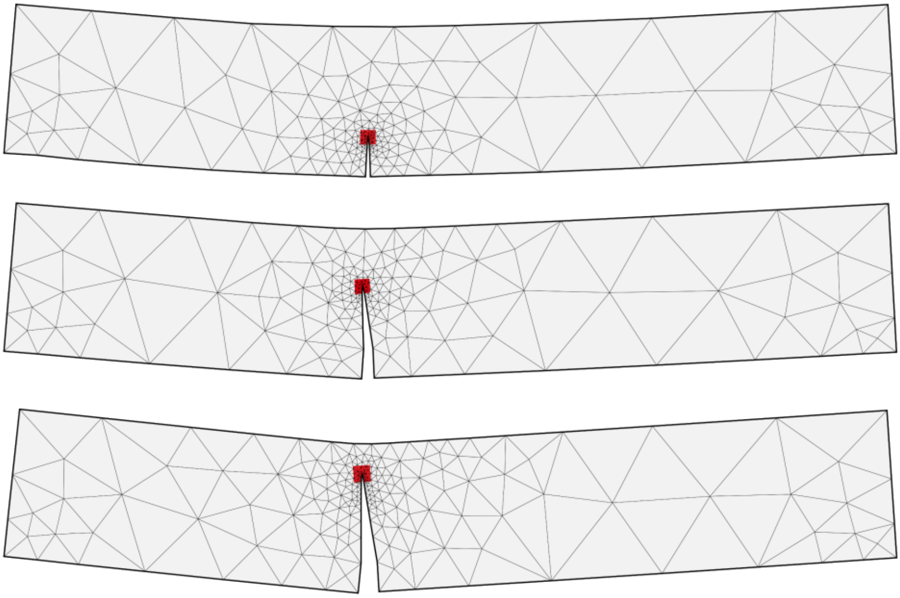

Figure 3.21. A notched glass-epoxy beam under a four-point bending test: a schematic view of the crack grow evaluation.

results provided by Rousseau and Tippur (Rousseau and Tippur, 2000). Table 3.4 resumes crack initiation angles (θ_0) and the maximum carrying loads (P). The present approach reproduces rather well crack paths predicted by other numerical strategies. Such predictions also agree with experimental data since the differences concerning θ_0 is about 1%. The accordance also occurs in terms of P because it differs from Kim and Paulino (Kim and Paulino, 2007) almost by 1% and for Ooi et al. (Ooi et al., 2015) such a difference is about 0.5%.

Figure 3.21 depicts three deforming shapes of the beam during the propagation process. The figure also reports the mark of the *q* function (highlighted in red) to represent schematically how the present method works. As shown, *q* follows the tip during the propagation.

For the current analysis, the function *q* had a pyramid shape with a square base of side a=0.2d.

3.4.1 Influence of the q function on the numerical solution

Additional analyses are developed to identify the best choice for the q-function that optimizes the convergence speed of the numerical solver. As described in Section 2.3, the function q (x_1, x_2) is an arbitrary function equal to the unity at the tip and zero at the outer edges of the integration domain. No requirements arise concerning the shape of q (x_1, x_2) from the theory. However, some studies show that the shape of q (x_1, x_2) is likely to affect computational performance. For homogeneous material, Shih et al. (Shih et al., 1986) have used both pyramid and plateau functions to calculate the *J*-integral in cracked strips under thermal loads, concluding that the shape of q (x_1, x_2) does not affect the accuracy of the numerical solution. Kuna (Kuna, 2013) has pointed out that plateau functions are less computationally expansive than pyramid ones. For FGMs, Kim and Paulino (Kim and Paulino, 2003) have used plateau functions for evaluating SIFs and T-stress.

Their numerical models do not concern moving mesh. Indeed, to the Author's knowledge, there are no studies that embedded the *M*-integral in crack propagation procedures based on the ALE techniques.

The parametric study analyzed the beam using pyramid and plateau functions with variable square base sides. The investigation firstly examines plateau functions square base with length a=0.2d and variable upper square bases a'. The analysis assumed a' equal to 0.025d, 0.05d,

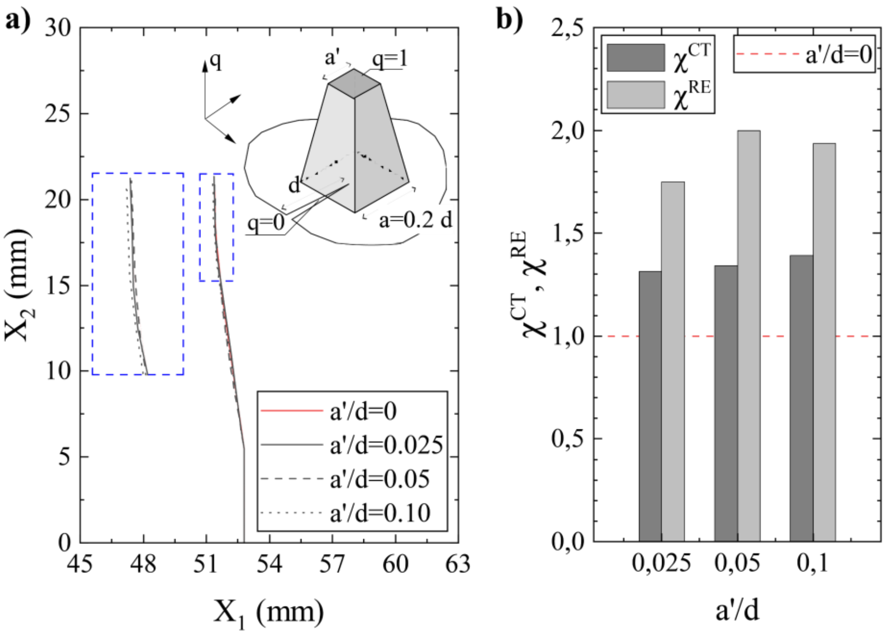

Figure 3.22. A notched glass-epoxy beam under a four-point bending test: comparisons in terms of (a) crack paths and (b) percentage variation of the computational time and the number of remeshing for variable plateau functions.

and 0.1d. Figure 3.22-a compares crack paths, while Figure 3.22-b reports the values concerning χ^{CT} and χ^{RE} evaluated through the equation (3.1), where the results of Figure 3.20-a are assumed as a reference.

The crack trajectories are almost equivalent, thus confirming that the shape of q (x_1, x_2) does not affect accuracy. However, it influences the computational efficiency: χ^{RE} doubles for a'=0.025d and a'=0.05d and increases of 1.75 for a'=0.025d, while χ^{CT} is about 1.3 in all cases. The data denote that pyramid functions may represent the optimum choice for improving efficacy in the prediction of fracture variables.

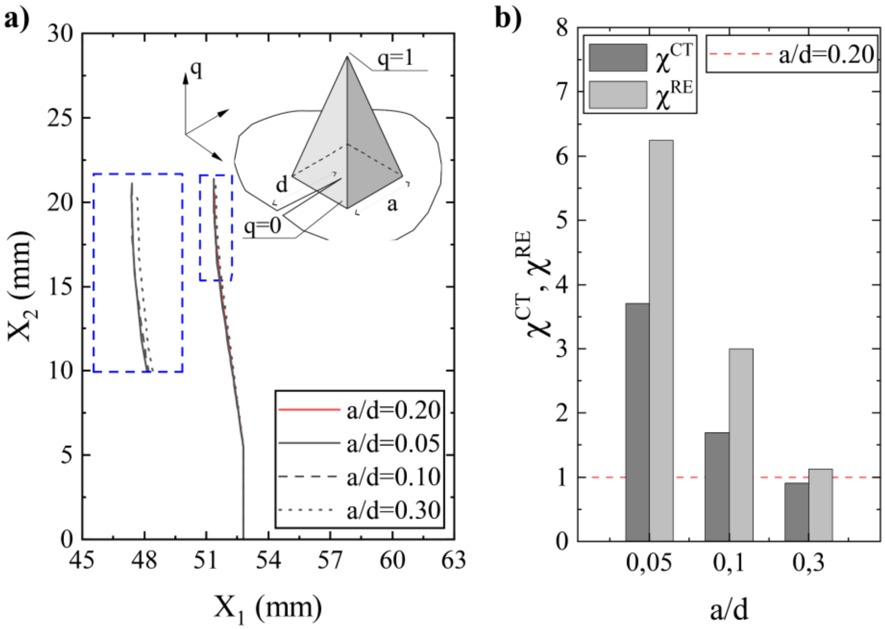

Figure 3.23. A notched glass-epoxy beam under a four-point bending test: comparisons in terms of (a) crack paths and (b) percentage variation of computational time and number of remeshing for variable square pyramid functions.

Now, the study focuses on pyramid functions of different base sides a. The analysis assumed a equal to 0.05d, 0.1d, and 0.3d. Figure 3.23-a depicts the crack trajectories, while Figure 3.23-b reports χ^{CT} and χ^{RE}. Also these cases, the crack paths are quite similar, whereas the computational efficiency improves as far as the base sides increase. This is likely to occur because the total number of triangular elements introduced in the integration domain increases, thus improving the accuracy and convergence speed of the solving procedure. Values larger than 0.3d do not increase the computational efficiency much because χ^{CT} and χ^{RE} are equal to 1. Moreover, larger values of the side a might reduce

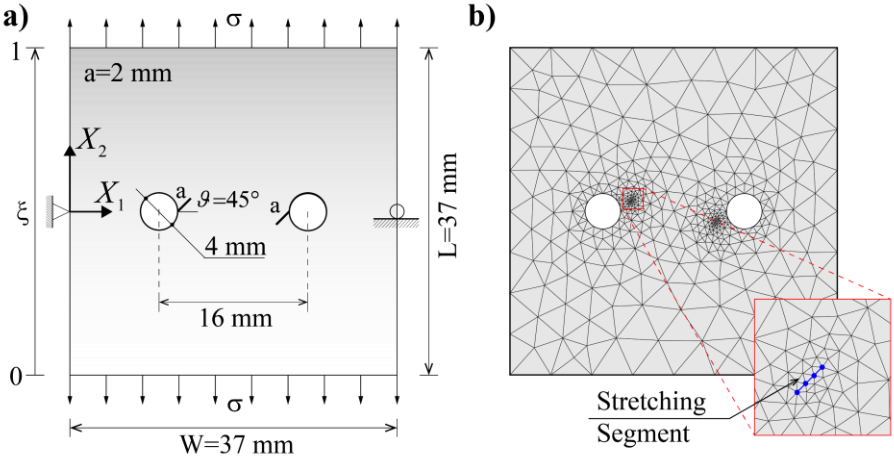

Figure 3.24. A glass-epoxy plate with two cracks emanating from two holes: (a) a schematic of geometry and boundary conditions; (b) initial mesh configuration used in the analysis.

the pre-crack excessively, thus leading to differences in crack paths and fracture behavior predictions. Then, the results suggest that the best choice for q (x_1, x_2) may be a square pyramid with a base of 0.2-0.3 d.

3.5 A glass-epoxy plate with two cracks emanating from two holes

Figure 3.24-a shows a glass-epoxy square plate of side 37 mm that presents two circular holes of diameter 4 mm placed symmetrically to the vertical central axis (the horizontal distance between the centers of the holes is 16 mm). Two cracks of 2 mm with angles π/4 and 5/4π arise from the left and right holes. Two hinges constrain the displacements of the midpoints of vertical boundaries. Tractions act on the upper and bottom edges. The material properties are equal to those

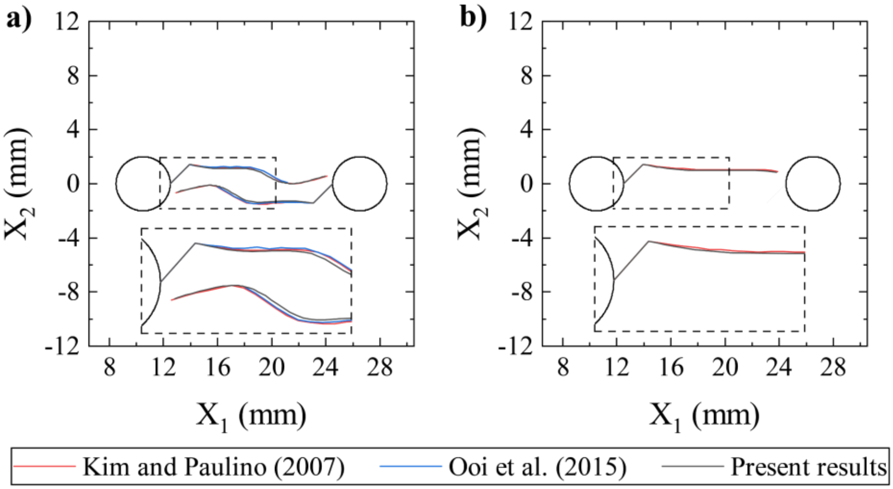

Figure 3.25. A glass-epoxy plate with two cracks emanating from two holes: comparisons in terms of crack paths for (a) Case A and (b) Case B.

adopted for the graded beam (see Table 3.3), but in this case, the material gradation occurs vertically along with the entire height of the plate (ξ=0 corresponds to the bottom boundary and ξ=1 to the top one).

Figure 3.24-b illustrates the computational mesh adopted for the analysis, which comprises 760 plane stress triangular elements arranged fine near the crack tips and coarse elsewhere. The edge of the holes includes 12 segments to properly discretize the circle, while both stretching segments consist of three elements (see zoomed picture).

Kim and Paulino (Kim and Paulino, 2007) and Ooi et al. (Ooi et al., 2015) have simulated the crack propagation through the same procedure employed for the graded beam discussed in the previous Section 3.4. In particular, Kim and Paulino (Kim and Paulino, 2007) have considered two fracture schemes. The first (Case A) involves the simultaneous propagation of both cracks. In particular, the cracks propagate

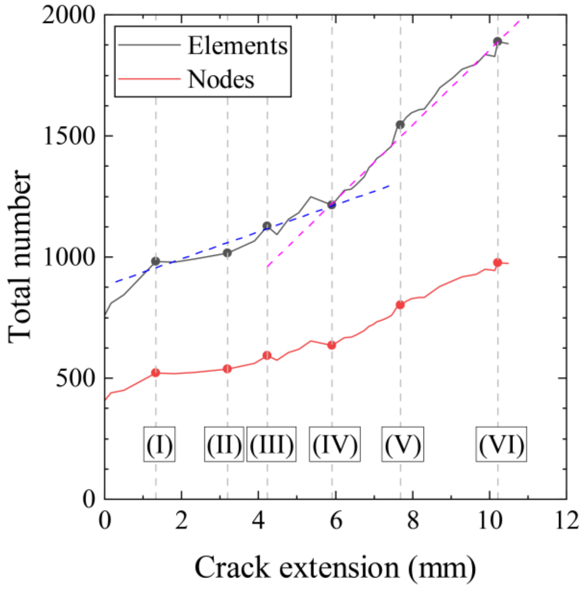

Figure 3.26. A glass-epoxy plate with two cracks emanating from two holes: variation of the total number of nodes and triangular elements during the propagation for Case A.

together even though both crack fronts do not satisfy onset conditions simultaneously.

The second (Case B) reproduces effective fracture conditions, so cracks propagate independently and only if the crack fronts meet onset conditions. Noting that Ooi et al. (Ooi et al., 2015) have simulated only Case A. The proposed method analyzes both fracture mechanics.

Figure 3.25 compares the crack paths gained through the present method with those predicted by Kim and Paulino (Kim and Paulino, 2007) and Ooi et al. (Ooi et al., 2015). In particular, Figure 3.25-a shows the results for Case A, while Figure 3.25-b depicts the results for Case

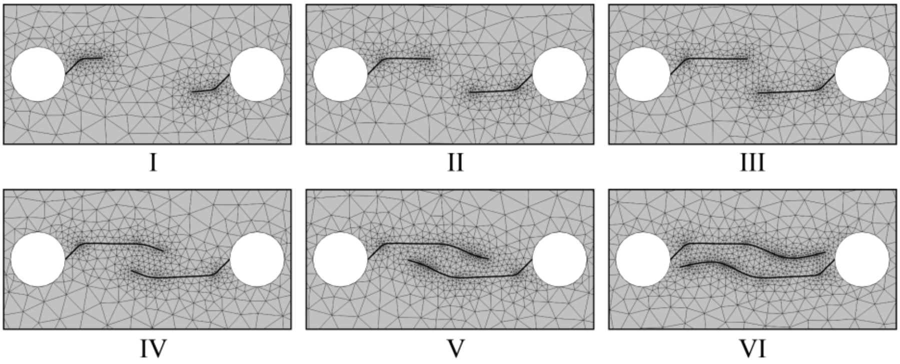

Figure 3.27. A glass-epoxy plate with two cracks emanating from two holes: snapshots of the mesh configuration during the propagation for Case A.

B. As one can see, the proposed methodology reproduces rather well crack paths obtained by other Authors.

For Case A, detailed results are proposed. In this case, crack paths are quite complicated, as evidenced by the several kinks in the propagation direction. Hence, it could be helpful to highlight the ability of the proposed method to refine the mesh during the analysis because of complex trajectories. This property derives from the workflow of the proposed procedure. As discussed in Section 2.4.2, when the variation angle of the stretching segment concerning the pre-existing crack reaches the established threshold, the procedure updates the model's geometry using the configuration achieved during the last analysis step. This process leads to a new stretching segment (inserting another mesh point near the crack tip) and new meshing operations.

Figure 3.26 reports the total number of elements and nodes as a function of the crack extension. Figure 3.27 depicts six snapshots of the

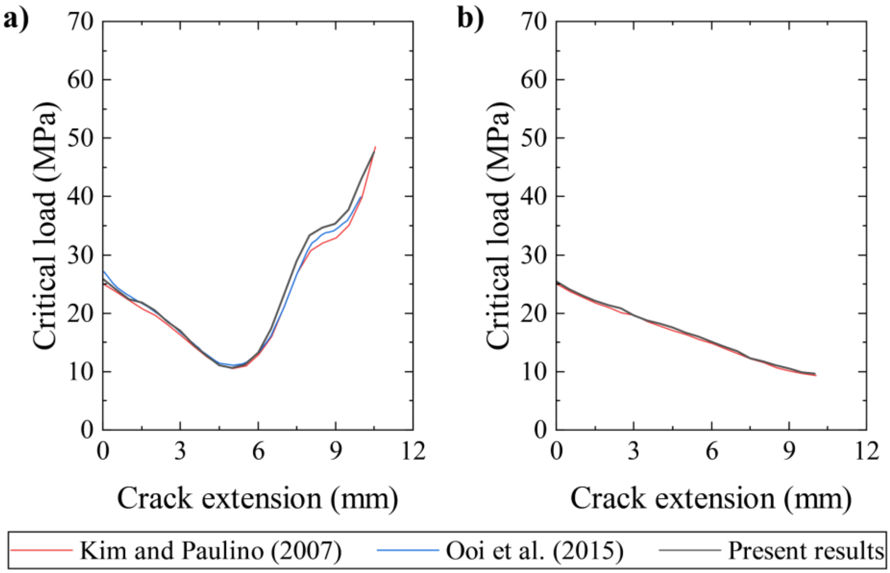

Figure 3.28. A glass-epoxy plate with two cracks emanating from two holes: comparisons in terms of critical loads for (a) Case A and (b) Case B.

mesh corresponding to the analysis steps marked by Roman numerals in Figure 3.26. The results denote that the elements in the mesh configurations increase with two growth rates (blue and magenta dashed lines in Figure 3.26). The first trend (blue line) is moderate because the cracks advance horizontally, as shown in snapshots I, II, and III. In these steps, the increment of elements and nodes may be due to remeshing processes caused by elevated element distortions. The second trend (magenta line) is steep and occurred because of the bending of crack paths. Further increments may arise because of the superimposing of the crack trajectories. These results have highlighted the strength of the proposed method to refine the mesh exclusively when necessary. This ability permits to save considerable computational resources.

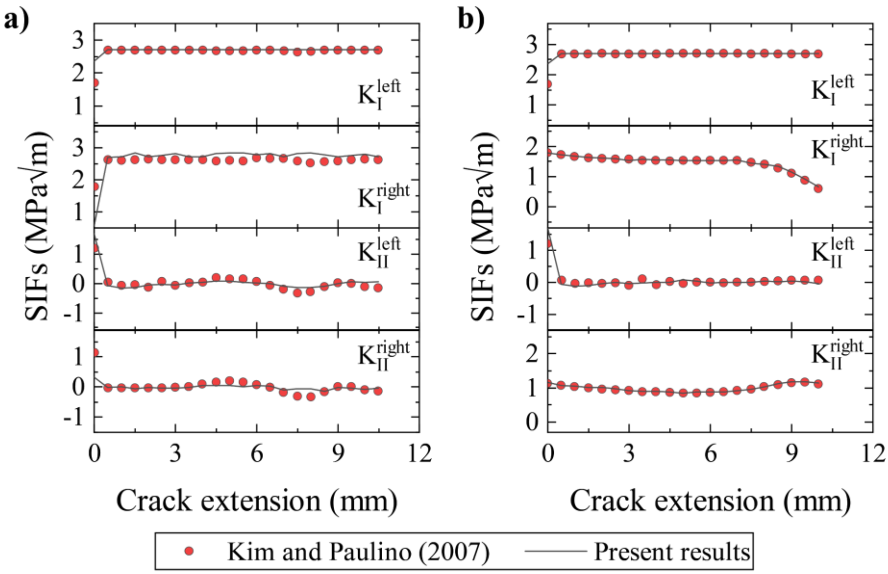

Figure 3.29. A glass-epoxy plate with two cracks emanating from two holes: comparisons in terms of SIFs for (a) Case A and (b) Case B.

The following results represent an adequate test to assess the potency of the proposed method. Figure 3.28-a and b report the critical load versus the crack extension for Cases A and B, respectively. Firstly, Case A is analyzed. The critical load decreases linearly for crack extension up to 5 mm. After, it increases, reaching the maximum value of 50 MPa. All numerical methods predicted the same trend but diverged slightly only in the final part of the graph. Such differences between the proposed approach and those developed by Ooi et al. (Ooi et al., 2015) and Kim and Paulino (Kim and Paulino, 2007) are equal to 6% and 9%, respectively, thus being quite reliable from the numeric point of view. The present method also accurately reproduces the critical load for Case B (see Figure 3.28-b). As one can see, it decreases linearly.

Further comparisons concern the SIFs extracted during the propagation. Figure 3.29-a and b compare the SIFs for Cases A and B, respectively, between the proposed method and the procedure used by Kim and Paulino (Kim and Paulino, 2007). As shown, the predicted SIFs are in good agreement with Kim and Paulino (Kim and Paulino, 2007). Note that they adopted singular elements arranged radially around the crack tip to improve accuracy. Therefore, these results also denote the accuracy of the ALE formulation of the *M*-integral in extracting the SIFs from a movable crack front inside a heterogeneous material.

3.6 A glass-epoxy plate with branched cracks subjected to uniform tension

Figure 3.31-a shows a square plate of side 37 mm subjected to branched cracks under a uniform tension load. The plate presents a notch formed by a horizontal segment of 3 mm followed by two branches of 1.5 mm inclined at $\pm\pi/4$ with respect to the horizontal. Boundary conditions include three adjoining hinges that limit the displacements of the midpoint of the right vertical boundary. The external load consists of uniform tractions acting on the top and bottom boundaries. The material properties are the same used in the previous section. Figure 3.31-b reports the initial mesh configurations used for the analysis. It comprises 905 nodes and 1736 plane stress triangular elements arranged finely near the crack tip and coarse elsewhere in the remaining part of the domain. Both the stretching segments have four elements, as shown in the zoomed view.

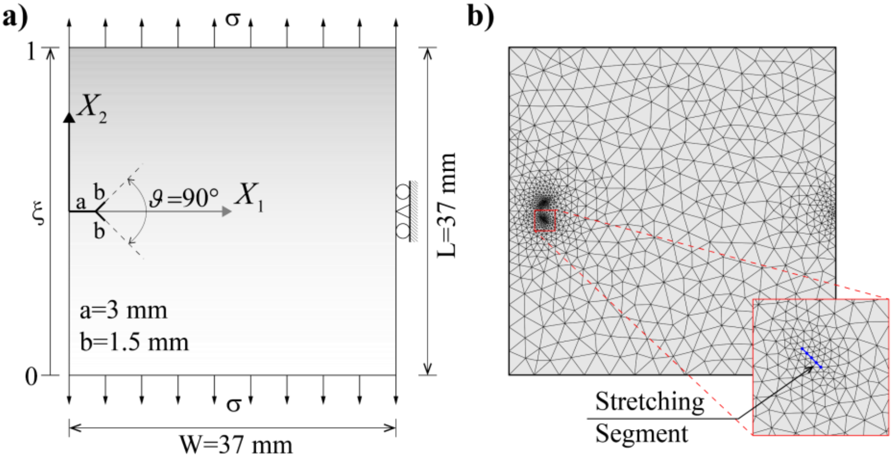

Figure 3.31. A glass-epoxy plate with branched cracks subjected to uniform tension: (a) geometry and boundary conditions; (b) initial mesh configuration adopted for the analysis.

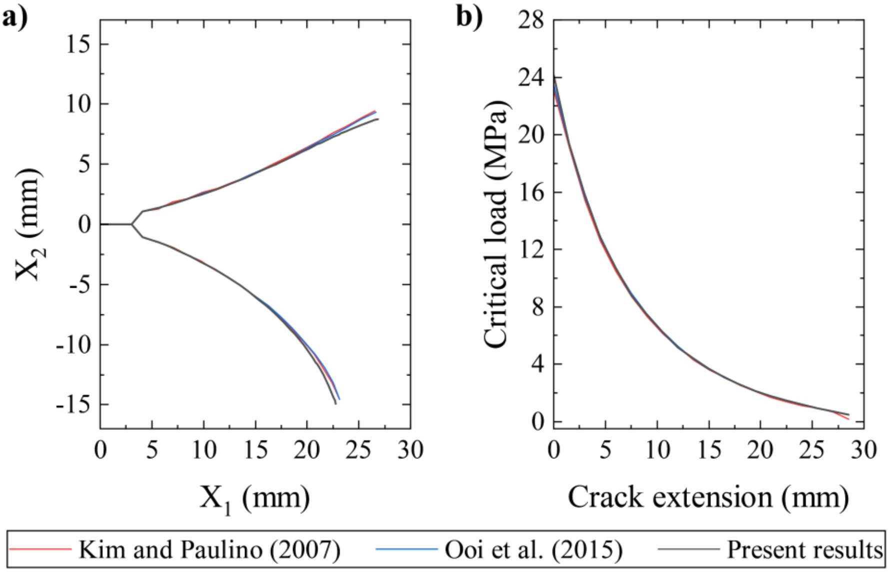

Figure 3.30. A glass-epoxy plate with branched cracks subjected to uniform tension: comparisons in terms of (a) crack path and (b) critical load.

Kim and Paulino (Kim and Paulino, 2007) and Ooi et al. (Ooi et

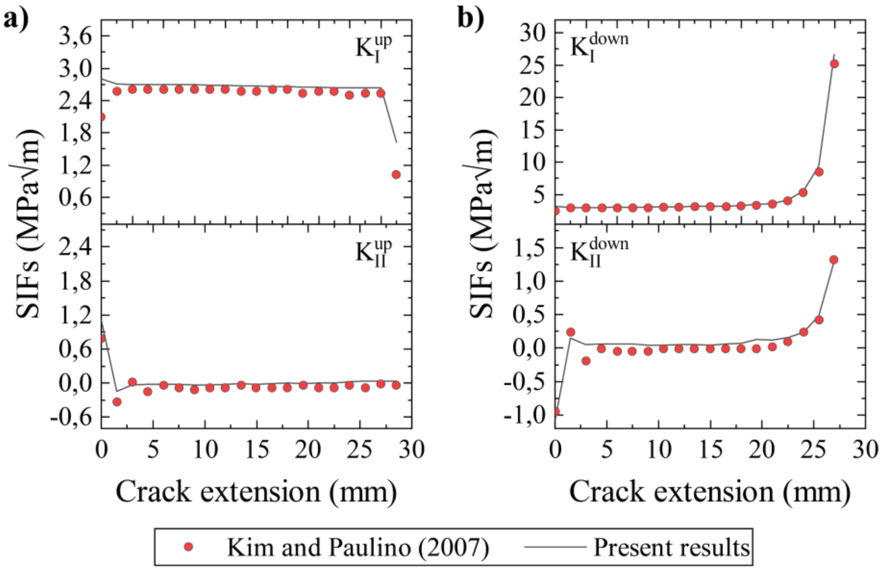

Figure 3.32. A glass-epoxy plate with branched cracks subjected to uniform tension: comparisons in terms of SIFs vs (a) upper and (b) down extensions.

al., 2015) have reproduced the crack propagation through the numerical procedure described in the previous section, considering only Case A.

Figure 3.30 compares the results achieved through the proposed method with those reported by Kim and Paulino (Kim and Paulino, 2007) and Ooi et al. (Ooi et al., 2015). Figure 3.30-a shows the plot of the crack paths, while Figure 3.30-b depicts the critical load versus the upper front extension. The results agree quite well with the predictions of other numerical procedures, thus highlighting the reliability of the present approach to simulate crack branching. Figure 3.32 illustrates the SIFs extracted during the propagation. Note that only Kim and Paulino (Kim and Paulino, 2007) reported the evolution of SIFs in terms of crack extensions. The results denote that the present method agrees with

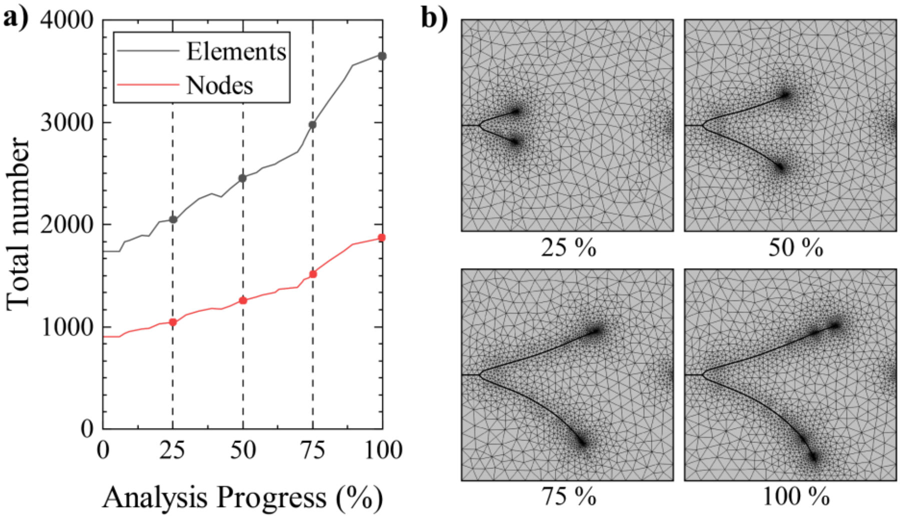

Figure 3.33. A glass-epoxy plate with branched cracks subjected to uniform tension: (a) variation of the total number of nodes and triangular elements and (b) snapshots of the mesh configuration during the propagation.

the literature's available data. Slight differences may be attributed to the finite element typology employed in the simulations.

3.6.1 Influence of mesh discretization on the numerical solution

Like the homogeneous beam reported in Section 3.1, the following study aims to assess the influence of the mesh discretization adopted in the numerical model for analyzing the failure behavior of FGMs material. Figure 3.33-a reports the evolution of the mesh configuration during the propagation in terms of the total number of finite elements and nodes as a function of the analysis progress. Figure 3.33-b shows snapshots of the mesh configuration at each 25% step of the analysis. As previously mentioned, the mesh refines during propagation. In particular, the elements have two different growth rates: the first is moderate and takes place between 0% and 75%; the second is steep and occurs during the last step of the analysis. This sudden growth probably emerges because of the vicinity of the crack tip to the bottom boundary of the plate (see snapshots corresponding 75% and 100%). At the end of the analysis, the number of elements and nodes has doubled compared to the initial configuration. Notably, their growth negatively affects computational efficiency because dense meshes spend relevant computer efforts to run the entire simulation. However, the possible recourse to remeshing procedures may be expensive since it further increases computational costs. In the proposed strategy, the ALE technique limits remeshing events, thus saving computational resources. In addition, the developed approach guarantees accurate results by using unrefined mesh configurations because it updates the geometry during the propagation when the variation angle of the stretching segment reaches a pre-established threshold value.

To better understand these abilities, a parametric study is developed using the mesh configurations illustrated in Figure 3.34 and marked as Mesh M2, Mesh M3, and Mesh M4, respectively (the mesh in Figure 3.31-b is identified in the sequel as Mesh M1). Mesh M2 involves 811 triangular elements arranged finely near the crack tip and coarse elsewhere. Mesh M3 is rougher than Mesh M2 and Mesh M1 since it comprises 393 triangular elements placed roughly elsewhere. However, like Mesh M1, Mesh M2 and Mesh M3 have branches discretized by four elements. Finally, Mesh M4 comprises almost the same number of finite elements as Mesh M1 but has a stretching segment with only two elements. Table 3.5 summarizes the statistics of such meshes.

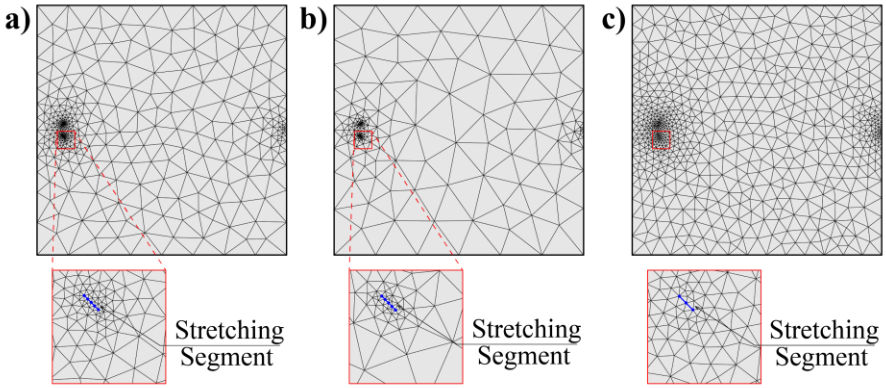

Mesh M2 Mesh M3 Mesh M4

Figure 3.34. A glass-epoxy plate with branched cracks subjected to uniform tension: a schematic of (a) Mesh M2, (b) Mesh M3 and (c) Mesh M4.

Figure 3.35 reports the crack trajectories achieved with different mesh configurations. The results denote that the present method ensures accuracy regardless of the discretization adopted since the crack paths are similar. However, similarly as discussed in Section 3.1.1, the following percentage variations are defined:

Table 3.5 – A glass-epoxy plate with branched cracks subjected to uniform tension: details of the meshes employed in the parametric analysis.

Type	Triangular Elements				Stretching segment		
	DOFs	Number	Maximum size (mm)	Minimum size (mm)	Number of elements	Maximum size (mm)	Minimum size (mm)
M1	905	1736	3.166	0.090	4	0.113	0.113
M2	429	811	5.498	0.098	4	0.113	0.113
M3	214	393	7.313	0.089	4	0.113	0.113
M4	705	1337	3.379	0.141	2	0.225	0.225

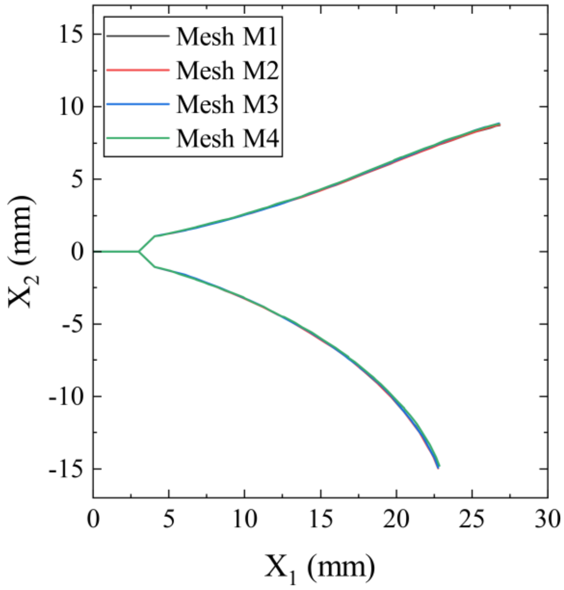

Figure 3.35. A glass-epoxy plate with branched cracks subjected to uniform tension: crack paths obtained with different mesh configurations.

$$\begin{cases} \mathrm{Var}_i^{CT} = \dfrac{CT_i - CT_1}{CT_1}[\%] \\ \mathrm{Var}_i^{RE} = \dfrac{RE_i - RE_1}{RE_1}[\%] \end{cases} \qquad i = 2,3,4 \tag{3.2}$$

where, (CT_i, RE_i) and (CT_R, RE_R) represent the computational time and number of remeshing events involved by the *i*-th investigated mesh and the one taken as reference (Mesh M1), respectively. Table 3.6 reports the percentage variations. The computational time reduces as the mesh configurations become coarser. Mesh M2 reduces CT by -38.93%, while Mesh M3 is about -50.84%. Mesh M4, even if it has almost the same number of elements and nodes as Mesh M1, spent

Table 3.6 – A glass-epoxy plate with branched cracks subjected to uniform tension: comparisons in terms of computational time (CT) and total number of remeshing events (RE).

Mesh	Var^{CT} (%)	Var^{RE} (%)
M2	-38.93	-9.02
M3	-50.84	-12.30
M4	90.84	-50.00

+90.84% of CT. This growth may be related to the coarse mesh around the crack tip. Unrefined meshes may induce convergence issues during remeshing processes. Indeed, during the analysis performed with Mesh M4, it was observed that the model suffered from convergence problems whenever remeshing occurred. Such difficulties affect the analysis, but it does not lead to convergence issues during the simulation. On the other hand, Mesh M4 has involved -50% of RE, while Mesh M3 and Mesh M2 -12.3% and -9.02%, respectively. The result of Mesh M4 could depend on the coarser mesh adopted for the stretching segment, as larger elements involve fewer remeshing actions. However, this benefit cannot compensate for the considerable time spent due to convergence problems. These considerations have highlighted that the present procedure does not require refined meshes to ensure accurate predictions.

4

Dynamic fracture analysis in quasi-brittle materials

The present chapter generalizes the modeling approach presented in Chapter 2 to the context of dynamic Fracture Mechanics for simulating crack propagation phenomena in quasi-brittle materials. It focuses attention on the ALE formulation of the dynamic *M*-integral to extract Dynamic Stress Intensity Factors (DSIFs) at a crack front that grows dynamically. The structure of the chapter is as follows: (*i*) the first part provides the theoretical background of the proposed methodology; (*ii*) the second treats numerical implementation aspects; (*iii*) finally, the last one reports comparisons between analytic, experimental, and numerical results to assess the efficiency and accuracy of the proposed procedure.

4.1 Theoretical background

4.1.1 ALE formulation

ALE serves as effective tool to trace the geometry evolution of the computational domain caused by the advance of internal defects. Precisely, the mesh nodes change their position during the crack growth according to the conditions dictated by classic Fracture Mechanics criteria in terms of crack onset conditions, crack propagation direction, and crack tip velocity. In addition, since the quantities involved are now time-varying, it is necessary relating the time derivatives of vectorial fields in material and referential systems. To this end, let the material and referential time derivatives of vectorial field **v** (expressed in the Material and Referential frame as $\mathbf{v}^M(\mathbf{X},t)$ and $\mathbf{v}^R(\boldsymbol{\chi},t)$) can be written, respectively, as follows:

$$\begin{aligned} \dot{\mathbf{v}}^M &= \frac{\partial}{\partial t}\mathbf{v}^M\left(\mathbf{X},t\right)\Big|_{\mathbf{X}} \\ \dot{\mathbf{v}}^R &= \frac{\partial}{\partial t}\mathbf{v}^R\left(\boldsymbol{\chi},t\right)\Big|_{\boldsymbol{\chi}} \end{aligned} \tag{4.1}$$

These time derivatives are related through the chain rule:

$$\frac{\partial}{\partial t}\mathbf{v}^R\left(\boldsymbol{\chi},t\right)\Big|_{\boldsymbol{\chi}} = \frac{\partial}{\partial t}\mathbf{v}^M\left(\mathbf{X},t\right)\Big|_{\mathbf{X}} + \frac{\partial \mathbf{v}^M}{\partial \mathbf{X}}\frac{\partial \mathbf{X}}{\partial t}\Big|_{\boldsymbol{\chi}} \rightarrow \dot{\mathbf{v}}^R = \dot{\mathbf{v}}^M + \nabla^M \mathbf{v}^M \dot{\mathbf{X}}^R \tag{4.2}$$

where, $\dot{\mathbf{X}}^R$ is a convective term denoting the velocity of the mesh in the material domain. It has little significance from a physical point of view, but it has a computational importance since numerical solvers compute and store in the solution vector referential time derivative only.

Eq. (4.2) can be expressed into referential coordinates through Eq. (2.14), as follows:

$$\dot{\mathbf{v}}^M = \dot{\mathbf{v}}^R - \nabla^R \mathbf{v}^R \, \mathbf{J}_{\boldsymbol{\Psi}}^{-1} \, \dot{\mathbf{X}}^R \tag{4.3}$$

The second time derivatives concerning Material and Referential frames can be evaluated by applying Eq. (4.3) recursively, thus achieving:

$$\begin{aligned} \ddot{\mathbf{v}}^M &= \ddot{\mathbf{v}}^R - 2\nabla^R \dot{\mathbf{v}}^R \, \mathbf{J}_{\boldsymbol{\Psi}}^{-1} \, \dot{\mathbf{X}}^R - \nabla^R \mathbf{v}^R \, \mathbf{J}_{\boldsymbol{\Psi}}^{-1} \, \ddot{\mathbf{X}}^R + \\ &+\nabla^R \left[\nabla^R \mathbf{v}^R \, \mathbf{J}_{\boldsymbol{\Psi}}^{-1} \right] \mathbf{J}_{\boldsymbol{\Psi}}^{-1} \, \dot{\mathbf{X}}^R \, \dot{\mathbf{X}}^R + \nabla^R \mathbf{v}^R \mathbf{J}_{\boldsymbol{\Psi}}^{-1} \nabla^R \dot{\mathbf{X}}^R \, \mathbf{J}_{\boldsymbol{\Psi}}^{-1} \, \dot{\mathbf{X}}^R \end{aligned} \tag{4.4}$$

4.1.2 Governing equations

The governing equations of the problem can be gathered into two groups: the first set involves the fundamental equations of solid mechanics to describe the mechanical behavior of the material solid, while the second one governs the motion of the nodes of the computational mesh.

According to the same considerations described in Section 2.1, the fundamental equations of solid mechanics are defined regarding a 2D homogeneous body (Figure 4.1). In this case, the crack propagates dynamically at a velocity $\dot{a}(t)$ along the propagation direction identified by the unit vector $\mathbf{n}_c$, inclined of $\theta_c(t)$ regarding the crack tip local coordinate system.

Similarly to Eq. (2.8), the variational weak form of the governing equation of the solid mechanics can be expressed as follows:

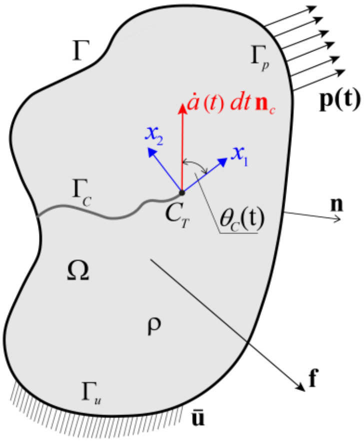

Figure 4.1. A 2D domain affected by a dynamically growing crack.

$$\int_{\Omega}[\mathbf{C}:\nabla\mathbf{u}]\nabla\delta\mathbf{u}\,d\Omega-\int_{\Omega}\mathbf{f}\delta\mathbf{u}\,d\Omega-\int_{\Gamma_p}\mathbf{p}\delta\mathbf{u}\,d\Gamma=-\int_{\Omega}\rho\ddot{\mathbf{u}}\delta\mathbf{u}\,d\Omega \qquad (4.5)$$

where, $\mathbf{C}$ is the fourth-order elastic tensor, $\mathbf{f}$ and $\mathbf{p}$ are the body force and surface traction vectors, respectively, and ρ is the mass density. Besides, $\mathbf{u}$ and $\delta\mathbf{u}$ represent the displacement field and a suitable set of virtual displacements defined in Eq. (2.9).

Eq. (4.5) must be stated with reference to the Referential system. According to Eq. (2.14), the left-hand side of Eq. (4.5) becomes:

$$\begin{aligned}&\int_{\Omega_R}\left\{\left[\mathbf{C}:\nabla^R\mathbf{u}^R\,\mathbf{J}_{\boldsymbol{\Psi}}^{-1}\right]\nabla^R\delta\mathbf{u}^R\,\mathbf{J}_{\boldsymbol{\Psi}}^{-1}\right\}\bar{J}_\Omega d\Omega_R+\\&\qquad-\int_{\Omega_R}\left\{\mathbf{f}\delta\mathbf{u}^R\right\}\bar{J}_\Omega d\Omega_R+\int_{\Gamma_p^R}\left\{\mathbf{p}\delta\mathbf{u}^R\right\}\bar{J}_S dS_R\end{aligned} \qquad (4.6)$$

Instead, using Eq. (4.4), the right-hand side of Eq. (4.5) becomes:

$$
\begin{aligned}
&-\int_{\Omega_R}\left[\rho\left(\ddot{\mathbf{u}}^R-2\nabla^R\dot{\mathbf{u}}^R\mathbf{J}_{\boldsymbol{\Psi}}^{-1}\,\dot{\mathbf{X}}^R-\nabla^R\mathbf{u}^R\mathbf{J}_{\boldsymbol{\Psi}}^{-1}\,\ddot{\mathbf{X}}^R\right)\delta\mathbf{u}^R\right]\bar{J}_\Omega d\Omega^R+\\
&-\int_{\Omega_R}\left[\rho\left(\nabla^R\left[\nabla^R\mathbf{u}^R\mathbf{J}_{\boldsymbol{\Psi}}^{-1}\right]\mathbf{J}_{\boldsymbol{\Psi}}^{-1}\,\dot{\mathbf{X}}^R\,\dot{\mathbf{X}}^R\right)\delta\mathbf{u}^R\right]\bar{J}_\Omega d\Omega^R+\\
&-\int_{\Omega_R}\left[\rho\left(\nabla^R\mathbf{u}^R\mathbf{J}_{\boldsymbol{\Psi}}^{-1}\,\nabla^R\dot{\mathbf{X}}^R\,\mathbf{J}_{\boldsymbol{\Psi}}^{-1}\dot{\mathbf{X}}^R\right)\delta\mathbf{u}^R\right]\bar{J}_\Omega d\Omega^R
\end{aligned}
\tag{4.7}
$$

In Eqs. (4.6)-(4.7) $\mathbf{u}^R$ and $\delta\mathbf{u}^R$ are the displacement and virtual displacements fields expressed in the referential domain, Ω_R is the area of the body in the referential domain, Γ_p^R is the boundary region affected by external tractions in the referential configuration, while $\bar{J}_\Omega$ and $\bar{J}_S$ represent the Jacobian related to the volume and area.

The basic equations of the moving mesh are expressed in terms of the Laplacian smoothing method (see Section 2.2). In this context, the boundary conditions for solving Laplace equations can be summarized as follows:

$$
\begin{aligned}
&\dot{\bar{\mathbf{x}}}\cdot\mathbf{n}_c=\dot{a}\quad \text{at}\quad C_T\\
&\bar{\mathbf{x}}=0\quad \text{on}\quad \Gamma
\end{aligned}
\tag{4.8}
$$

where, $\dot{\bar{\mathbf{x}}}$ is the time derivative of nodal mesh displacement vector function $\bar{\mathbf{x}}$. In Eq. (4.8), the first condition imposes that the mesh node of the crack tip moves along the direction of propagation $\mathbf{n}_\mathrm{c}$ at speed equal to the crack tip velocity $\dot{a}$. The second condition requires no mesh displacements along the external boundary of the domain. Noting that both $\mathbf{n}_\mathrm{c}$ and $\dot{a}$ can be defined using any fracture criteria of Fracture Mechanics. Regarding the crack tip velocity, suitable expressions consistent with experimental results are those proposed by Freund (Freund, 1990).

Finally, by combining Eq. (2.21) and Eq. (4.8) through the Lagrangian Multipliers Method (LMM), the weak form of Laplacian smoothing in the Referential frame assumes the following expression:

$$\begin{aligned}\int_{\Omega_R}\left[\nabla^R(\mathbf{x})\mathbf{J}_{\boldsymbol{\Psi}}^{-1}\right]\cdot\left[\nabla^R(\delta\mathbf{x})\mathbf{J}_{\boldsymbol{\Psi}}^{-1}\right]\bar{J}_{\Omega}d\Omega_R &+ \\ +\left[\delta(\boldsymbol{\lambda}\cdot\mathbf{n}_c)\left(\dot{\bar{\mathbf{x}}}\cdot\mathbf{n}_c-\dot{a}\right)+(\boldsymbol{\lambda}\cdot\mathbf{n}_c)\delta\left(\dot{\bar{\mathbf{x}}}\cdot\mathbf{n}_c\right)\right]_{\mathbf{X}=\mathbf{X}_{C_T}} &+ \\ +\int_{\Gamma_R}\left[\delta(\boldsymbol{\lambda})\cdot\bar{\mathbf{x}}+\boldsymbol{\lambda}\cdot\delta(\bar{\mathbf{x}})\right]\bar{J}_{\Gamma}d\Gamma_R &= 0\end{aligned} \tag{4.9}$$

4.1.3 Interaction Integral method

The dynamic form of the *M*-integral is used to evaluate the Dynamic Stress Intensity Factors (DSIFs), which are fundamental parameters for defining crack onset conditions, the direction of propagation, and crack tip velocity.

To derive the dynamic *M*-integral expression, let us consider the analytical form of the dynamic *J*-integral, defined as follows ((Moran and Shih, 1987), (Yu and Kuna, 2021)):

$$J=\lim_{S_0\to 0}\int_{S_0}\left[(W+K)\delta_{1i}-\sigma_{ij}u_{j,1}\right]n_i dS \quad \text{with} \quad i,j=1,2 \tag{4.10}$$

where, *W* and *K* are the strain density and the kinematic energy density, respectively, defined as:

$$W=\frac{1}{2}\sigma_{ij}\varepsilon_{ij};\quad K=\frac{1}{2}\rho\dot{u}_j\dot{u}_j \tag{4.11}$$

in which, ρ and $\dot{u}_j$ are the mass density and velocity field, respectively. For computational reasons, Eq. (4.10) is usually converted into an Equivalent Domain Integral (EDI) form (for more clarification, see Section 2.3), thus obtaining the following expression:

$$\begin{aligned} J=&\int_A\left[\sigma_{ij}u_{i,1}-\frac{1}{2}\left(\sigma_{jk}\varepsilon_{jk}+\rho\dot{u}_j\dot{u}_j\right)\delta_{1i}\right]q_{,i}dA+\\ &\int_A\left[\left(\sigma_{ij}u_{i,1}\right)_{,i}-\frac{1}{2}\left(\sigma_{jk}\varepsilon_{jk}+\rho\dot{u}_j\dot{u}_j\right)_{,1}\right]qdA \end{aligned} \tag{4.12}$$

Also, by noting that $(\sigma_{ij}u_{j,1})_{,i}=\sigma_{ij,i}u_{j,1}+\sigma_{ij}u_{i,j1}=\sigma_{ij,i}u_{j,1}+\sigma_{ij}\varepsilon_{ij,1}$, $\sigma_{jk}\varepsilon_{jk,1}=C_{jklm}\varepsilon_{lm}\varepsilon_{jk,1}=\varepsilon_{jk}\sigma_{jk,1}=\varepsilon_{ij}\sigma_{ij,1}$, and $\sigma_{ij,j}=\rho\ddot{u}_i$, Eq. (4.12) simplifies as follows:

$$J=\int_A\left\{\left[\sigma_{ij}u_{i,1}-\frac{1}{2}\left(\sigma_{jk}\varepsilon_{jk}+\rho\dot{u}_j\dot{u}_j\right)\delta_{1i}\right]q_{,i}+\rho\left[\ddot{u}_iu_{j,1}-\dot{u}_{j,1}\dot{u}_j\right]q\right\}dA \tag{4.13}$$

Similar to what is reported in Section 2.3, the *M*-integral expression results by applying Eq. (4.13) to the superimposed state "act+aux", thus gaining $J^{act+aux}=J^{act}+J^{aux}+M$, in which *M* is the mutual term equal to:

$$\begin{aligned} M=&\int_A\left[\left(\sigma_{ij}^{act}u_{j,1}^{aux}+\sigma_{ij}^{aux}u_{j,1}^{act}\right)-\left(\sigma_{jk}^{act}\varepsilon_{jk}^{aux}+\rho\dot{u}_j^{act}\dot{u}_j^{aux}\right)\delta_{1i}\right]q_{,i}dA+\\ &+\int_A\left[\rho\left(\ddot{u}_j^{act}u_{j,1}^{aux}+\ddot{u}_j^{aux}u_{j,1}^{act}\right)-\rho\left(\dot{u}_{j,1}^{act}\dot{u}_j^{aux}+\dot{u}_{j,1}^{aux}\dot{u}_j^{act}\right)\right]qdA \end{aligned} \tag{4.14}$$

Usually, dynamic fracture problems have also been investigated using the auxiliary fields adopted for quasi-static fracture analysis. Employing Williams' asymptotic solutions determines that the auxiliary velocity $\dot{u}_i^{aux}$ and acceleration $\ddot{u}_i^{aux}$ fields are equal to zero, thus achieving the following simplified expression for the *M*-integral:

$$M=\int_A\left[\left(\sigma_{ij}^{act}u_{j,1}^{aux}+\sigma_{ij}^{aux}u_{j,1}^{act}\right)-\left(\sigma_{jk}^{act}\varepsilon_{jk}^{aux}\right)\delta_{1i}\right]q_{,i}dA+\int_A\rho\left(\ddot{u}_j^{act}u_{j,1}^{aux}\right)qdA \tag{4.15}$$

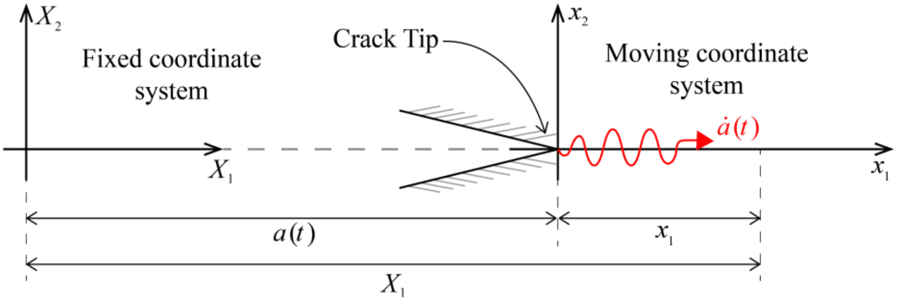

Figure 4.2. Auxiliary moving crack tip coordinate system according to Rice's analytical solutions.

However, the effect of non-zero crack propagation velocity on the *M*-integral can be adequately accounted for by assuming as auxiliary fields the analytic solutions regarding a steady-state propagation crack problem derived by Rice (Rice, 1968).

Figure 4.2 shows that these solutions are referred to as an advancing crack coordinate system (x_1, x_2), centered at the crack tip, that moves at constant velocity $\dot{a}$ with respect to a fixed coordinate system (X_1, X_2). These two coordinate systems are related by means of the following relationships:

$$\begin{cases} x_1 = X_1 - a(t) \\ x_2 = X_2 \end{cases} \tag{4.16}$$

where, $a(t)$ is the current crack propagation distance from the origin of the fixed frame. Considering the first relationship of Eq. (4.16), the material time derivative in the Referential coordinate of the displacement component u_i along the x_1 axis can be defined as:

$$\frac{du_i}{dt} = \frac{\partial u_i}{\partial t} - \frac{\partial u_i}{\partial x_1}\frac{\partial a}{\partial t} = \frac{\partial u_i}{\partial t} - \dot{a}\frac{\partial u_i}{\partial x_1} \tag{4.17}$$

In Eq. (4.17), $\partial u_i / \partial t$ is equal to zero under steady-state conditions, so one obtains:

$$\dot{u}_i = -\dot{a} u_{i,1}; \qquad \dot{u}_{i,1} = -\dot{a} u_{i,11} \tag{4.18}$$

Rice’s solutions are also valid when the propagation velocity varies with time ((Freund and Clifton, 1974), (Nilsson, 1974)). According to such condition, one derives the material time acceleration through the first relationship of Eq. (4.18), as follows:

$$\ddot{u}_i = -\frac{\partial \dot{a}}{\partial t} u_{i,1} - \dot{a}\dot{u}_{i,1} = -\ddot{a} u_{i,1} - \dot{a}\dot{u}_{i,1} \tag{4.19}$$

Eqs. (4.18)-(4.19) can be used to express the auxiliary velocity and acceleration fields in Eq. (4.14).

The *M*-integral expression (Eq. (4.14)) express in the Referential coordinate system is the following:

$$\begin{aligned}
M = &+\int_{A_R} \left(C_{ijkl} u^R_{k,h} \left(X^R_h \right)^M_{,n} \left(X^M_n \right)^C_{,l} u^{aux}_{j,1} \right) q_{,h} \left(X^R_h \right)^M_{,n} \left(X^M_n \right)^C_{,i} \bar{J}_A dA_R + \\
&+\int_{A_R} \left(\sigma^{aux}_{ij} u^R_{j,h} \left(X^R_h \right)^M_{,n} \left(X^M_n \right)^C_{,1} \right) q_{,h} \left(X^R_h \right)^M_{,n} \left(X^M_n \right)^C_{,i} \bar{J}_A dA_R + \\
&-\int_{A_R} \left(C_{jkpq} u^R_{p,h} \left(X^R_h \right)^M_{,n} \left(X^M_n \right)^C_{,q} \varepsilon^{aux}_{ij} \delta_{1i} \right) q_{,h} \left(X^R_h \right)^M_{,n} \left(X^M_n \right)^C_{,i} \bar{J}_A dA_R + \\
&-\int_{A_R} \left(\rho \Xi_i \dot{u}^M_i \dot{u}^{aux}_j \right) q_{,h} \left(X^R_h \right)^M_{,n} \left(X^M_n \right)^C_{,i} \bar{J}_A dA_R + \\
&+\int_{A_R} \left[\rho \left(\Xi_i \ddot{u}^M_i u^{aux}_{j,1} + \ddot{u}^{aux}_j u^R_{j,h} \left(X^R_h \right)^M_{,n} \left(X^M_n \right)^C_{,1} \right) \right] q \left[\Xi_i \left(\Psi_i \left(X^R_i \right) \right) \right] \bar{J}_A dA_R + \\
&-\int_{A_R} \left[\rho \left(\left(\dot{u}^R_i - u^R_{i,n} \left(X^R_h \right)^M_{,n} \dot{X}^M_i \right)^R_{,h} \left(X^R_h \right)^M_{,n} \left(X^M_n \right)^C_{,1} \dot{u}^{aux}_j \right) \right] q \left[\Xi_i \left(\Psi_i \left(X^R_i \right) \right) \right] \bar{J}_A dA_R + \\
&-\int_{A_R} \left[\rho \dot{u}^{aux}_{j,1} \Xi_i \left(\dot{u}^M_i \right) \right] q \left[\Xi_i \left(\Psi_i \left(X^R_i \right) \right) \right] \bar{J}_A dA_R
\end{aligned} \tag{4.20}$$

where, A_R is the domain area in the moving system, $\bar{J}_A$ is the Jacobian of the transformation, and Ξ is the mapping function between the referential frame and the crack tip system of coordinates.

According to the relationships between the *J*-integral and DSIFs for two-dimensional crack problems (in the context of LEFM), the following expression is valid for the superimposed state:

$$M = \frac{2}{E'}\left[K_I^{act}K_I^{aux}f_d\left(\dot{a}\right)+K_{II}^{act}K_{II}^{aux}f_s\left(\dot{a}\right)\right] \tag{4.21}$$

where, $E' = E/(1-\nu^2)$ and $E' = E$ for plane strain and plane stress conditions, respectively. Also, $f_d(\dot{a}), f_s(\dot{a})$ represent universal functions, depending on the crack tip velocity $\dot{a}$, expressed as follows:

$$f_i\left(\dot{a}\right)=\frac{1}{\kappa+1}\frac{4\alpha_i\left(1-\alpha_s^2\right)}{4\alpha_d\alpha_s-\left(1-\alpha_s^2\right)^2} \tag{4.22}$$

in which, κ is the Kolosov's constant defined in Section 2.3.1. Besides, in Eq. (4.22) the coefficients α_d and α_s assume the following form:

$$\alpha_d = \sqrt{1-\frac{\dot{a}^2}{c_d^2}} \quad \text{and} \quad \alpha_s = \sqrt{1-\frac{\dot{a}^2}{c_s^2}} \tag{4.23}$$

where, $c_d = \sqrt{(\lambda+2\mu)/\rho}$ and $c_s = \sqrt{\mu/\rho}$ are the longitudinal and transversal wave speed, respectively, depending on the Lame's constant (λ and μ) and the mass density ρ of the material.

The DSIFs of the actual field are computed using two *M*-integral evaluated by combining the actual state with a pure mode I (aux-I) and a pure mode II (aux-II) auxiliary fields, namely $M^{act,aux-I}$ and $M^{act,aux-II}$, which provide the following simplified expression of the actual DSIFs:

$$\begin{aligned} K_I^{act} &= \frac{E'M^{act,aux-I}}{2f_d\left(\dot{a}\right)K_I^{aux-I}} \quad \left(K_{II}^{aux-I}=0\right); \\ K_{II}^{act} &= \frac{E'M^{act,aux-II}}{2f_s\left(\dot{a}\right)K_{II}^{aux-II}} \quad \left(K_I^{aux-II}=0\right) \end{aligned} \tag{4.24}$$

4.1.3.1 Rice's solutions

The Rice's analytical solutions in terms of displacements are the following:

$$\begin{cases} u_1^{aux} = \dfrac{K_I^{aux}}{\sqrt{2\pi}} \dfrac{2\left(1+\alpha_s^2\right)}{\mu D\left(\dot{a}\right)} \left[\sqrt{r_d}\cos\left(\dfrac{\theta_d}{2}\right) - \dfrac{2\alpha_d\alpha_s}{\left(1+\alpha_s^2\right)}\sqrt{r_s}\cos\left(\dfrac{\theta_s}{2}\right) \right] \\ u_2^{aux} = \dfrac{K_I^{aux}}{\sqrt{2\pi}} \dfrac{2\left(1+\alpha_s^2\right)}{\mu D\left(\dot{a}\right)} \left[-\alpha_d\sqrt{r_d}\sin\left(\dfrac{\theta_d}{2}\right) + \dfrac{2\alpha_d}{\left(1+\alpha_s^2\right)}\sqrt{r_s}\sin\left(\dfrac{\theta_s}{2}\right) \right] \end{cases} \tag{4.25}$$

$$\begin{cases} u_1^{aux} = \dfrac{K_{II}^{aux}}{\sqrt{2\pi}} \dfrac{2\alpha_s}{\mu D\left(\dot{a}\right)} \left[2\sqrt{r_d}\sin\left(\dfrac{\theta_d}{2}\right) - \left(1+\alpha_s^2\right)\sqrt{r_s}\sin\left(\dfrac{\theta_s}{2}\right) \right] \\ u_2^{aux} = \dfrac{K_{II}^{aux}}{\sqrt{2\pi}} \dfrac{2\alpha_s}{\mu D\left(\dot{a}\right)} \left[2\alpha_d\sqrt{r_d}\cos\left(\dfrac{\theta_d}{2}\right) - \dfrac{\left(1+\alpha_s^2\right)}{\alpha_s}\sqrt{r_s}\cos\left(\dfrac{\theta_s}{2}\right) \right] \end{cases} \tag{4.26}$$

Instead, the velocity fields are defined as follows:

$$\begin{cases} \dot{u}_1^{aux} = -\dot{a}\dfrac{K_I^{aux}}{\sqrt{2\pi}} \dfrac{\left(1+\alpha_s^2\right)}{\mu D\left(\dot{a}\right)} \left[\dfrac{1}{\sqrt{r_d}}\cos\left(\dfrac{\theta_d}{2}\right) - \dfrac{2\alpha_d\alpha_s}{\left(1+\alpha_s^2\right)}\dfrac{1}{\sqrt{r_s}}\cos\left(\dfrac{\theta_s}{2}\right) \right] \\ \dot{u}_2^{aux} = -\dot{a}\dfrac{K_I^{aux}}{\sqrt{2\pi}} \dfrac{\left(1+\alpha_s^2\right)}{\mu D\left(\dot{a}\right)} \left[\dfrac{\alpha_d}{\sqrt{r_d}}\sin\left(\dfrac{\theta_d}{2}\right) - \dfrac{2\alpha_d}{\left(1+\alpha_s^2\right)}\dfrac{1}{\sqrt{r_s}}\sin\left(\dfrac{\theta_s}{2}\right) \right] \end{cases} \tag{4.27}$$

$$\begin{cases} \dot{u}_1^{aux} = -\dot{a}\dfrac{K_{II}^{aux}}{\sqrt{2\pi}}\dfrac{\left(1+\alpha_s^2\right)}{\mu D(\dot{a})}\left[-\dfrac{2\alpha_s}{\left(1+\alpha_s^2\right)\sqrt{r_d}}\sin\left(\dfrac{\theta_d}{2}\right)+\dfrac{1}{\sqrt{r_s}}\sin\left(\dfrac{\theta_s}{2}\right)\right] \\ \dot{u}_2^{aux} = -\dot{a}\dfrac{K_{II}^{aux}}{\sqrt{2\pi}}\dfrac{\left(1+\alpha_s^2\right)}{\mu D(\dot{a})}\left[\dfrac{2\alpha_d\alpha_s}{\left(1+\alpha_s^2\right)\sqrt{r_d}}\cos\left(\dfrac{\theta_d}{2}\right)-\dfrac{1}{\sqrt{r_s}}\cos\left(\dfrac{\theta_s}{2}\right)\right] \end{cases} \tag{4.28}$$

Finally, the stress fields assume the following form:

$$\begin{cases} \sigma_{11}^{aux} = \dfrac{K_I^{aux}}{\sqrt{2\pi}}\dfrac{1+\alpha_s^2}{D(\dot{a})}\left[\dfrac{1+2\alpha_d^2-\alpha_s^2}{\sqrt{r_d}}\cos\left(\dfrac{\theta_d}{2}\right)-\dfrac{4\alpha_d\alpha_s}{\left(1+\alpha_s^2\right)\sqrt{r_s}}\cos\left(\dfrac{\theta_s}{2}\right)\right] \\ \sigma_{12}^{aux} = \dfrac{K_I^{aux}}{\sqrt{2\pi}}\dfrac{2\alpha_d\left(1+\alpha_s^2\right)}{D(\dot{a})}\left[\dfrac{1}{\sqrt{r_d}}\sin\left(\dfrac{\theta_d}{2}\right)-\dfrac{1}{\sqrt{r_s}}\sin\left(\dfrac{\theta_s}{2}\right)\right] \\ \sigma_{22}^{aux} = \dfrac{K_I^{aux}}{\sqrt{2\pi}}\dfrac{1+\alpha_s^2}{D(\dot{a})}\left[-\dfrac{1+\alpha_s^2}{\sqrt{r_d}}\cos\left(\dfrac{\theta_d}{2}\right)+\dfrac{4\alpha_d\alpha_s}{\left(1+\alpha_s^2\right)\sqrt{r_s}}\cos\left(\dfrac{\theta_s}{2}\right)\right] \end{cases} \tag{4.29}$$

$$\begin{cases} \sigma_{11}^{aux} = \dfrac{K_{II}^{aux}}{\sqrt{2\pi}}\dfrac{2\alpha_s}{D(\dot{a})}\left[\dfrac{\alpha_s\left(\alpha_s^2-1-2\alpha_d^2\right)}{\sqrt{r_d}}\sin\left(\dfrac{\theta_d}{2}\right)+\dfrac{\left(1+\alpha_s^2\right)}{\sqrt{r_s}}\sin\left(\dfrac{\theta_s}{2}\right)\right] \\ \sigma_{12}^{aux} = \dfrac{K_{II}^{aux}}{\sqrt{2\pi}}\dfrac{2\alpha_2}{D(\dot{a})}\left[\dfrac{2\alpha_d}{\sqrt{r_d}}\cos\left(\dfrac{\theta_d}{2}\right)-\dfrac{\left(1+\alpha_s^2\right)}{2\alpha_s\sqrt{r_s}}\cos\left(\dfrac{\theta_s}{2}\right)\right] \\ \sigma_{22}^{aux} = \dfrac{K_{II}^{aux}}{\sqrt{2\pi}}\dfrac{2\alpha_s}{D(\dot{a})}\left[\dfrac{1+\alpha_s^2}{\sqrt{r_d}}\sin\left(\dfrac{\theta_d}{2}\right)-\dfrac{\left(1+\alpha_s^2\right)}{\sqrt{r_s}}\sin\left(\dfrac{\theta_s}{2}\right)\right] \end{cases} \tag{4.30}$$

Eqs. (4.25), (4.27), (4.29) refer to pure mode-I loading scheme, while Eqs. (4.26), (4.28), and (4.30) to pure mode-II. In Eqs. (4.25)-(4.30) $D(\dot{a}) = 4\alpha_d\alpha_s - \left(1+\alpha_s^2\right)^2$, $\theta_d = \tan^{-1}\left(\alpha_d x_2/x_1\right)$, $\theta_s = \tan^{-1}\left(\alpha_s x_2/x_1\right)$, $r_d = \sqrt{x_1^2+\alpha_d^2 x_2^2}$, and $r_s = \sqrt{x_1^2+\alpha_s^2 x_2^2}$.

4.1.4 Fracture criteria

Quasi-brittle materials fail dynamically due to rapid crack propagation mechanisms that, once triggered, become unstable unless arrested. An accurate numerical representation of such complex phenomena requires proper fracture criteria for identifying crack onset events, crack front velocity and propagation direction, and crack arrest conditions.

The dynamic fracture before crack onsetting differs noticeably from what occurs during the crack propagation stage ((Grégoire et al., 2007)). This last consideration relies on the fact that different material toughness thresholds identify the fracture behavior of the material before and suddenly after crack onsetting. Indeed, a dynamic crack initiation toughness K_{Id} identifies the limit threshold for crack onset conditions. Instead, dynamic crack growth K_{ID} and arrest K_{IA} toughness values are associated with crack propagation and crack arrest events. Note that, as denoted by many experimental tests performed on quasi-brittle materials ((Freund, 1990), (Anderson and Anderson, 2005)), K_{ID} varies with crack tip velocity. For these reasons, the crack initiation event must be analyzed separately from the crack propagation and arrest phenomena. To this end, the present method introduces two distinct fracture functions to identify (*i*) crack initiation conditions and (*ii*) investigate crack propagation mechanisms.

The first fracture function f_F^I is defined as follows:

$$f_F^I = \frac{K^*}{K_{Id}} - 1 \;\Rightarrow \begin{cases} f_F^I < 0 & \text{(no initiation)} \\ f_F^I = 0 & \text{(initiation)} \end{cases} \qquad (4.31)$$

In Eq. (4.31), K^* is an Equivalent Stress Intensity Factor.

In the proposed method, it is evaluated through the maximum hoop stress criterion (Erdogan and Sih, 1963) which provides the following expression:

$$K^*\left(K_I, K_{II}, \theta_c\right) = K_I \cos^3\left(\frac{\theta_c}{2}\right) - 3K_{II}\cos^2\left(\frac{\theta_c}{2}\right)\sin\left(\frac{\theta_c}{2}\right) \tag{4.32}$$

where, θ_c is the crack propagation angle calculated trough Eq. (2.49).

The second fracture function f_F^P serves to describe the kinematic of crack tip motion, thus quantifying the velocity of the crack tip and defining the conditions for crack arrest:

$$f_F^P = \frac{K^*}{K_{ID}} - 1 \Rightarrow \begin{cases} f_F^P = 0 \ \ \& \ \ \dot{a} > 0 & \text{(propagation)} \\ f_F^P = 0 \ \ \& \ \ \dot{a} = 0 & \text{(arrest)} \end{cases} \tag{4.33}$$

As discussed previously, K_{ID} depends on the crack tip velocity. To this end, the proposed approach adopts the empirical equation presented by Kanninen and Popelar (Baton, 1986), defined as follows:

$$K_{ID}\left(\dot{a}\right) = \frac{K_{IA}}{1 - \left(\dfrac{\dot{a}}{V_L}\right)^m} \tag{4.34}$$

where, V_L is the limiting crack velocity material, K_{IA} is the crack arrest toughness, and m is a dimensionless shape factor.

Figure 4.3 depicts Eq. (4.34) for different values of the m factor. It shows that K_{ID} assumes a constant value slightly higher than K_{IA} for moderate crack tip velocities, while it increases exponentially for high crack speed rates, reaching an infinite value when the crack tip velocity approaches to V_L. Furthermore, when $\dot{a} = 0$, it results $K_{ID}(\dot{a} = 0) = K_{IA}$

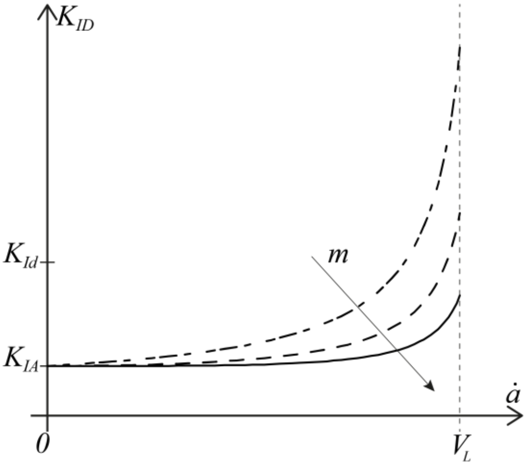

Figure 4.3. Dynamic fracture toughness: a schematic of the empirical equation presented by Kanninen and Popelar (Eq. (4.34)).

and crack arrest occurs. Finally, the plot of K_{ID} shows that K_{Id} is higher than K_{IA}. This last observation denotes that the energy to trigger the crack propagation is generally higher than that needed for maintaining the propagation. Such an aspect further justifies the necessity of two distinct fracture functions for analyzing crack initiation and crack propagation fracture phenomena.

4.2 Implementation aspects

Section 2.4 explains in detail all implementation aspects concerning the FE framework. The current section only reports the changes made to extend the model in a dynamic fracture context.

Regarding the Galerkin approximation, the Eq (2.48) becomes:

$$\begin{aligned} \mathbf{M}\ddot{\mathbf{U}} + \mathbf{K}\mathbf{U} &= \mathbf{F} \\ \mathbf{A}\mathbf{X}^{\mathbf{M}} + \mathbf{R}\boldsymbol{\Lambda} &= \mathbf{0} \end{aligned} \tag{4.35}$$

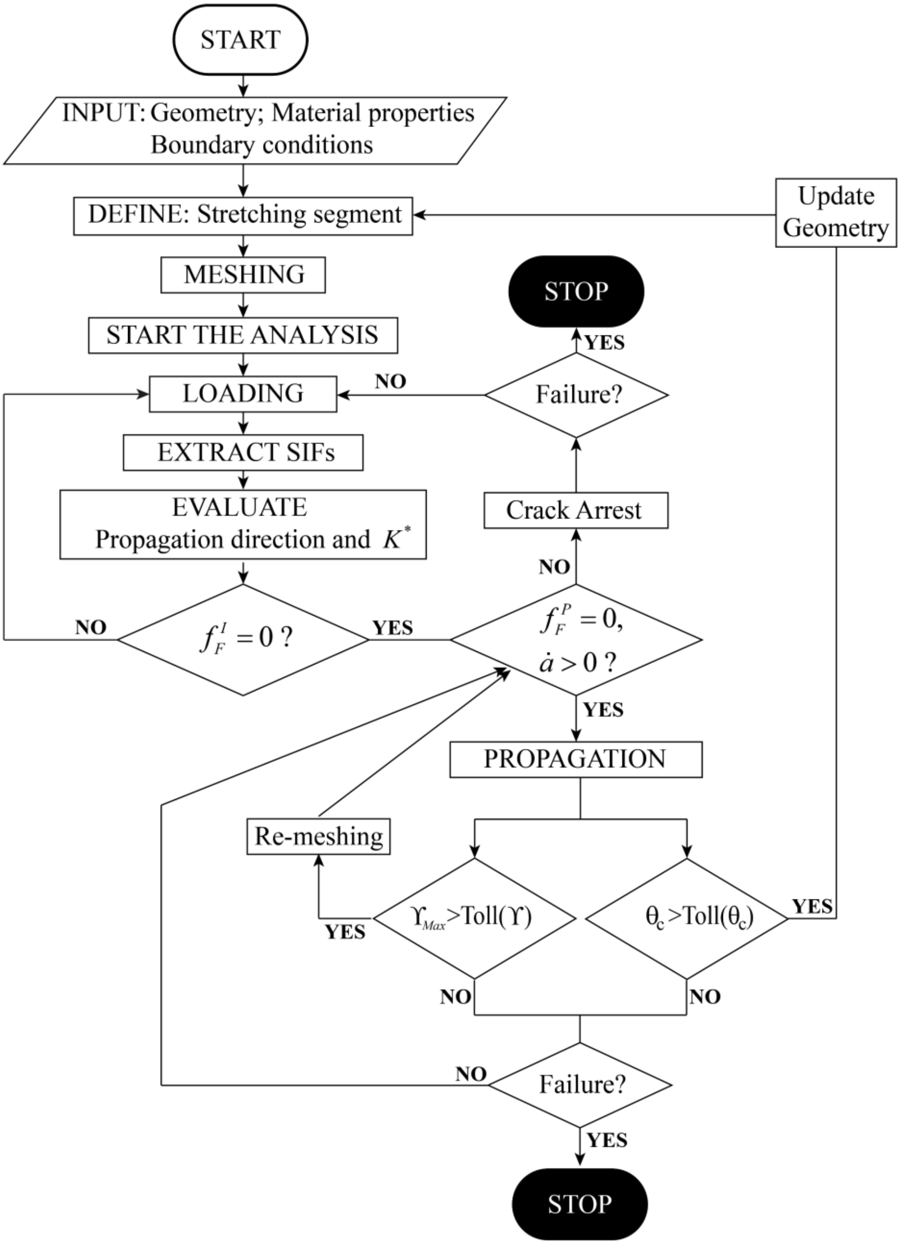

Figure 4.4. Flowchart of the dynamic propagation process.

where, in the first relation, $\mathbf{M}$ represents the consistent mass matrix.

Figure 4.4 reports a flowchart illustrating the steps employed by the proposed strategy for reproducing dynamic fracture mechanisms.

The steps of the numerical procedure are the same as those described in Section 2.4.2. The substantial difference lies in the fact that, for each time step, the model extracts the DSIFs through the ALE formulation of the dynamic *M*-integral. Then, the procedure computes a preliminary value for the kinking angle, and finally checks crack initiation conditions using the fracture function f_F^I. When f_F^I=0, the dynamic propagation takes place, and the second fracture function f_F^P (introduced by Eq. (4.33)) entirely governs the fracture process. At this point, the mesh node of the crack tip advances at a velocity $\dot{a}$ along the direction defined by the instantaneous value of the propagation angle.

4.3 Numerical results

This section reports numerical results to assess the reliability and accuracy of the proposed approach in simulating dynamic crack propagation mechanisms occurring in quasi-brittle materials. In particular, the following cases are investigated:

- A rectangular plate with a horizontal notch under tension.
- An Araldite-B rectangular double cantilever beam.
- The Kalthoff-Winkler impact test.

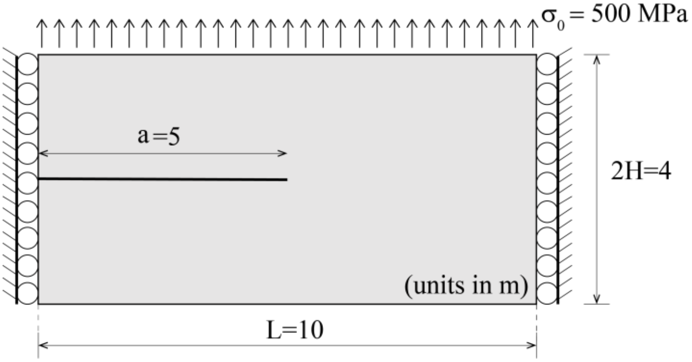

Figure 4.5. A rectangular plate with a horizontal notch under tension: a schematic of geometry and boundary conditions.

These examples are well known for being among the most popular benchmark tests for checking the effectiveness of numerical methodologies devoted to reproducing dynamic crack propagation processes inside material solids.

All these examples are analyzed numerically using the same discretization strategy, involving either plane stress or plain strain 9-node triangular elements arranged according to a Delaunay-type triangulation scheme. The behavior of the material is assumed to be linear and elastic up to the failure. All the numerical simulations were performed with a standard PC equipped with an Intel Core i7-9750H running at 2.60 GHz with 16 GB RAM.

4.3.1 A rectangular plate with a horizontal notch under tension

This case is utilized to validate the ALE formulation of the dynamic *M*-integral. It consists of an infinite plate with a semi-infinite mode-I crack whose analytical solutions, in terms of time evolution of dynamic

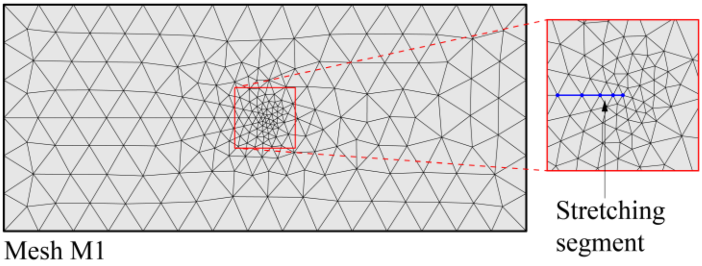

Figure 4.6. A rectangular plate with a horizontal notch under tension: computational mesh employed in numerical simulations.

mode-I DSIF relative to the case of stationary and moving crack front, are available in the literature (Freund, 1990).

Figure 4.5 shows a schematic of a rectangular plate having length L=10 m, height 2H=4 m, and thickness B=1 m, with a horizontal pre-crack a=5 m that develops along the mid-height from the left boundary. The plate presents line constraints on the vertical boundaries that limit horizontal displacements and a uniform and distributed traction σ_0=500 MPa acts on the upper boundary. The Young's Modulus (E), Poisson's ratio (ν), mass density (ρ), dilatational (c_d), and Rayleigh (c_r) wave speeds are equal to E=210 GPa, ν=0.3, ρ=8000 kg/m^3, c_d=5944.5 m/s, and c_r=2942.8 m/s, respectively. Figure 4.6 reports the computational mesh used in numerical simulations, which involves 238 computational nodes and 432 plane strain triangular elements densely arranged around the crack tip region and relatively coarse elsewhere. The stretching segment is discretized by four elements of variable length.

The analytical solutions proposed by Freund (Freund, 1990) provide reasonable values of mode-I DSIF until the stress waves generated by the traction σ_0 acting on the upper boundary of the plate and reflected by the remaining ones reach the crack front ((Belytschko et al., 2003), (Chen et al., 2019)). For this reason, the time interval of validity of such analytical solutions has been estimated to be $0 < t < t_c$, where $t_c = H/c_d$ (H is the half-height of the plate). The Author has developed two sets of analytical solutions: the first set (Case 1) provides the time evolution of the mode-I DSIF for a stationary crack, while the second set (Case 2) deals with a moving crack running at constant velocity. To this end, the mode-I DSIF (K_I) can be evaluated through the following expressions:

$$\begin{aligned} \mathrm{K_I}(0,\mathrm{t}) &= \frac{2\sigma_0}{1-\nu}\sqrt{\frac{\mathrm{c_d}(\mathrm{t}-\mathrm{t_c})(1-2\nu)}{\pi}} && \text{(Case 1)} \\ \mathrm{K_I}(\dot{\mathrm{a}},\mathrm{t}) &= \frac{2\sigma_0}{1-\nu}\sqrt{\frac{\mathrm{c_d}(\mathrm{t}-\mathrm{t_c})(1-2\nu)}{\pi}}\,\frac{1-\dot{\mathrm{a}}/\mathrm{c_r}}{1-\dot{\mathrm{a}}/(2\mathrm{c_r})} && \text{(Case 2)} \end{aligned} \tag{4.36}$$

According to these analytical solutions, K_I is zero until the stress waves reach the crack tip (for $t < t_c$). Besides Eq. (4.36), several works have analyzed the fracture behavior of the plate through advanced numerical strategies. Among these, Chen et al. (Chen et al., 2019) have reproduced the crack propagation of the plate using the Singular Edge-based Smoothed Finite Element Method (SE-FEM). Menouillard et al. (Menouillard et al., 2010) have adopted an XFEM approach enhanced by the crack tip enrichment method. Such numerical methodologies extract K_I using the *M*-integral method, thus representing relevant references for assessing the accuracy of the proposed approach.

In addition to Case 1 and Case 2, the present work has examined a combined case (Case 3) consisting of an initially stationary crack that starts moving at constant velocity $\dot{a}$=1500 m/s for $t > t_c$. Of course, both Case 2 and Case 3 represent significant test for checking the ALE formulation of the dynamic *M*-integral developed in this thesis.

Note that some simplifications had to be made to the script code to simulate Cases 2 and 3 using the present procedure (see Figure 4.4). Conditions dictated by fracture functions f_F^I and f_F^P have been substituted by switch statements, which simply impose that the crack tip starts moving at a constant velocity $\dot{a}$=1500 m/s for $t > t^*$ ($t^* = 0$ for Case 2 and $t^* = 1.5t_c$ for Case 3). In addition, crack arrest events are excluded.

In the following analysis, the finite element distortion tolerance is set equal to $\text{Toll.}(\gamma)$=1 and the *M*-integral method assumes auxiliary fields from Rice's analytical solutions.

Figure 4.7 compares the normalized K_I (expressed as $K_I / \sigma_0 \sqrt{H}$) as a function of normalized time (t/t_c) predicted through the proposed approach with the analytical solutions developed by Freund (Freund, 1990) and numerical results gained by Chen et al. (Chen et al., 2019) and Menouillard et al. (Menouillard et al., 2010). In particular, Figure 4.7-a, b, and c report the results for Cases 1, 2, and 3, respectively. The results denote that the proposed strategy is in good agreement with both analytical solutions and predictions provided by other numerical techniques. In addition, similar to the predictions of the other Authors, the value of K_I computed through the present method is zero until t/t_c =0.6. After that, it oscillates around zero for $0.6 \le t/t_c \le 1$, and finally, it follows the analytic curves for $t/t_c > 1$.

A possible explanation for this oscillating behavior of K_I in the range $0.6 \le t/t_c \le 1$ is that the stress wave induced into the plate by the external loads interacts with the domain area defined for *M*-integral

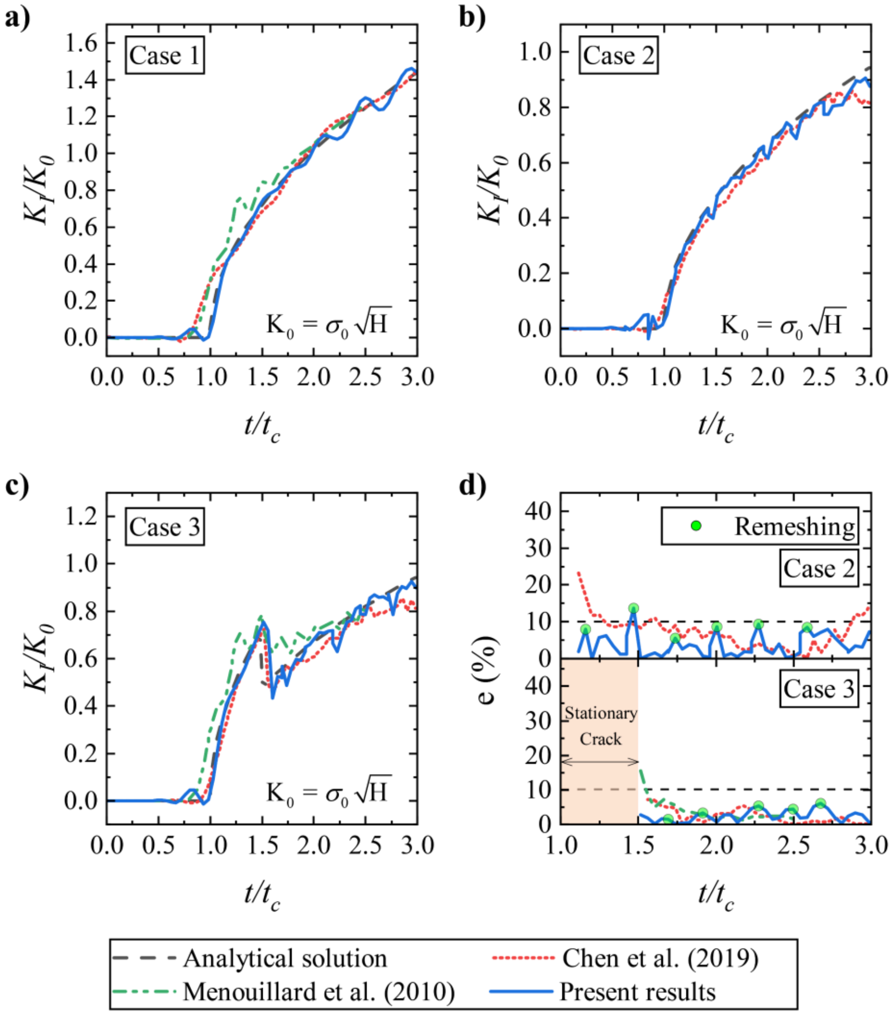

Figure 4.7. A rectangular plate with a horizontal notch under tension: A comparison in terms of normalized K_I vs normalized time between the proposed method, the analytical solutions developed by Freund (Freund, 1990), and numerical predictions obtained by Chen et al. (Chen et al., 2019) and Menouillard et al. (Menouillard et al., 2010) for (a) Case 1, (b) Case 2, (c) Case 3. (d) Percentage error between the numerical predictions and analytical solutions for Cases 2 and 3.

computation. Note that such an aspect does not significantly affect the reliability of the numerical solution because variations of K_I are almost imperceptible and occur for a short time.

Figure 4.7-d shows the percentage error between the numerical predictions and the analytical solutions for Cases 2 and 3, defined as:

$$\mathrm{e}(\%) = \frac{\left| K_{\mathrm{I}}^{\mathrm{analyt.}} - K_{\mathrm{I}}^{\mathrm{num.}} \right|}{K_{\mathrm{I}}^{\mathrm{analyt.}}} \tag{4.37}$$

As one can see, the proposed method evaluates K_I somewhat correctly during the mesh motion since the percentage variations are less than 10% in both cases and comparable with the predictions of Chen et al. (Chen et al., 2019) and Menouillard et al. (Menouillard et al., 2010).

These results confirm the effectiveness of the proposed procedure based on the use of the ALE formulation of the *M*-integral.

The curves of the relative errors obtained through the proposed approach have fluctuations with peaks of divergence from the analytical solution. The peaks probably take place when the triangular finite elements of the computational mesh have undergone relevant distortions. Indeed, any time there is a divergence peak, the numerical model updates the computational mesh via a remeshing action (identified on the curve by the green points), which restore mesh regularity, and numerical accuracy improves accordingly. These results denote that the precision of the current strategy can be particularly dependent on the computational mesh arrangement and the finite element distortion tolerance adopted to run numerical simulations.

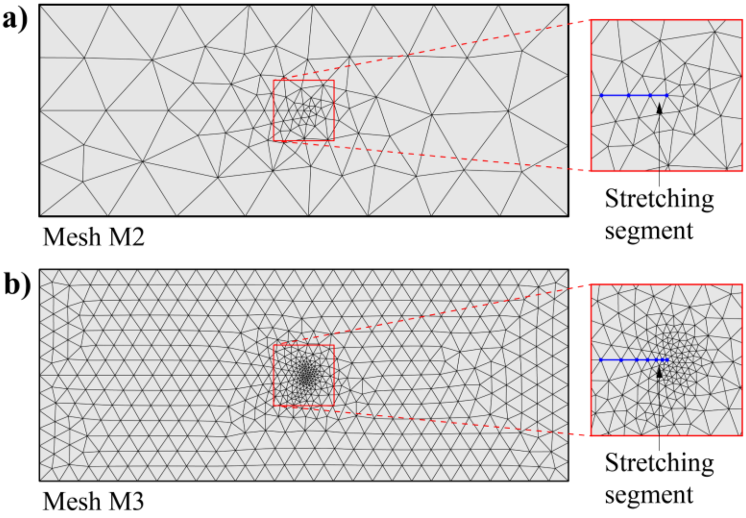

Figure 4.8. A rectangular plate with a horizontal notch under tension: representation of (a) Mesh M2 and (b) Mesh M3.

4.3.1.1 Parametric analyses

To examine the previously exposed aspects, two additional parametric analyses are developed regarding Case 2.

The first parametric study aims to investigate the influence of mesh discretization on the accuracy of the proposed model. To this end, further numerical simulations are carried out using the computational meshes illustrated in Figure 4.8, identified in the sequel as Mesh M2 (Figure 4.8-a) and Mesh M3 (Figure 4.8-b) and compared with the mesh configuration reported in Figure 4.6 (named Mesh M1).

Mesh M2 is the coarsest of the set, involving 100 computational nodes and 175 triangular elements. Mesh M3 is the most refined since it has 596 computational nodes and 1113 triangular elements. The stretching segments present three and six elements for the Meshes M2

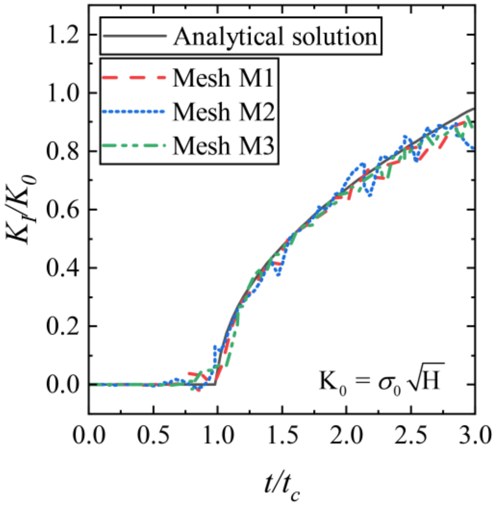

Figure 4.9. A rectangular plate with a horizontal notch under tension: influence of mesh discretization.

and M3, respectively. Table 4.1 reports statistics about the examined meshes. Figure 4.9 compares the normalized K_I (expressed as $K_I/\sigma_0\sqrt{H}$) as a function of normalized time (t/t_c) obtained using the

Table 4.1 – A rectangular plate with a horizontal notch under tension: details of the meshes used in the parametric analysis.

Type	Triangular Elements				Stretching segment		
	DOFs	Number	Maximum size (mm)	Minimum size (mm)	Number of elements	Maximum size (mm)	Minimum size (mm)
M1	238	432	758.00	74.87	4	186.70	74.56
M2	100	175	1451.95	124.10	3	211.86	125.26
M3	596	1113	417.63	37.30	6	153.45	35.48

Table 4.2 – A rectangular plate with a horizontal notch under tension: Computational Time and number of Remeshing Events between the mesh configurations for Case 2.

Mesh	Computational Time (s)	Number of Remeshing Events
M1	53	11
M2	41	8
M3	98	16

considered mesh configurations depicted in Figure 4.6 and Figure 4.8, and the analytical solutions. The results highlight that the present procedure ensures acceptable levels of accuracy in extracting K_I during the crack propagation regardless of the mesh discretization. In addition, it is worth noting that the employed meshes involve a variable amount of total remeshing events and different computational times to perform the entire simulation. Examining the results reported in Table 4.2, it transpires that Mesh M2 is the most useful for a preliminary evaluation of the problem, while Mesh M3 is the most computationally expensive. For this reason, Mesh M1 represents an optimal compromise between computational efficiency and numerical accuracy.

The second parametric analysis examines the influence of the pre-established tolerance of finite element distortion (i.e., $\mathrm{Toll.}(\gamma)$). Figure 4.10 depicts the variability of the normalized K_I as a function of normalized time for values of $\mathrm{Toll.}(\gamma)$ equal to 0.5, 1, 2, and 3. The results denote that (*i*) $\mathrm{Toll.}(\gamma)$ influences the reliability of the numerical solution and (*ii*) accurate numerical predictions are ensured by fixing $\mathrm{Toll.}(\gamma)$ no more than 2. For $\mathrm{Toll.}(\gamma)>2$, there is a notable difference

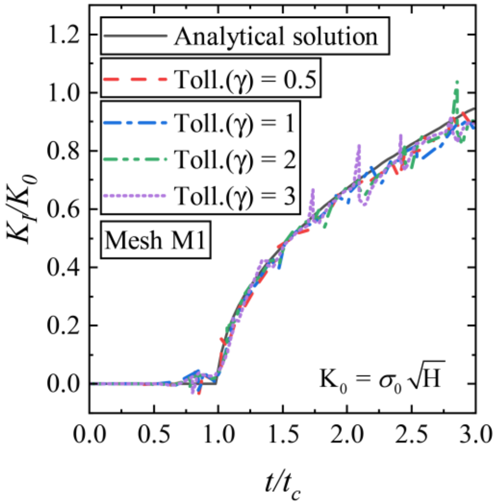

Figure 4.10. A rectangular plate with a horizontal notch under tension: influence of finite element distortion tolerance Toll.(γ).

Table 4.3 – A rectangular plate with a horizontal notch under tension: Computational Time and number of Remeshing Events for different values of the finite element distortion tolerance for Case 2.

Toll.(γ)	Computational Time (s)	Number of Remeshing Events
0.5	72	16
1	53	11
2	45	9
3	63	9

between the analytical and numerical results with relevant peaks of divergence in the latter. This is likely to happen because of the occurrence of significant distortions in the finite elements of the computational mesh. In particular, these peaks mark the onset of remeshing events.

Indeed, the accuracy of the numerical solution improves once a remeshing action occurs.

Table 4.3 reports statistics regarding the computational time and the number of remeshing events, which decrease with increasing $\text{Toll.}(\gamma)$. This trend is quite evident by comparing the results gained for $\text{Toll.}(\gamma)$ =0.5, $\text{Toll.}(\gamma)$=1, and $\text{Toll.}(\gamma)$=2. Consequently, a suitable value of this parameter can be selected in the range $1 < \text{Toll.}(\gamma) < 2$, which ensures a good level of accuracy in dynamic K_I evaluation while avoiding excessive computational efforts. The advantage of using the range $1 < \text{Toll.}(\gamma) < 2$ is also confirmed by observing the computational time and the number of remeshing events that occurred for $\text{Toll.}(\gamma)$=3. Indeed, this threshold value spends a computational time higher than the others because of some convergence problems in the numerical solver. Probably, this latter needed more iterative steps to find numerical convergence due to the excessive distortions undergone by the finite elements inside the computational mesh, which are also marked by the peaks of divergence from the analytical solution.

4.3.2 An Araldite-B rectangular double cantilever beam

The second case provides prominent experimental data that allows us to assess the overall reliability of the proposed method. It reproduces the experimental test developed by Kalthoff et al. (Kalthoff et al., 1977) on a rectangular double cantilever beam made by Araldite-B. The Authors have investigated the mode-I dynamic crack propagation process, evaluating the time histories of the crack length, crack tip velocity and mode-I DSIF.

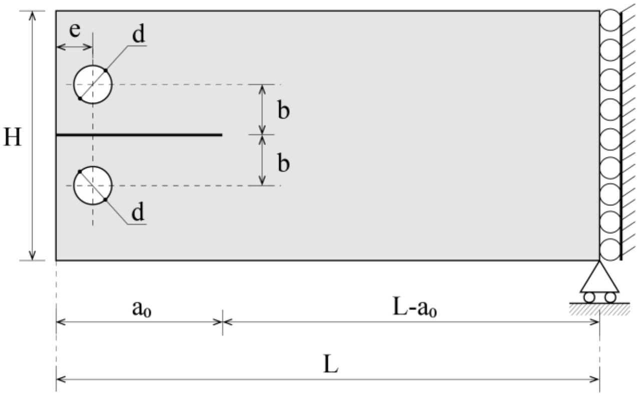

Figure 4.11. An Araldite-B rectangular double cantilever beam: a schematic of geometry and boundaries conditions.

Figure 4.11 shows the double cantilever beam having the following dimension: length L=321 mm, height H=63.5 mm, and thickness B=10 mm. The beam presents a horizontal pre-crack a_0 of length equal to 83.8 mm and two circular holes of diameter d=25 mm, placed symmetrically with respect to the crack plane. The holes are e=16 mm and b=20 mm from the left boundary and the crack plane, respectively. They serve as allocation for the mechanical gauges of an experimental machine for conducting Mode-I fracture tests. The experimental machine produces two vertical and opposite forces that dilate the surfaces of the notch. Finally, on the right boundary, line constraints limit the horizontal displacement of the beam.

Figure 4.12 reports the computational domain, mesh discretization, and load configuration. As one can see, the geometry of the numerical model does not include the holes. As evidenced by Shahani and Amini Fasakhodi (Shahani and Amini Fasakhodi, 2009). this assumption does not affect the reliability of the numerical results. Besides, it provides

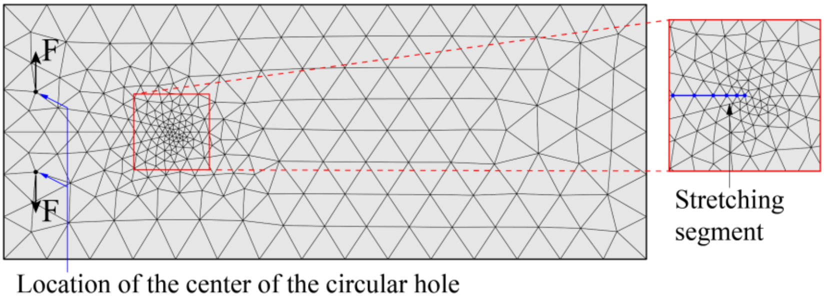

Figure 4.12. An Araldite-B rectangular double cantilever beam: computational mesh used in numerical simulations and load configuration.

Table 4.4 – An Araldite-B rectangular double cantilever beam: mechanical properties.

Young's Module (E)	3660 MN/m^2
Poisson's ratio (ν)	0.39
Density (ρ)	1172 kg/m^3
Dilatational wave speed (c_d)	1919.1 m/s
Shear wave speed (c_s)	1059.9 m/s
Rayleigh wave speed (c_r)	966.28 m/s
Static fracture toughness (K_{IC})	2.32 MPa m$^{1/2}$

the relevant benefit of setting the load configuration simply as two vertical and opposite forces (F) applied at the geometric coordinates of the center of the holes. The mesh comprises 480 plane stress triangular elements refined in the region around the crack tip and relatively coarser elsewhere. The stretching segment has five elements of variable size.

Kalthoff et al. (Kalthoff et al., 1977) also provide the mechanical properties of the beam (Table 4.4) and the experimental curve of the

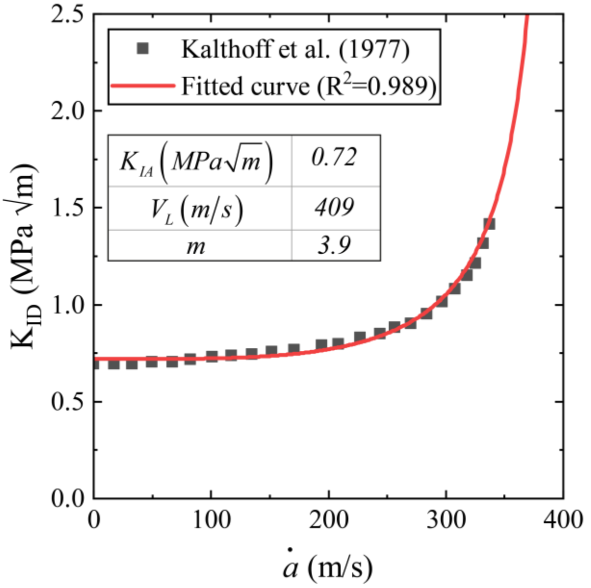

Figure 4.13. An Araldite-B rectangular double cantilever beam: dynamic fracture toughness versus crack tip velocity.

dynamic crack growth toughness (K_{ID}) as a function of crack velocity ($\dot{a}$). In the proposed study, a nonlinear fitting analysis has been performed to replicate the trend line of K_{ID} through Eq. (4.34), thus determining the values of crack arrest toughness (K_{IA}), the limiting crack velocity (V_L), and the dimensionless shape factor (m). In particular, $K_{IA} = 0.72\, MPa\, m^{1/2}$, $V_L = 409\, m/s$, and $m = 3.9$ are obtained, which involve an R-square value of 0.989 in the fitting procedure. Figure 4.13 shows the results of the nonlinear fitting analysis. Note that it was conducted using the Nonlinear Curve Fitting procedure developed by the software Origin Lab (Origin(Pro)).

Beyond this work, several Authors have reproduced the experimental results of Kalthoff et al. (Kalthoff et al., 1977) through advanced numerical strategies. Among these, Ooi et al. (Ooi et al., 2013) have investigated the fracture behavior of the beam using an advanced numerical method based on the Scaled Boundary Finite Element Method (SB-FEM). Shahani and Amini Fasakhodi (Shahani and Amini Fasakhodi, 2009) have employed a traditional FE-based numerical model utilizing a remeshing algorithm to reproduce crack advancement. Koh et al. (Koh et al., 1988) have used a moving-grid finite element method based on the Eulerian-Lagrangian Description (ELD).

The proposed strategy simulated the dynamic crack propagation using a two-step analysis procedure, similar to what Ooi et al. (Ooi et al., 2013) have done. More precisely, the numerical model performs an initial quasi-static analysis, in which the external loads are progressively incremented until crack initiation conditions occur (*i.e.*, $f_F^I = 0$). Next, a second transient-type analysis is performed based on the numerical solution associated with $f_F^I = 0$ keeping the opening load constant while simulating dynamic crack propagation.

Figure 4.14-a compares the time history of the crack extension predicted by the present approach with the experimental results of Kalthoff et al. (Kalthoff et al., 1977) and the numerical predictions of Koh et al. (Koh et al., 1988), and Shahani and Amini Fasakhodi (Shahani and Amini Fasakhodi, 2009). Figure 4.14-b shows the snapshots of the deformed configurations of the beam gained through the present method at the points of the time history curve indicated by Roman numerals in Figure 4.14-a. The proposed strategy agrees reasonably well with both the experimental data and numerical results predicted by the other numerical approaches. To quantify the difference between the prediction

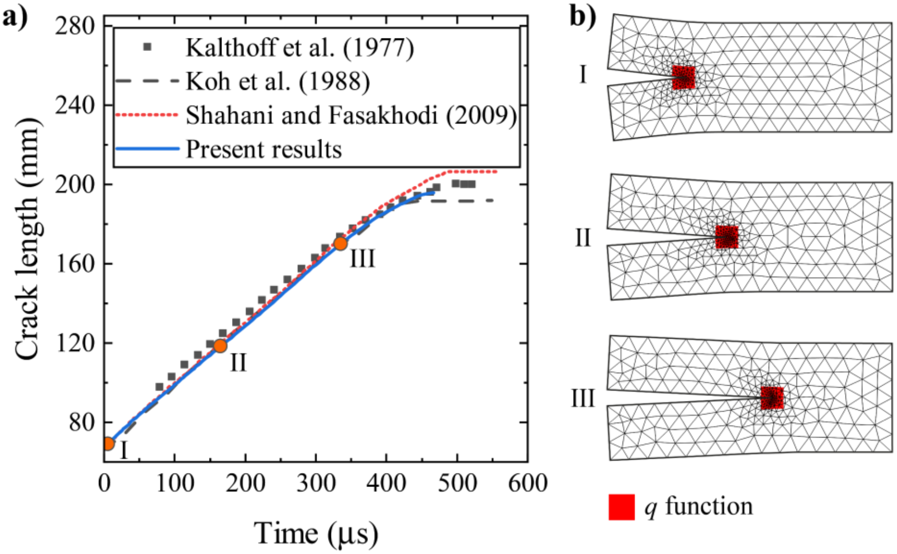

Figure 4.14. An Araldite-B rectangular double cantilever beam: (a) A comparison in terms of time history of the crack extension between the present method, the experimental data achieved by Kalthoff et al. (Kalthoff et al., 1977), and numerical predictions of Koh et al. (Koh et al., 1988) and Shahani and Amini Fasakhodi (Shahani and Amini Fasakhodi, 2009). (b) snapshots of the deformed configurations of the beam predicted by the proposed approach.

of the present method and those reported in the reference works, the following percentage difference at time t is defined as follows:

$$\Delta X(\%) = \frac{\left| X^{\text{REF}} - X^{\text{PRES}} \right|}{X^{\text{REF}}} \tag{4.38}$$

where, X^{REF} and X^{PRES} are the results reported in the reference works and those obtained by the proposed approach at the same time t. With reference to the crack length, it results that ΔX ranges between 0.02%-5.22% referring to the experimental data (Kalthoff et al., 1977), and 0.02%-3.86% and 0.01%-3.84% concerning the results gained by Koh

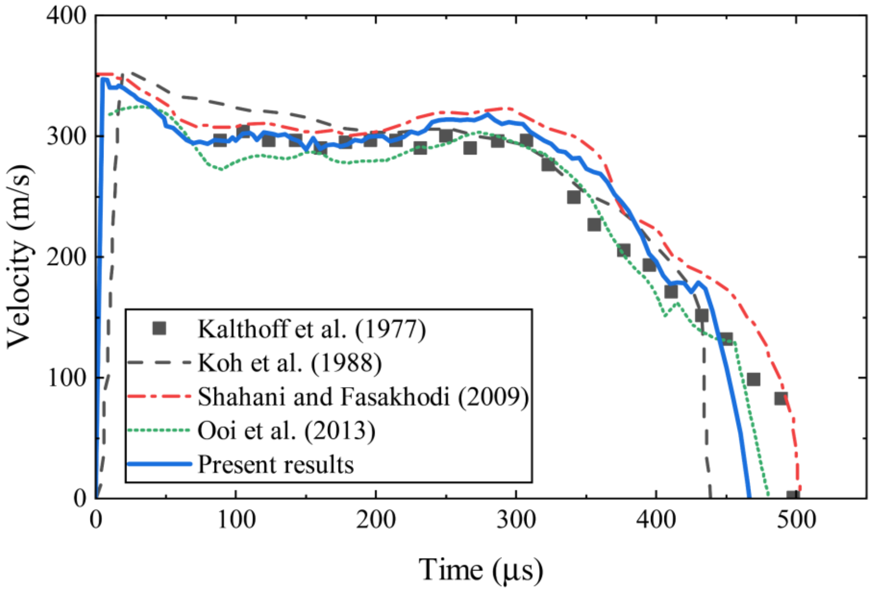

Figure 4.15. An Araldite-B rectangular double cantilever beam: A comparison in terms of time history of the crack tip velocity between the present method, the experimental data achieved by Kalthoff et al. (Kalthoff et al., 1977), and numerical predictions of Koh et al. (Koh et al., 1988), Shahani and Amini Fasakhodi (Shahani and Amini Fasakhodi, 2009), and Ooi et al. (Ooi et al., 2013).

et al. (Koh et al., 1988) and Shahani and Amini Fasakhodi (Shahani and Amini Fasakhodi, 2009), respectively.

Figure 4.15 compares the time history of the crack tip velocity evaluated by the present method with the experimental results of Kalthoff et al. (Kalthoff et al., 1977) and the numerical predictions of Koh et al. (Koh et al., 1988), Shahani and Fasakhodi (Shahani and Amini Fasakhodi, 2009), and Ooi et al. (Ooi et al., 2013). The proposed method predicted a starting crack tip velocity of about 350 m/s, which marginally reduces to almost 300 m/s after 80 μs. Then, the crack tip advances with this velocity until 300 μs, and, finally, for $t > 300$ μs, the crack tip velocity decreases. The proposed approach agrees very well with the numerical results of Shahani and Amini Fasakhodi (Shahani and Amini Fasakhodi, 2009) because ΔX ranges between 0.05%-4.43% in the time interval $80\,\mu s \le t \le 300\,\mu s$. Instead, in the same interval, the range of ΔX slightly rises for the remaining reference data. In particular, ΔX varies between 0.33%-9.81%, 0.02%-8.92%, and 0.87% -8.91% regarding the experimental results (Kalthoff et al., 1977), Koh et al. (Koh et al., 1988), and Ooi et al. (Ooi et al., 2013), respectively. In the time interval from 300 μs to 460 μs, the proposed method agrees very well with the predictions of Shahani and Fasakhodi (Shahani and Amini Fasakhodi, 2009) and Koh et al. (Koh et al., 1988) because the associated ΔX oscillates only between 0.29%-5.15% and 1.54%-9.89%, respectively. Instead, regarding the experimental results (Kalthoff et al., 1977) and numerical predictions of Ooi. et al. (Ooi et al., 2013), ΔX somewhat increases, ranking between 3.05%-18.10% and 4.34%-17.72%, respectively. Despite such increments, ΔX is still acceptable from an engineering point of view, thus confirming the reliability of the proposed approach. Furthermore, as one can see, the proposed method, the experimental data, and the other numerical approaches predict different time instants for crack arrest.

Figure 4.16 compares the time history of the mode-I DSIF (K_I) evaluated through the present method with the experimental one (Kalthoff et al., 1977) and those predicted by Koh et al. (Koh et al., 1988), Shahani and Amini Fasakhodi (Shahani and Amini Fasakhodi, 2009), and Ooi et al. (Ooi et al., 2013). The proposed method agrees with the

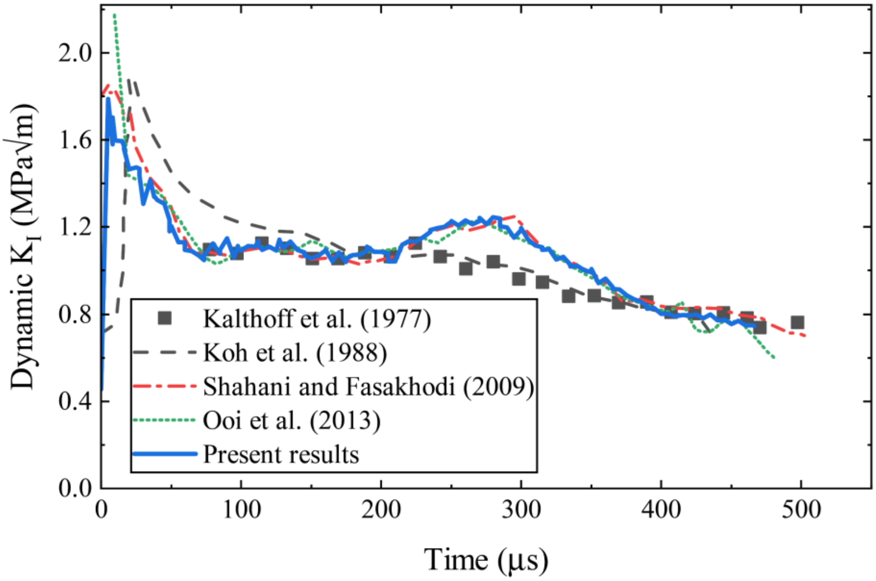

Figure 4.16. An Araldite-B rectangular double cantilever beam: A comparison in terms of time history of the mode-I dynamic stress intensity factor between the present method, the experimental data achieved by Kalthoff et al. (Kalthoff et al., 1977), and numerical predictions of Koh et al. (Koh et al., 1988), Shahani and Amini Fasakhodi (Shahani and Amini Fasakhodi, 2009), and Ooi et al (Ooi et al., 2013).

numerical predictions obtained by Shahani and Amini Fasakhodi (Shahani and Amini Fasakhodi, 2009) and Ooi et al. (Ooi et al., 2013) since that the associated ΔX ranges between 0.06%-6.97% and 0.03%-6.87%, respectively. In contrast, there are some differences between the prediction of the proposed method, the numerical results of Koh et al. (Koh et al., 1988) where ΔX ranges between 0.12% and 21.15%, and the experimental results (Kalthoff et al., 1977), in which ΔX is just over 20%. In particular, for the latter, significant variations occur between 207 μs and 390 μs only.

4.3.2.1 Influence of auxiliary fields

With reference to the rectangular double cantilever beam, this section presents an additional parametric study dedicated to analyzing the influence of auxiliary fields used in the *M*-integral computation. As discussed in Section 4.1.3, there are two possible options as auxiliary fields concerning dynamic fracture problems. The first option consists of adopting analytical solutions for and advancing crack at constant velocity derived by Rice, while the second one includes displacement and stress fields relative to Williams' asymptotic solutions. Most studies reported in the literature have employed Williams' asymptotic solutions, even if they do not account for dynamic effects. Therefore, to identify the best option, the numerical simulation of the beam has been carried out assuming the following three auxiliary fields:

- **Aux. fields 1**: Rice's asymptotic solutions under the non-uniform crack tip velocity hypothesis.
- **Aux. fields 2**: Rice's asymptotic solutions under the hypothesis of uniform crack tip velocity.
- **Aux. fields 3**: Williams' asymptotic solutions.

Figure 4.17 shows the results regarding the time histories of the crack tip velocity (Figure 4.17-a) and mode-I DSIF (Figure 4.17-b). As one can see, the numerical model predicts the same dynamic fracture behavior concerning the crack tip velocity and mode-I DSIF evolution because the results are somewhat comparable. This behavior can be ex-

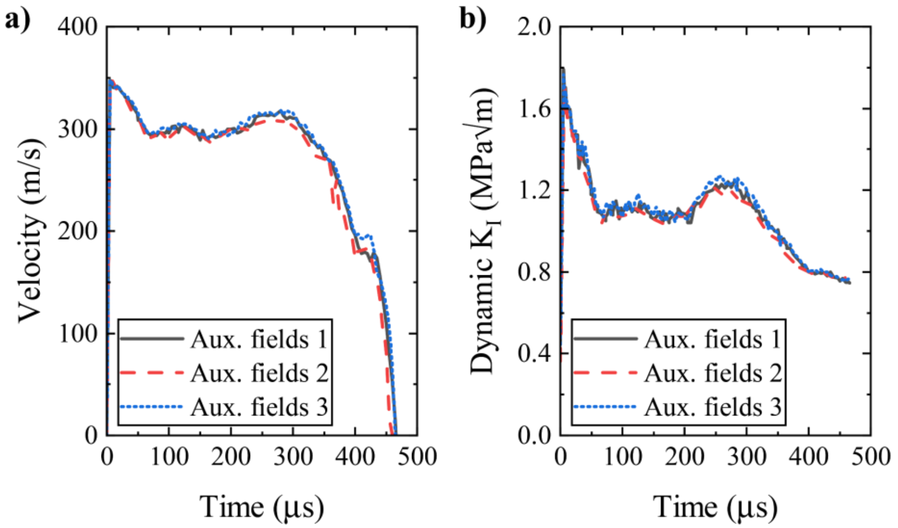

Figure 4.17. An Araldite-B rectangular double cantilever beam: time histories of (a) crack tip velocity and (b) mode-I DSIF for the different auxiliary fields.

plained because the analytical solutions of Rice tend to those of Williams for low crack tip velocities. In addition, both the analytical solutions have a singularity for the stress field, which limits the variation in case of high crack tip rates. Despite the considered auxiliary fields lead to similar results, there are significant differences in numerical implementation. Indeed, employing Williams' asymptotic solutions implicates that the velocity of the auxiliary field is zero, thus simplifying the kinematic description of the auxiliary displacement fields. Besides, the *M*-integral expression notably simplifies (Eq. (4.14) becomes Eq. (4.15)). Finally, it is possible to conclude that the best option for the auxiliary fields in the *M*-integral method can be Williams' asymptotic solutions.

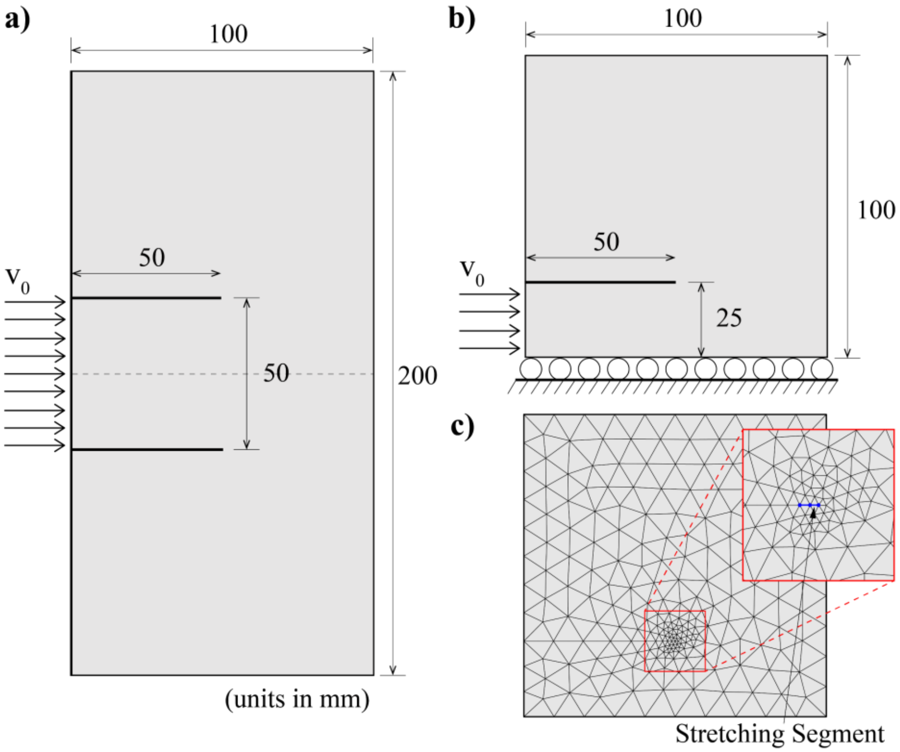

Figure 4.18. The Kalthoff-Winkler impact test: (a) experimental scheme; (b) a schematic of geometry and boundary conditions inputted in the numerical model; (c) initial mesh configuration used in numerical simulation.

4.3.3 The Kalthoff-Winkler impact test

This example represents a prominent test to assess the ability of the proposed method to reproduce dynamic mixed-mode crack propagation phenomena in quasi-brittle materials. It is the well-known experiment performed by Kalthoff and Winkler concerning a rectangular pre-cracked plate with twofold horizontal notches impacted by a projectile at a constant speed (Figure 4.18-a). The impact induces mixed-mode crack propagation mechanisms that develop inside the plate, degrading its integrity. The experiment Authors have reported that the crack paths are symmetric regarding the middle plane of the plate, inclined about $\alpha=70°$ with reference to the horizontal. Because of the symmetry of the specimen's geometry, boundary conditions, and crack trajectories (as emerged from experimental observations), only half of the plate geometry is implemented in the numerical model (Figure 4.18-b).

In the numerical model, the plate has a width L=100 mm and height H=100 mm, with a horizontal notch of length a=50 mm distant of 25 mm from the bottom edge. A constant velocity v_0=16.5 m/s is imposed on the external boundary between the pre-crack and the lower edge to simulate the effect induced by the projectile's impact. The Young's modulus (E), Poisson's ratio (ν), mass density (ρ), and dynamic crack initiation toughness (K_{Id}) are equal to E=190 GPa, ν=0.3, ρ=8000 kg/m^3 and K_{Id} =68 MPa m$^{1/2}$, respectively.

Figure 4.18-c reports the mesh configuration employed to discretize the computational domain. It comprises 427 plane strain triangular elements arranged finely around the crack tip region and coarser elsewhere. As shown in the zoomed view, the stretching segment presents two elements of variable length.

Many researchers have reproduced the experimental test through different numerical strategies. Belytschko and Tabbara (Belytschko and Tabbara, 1996) have used a meshless approach based on the Element-Free Galerkin Method (EFGM). Ooi et al. (Ooi et al., 2013) have employed the Scaled Boundary Finite Element Method (SB-FEM). Yan et al. (Yan et al., 2021) have adopted a Continuous-Discontinuous Cellular Automaton (CDCA) method. Note that, all these Authors assumed

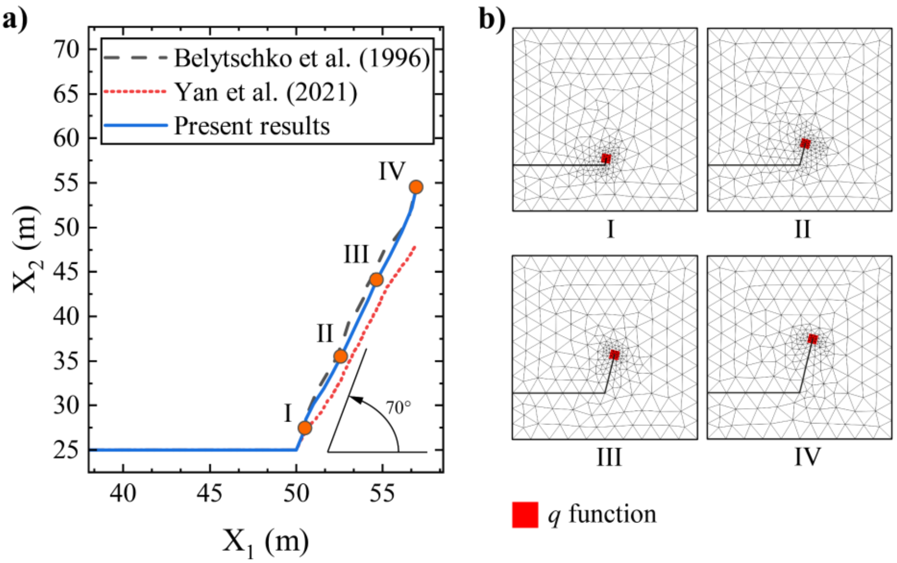

Figure 4.19. The Kalthoff-Winkler impact test: (a) a comparison in terms of crack paths between the present method, experimental evidence, and numerical predictions of Belytschko and Tabbara (Belytschko and Tabbara, 1996), and Yan et al. (Yan et al., 2021); (b) snapshots of the deformed configurations of the plate predicted by the proposed approach.

that the crack propagates at a constant velocity $\dot{a} = 0.15\, c_s$ once the crack onset conditions are satisfied ($c_s = 3100.9$ m/s represents the shear wave speed).

Figure 4.19-a compares the crack paths obtained through the present method with experimental evidence and numerical results achieved by Belytschko and Tabbara (Belytschko and Tabbara, 1996) and Yan et al. (Yan et al., 2021). Figure 4.19-b illustrates the snapshots of the deformed configurations marked by Roman numerals in Figure 4.19-a.

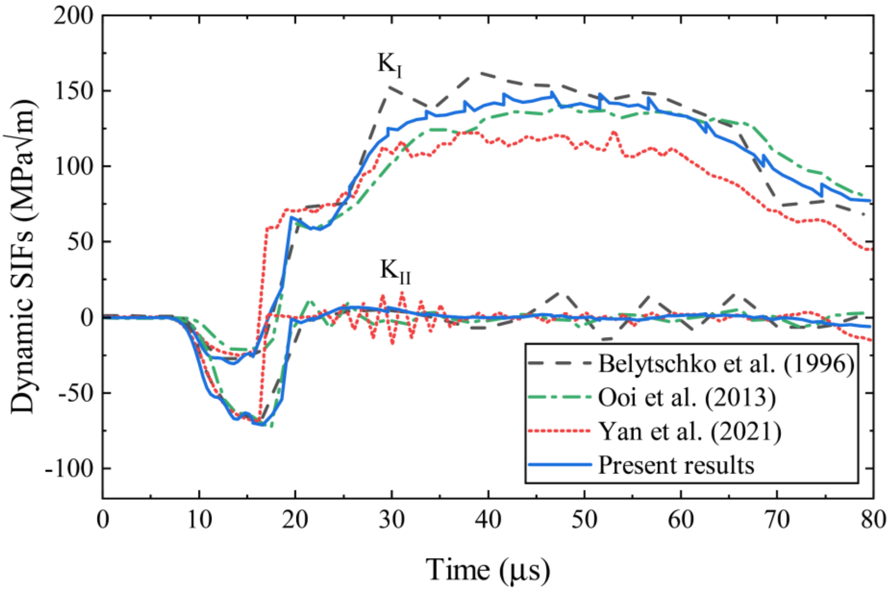

Figure 4.20. The Kalthoff-Winkler impact test: a comparison in terms of the time histories of the DSIFs between the present method and numerical predictions of Belytschko and Tabbara (Belytschko and Tabbara, 1996), Ooi et al. (Ooi et al., 2013), and Yan et al (Yan et al., 2021).

The present method predicts an almost straight crack trajectory at 68° to the horizontal. It is consistent with both experimental and numerical approaches. In addition, the snapshots in Figure 4.19-b confirm that the crack propagation simulated by the proposed strategy implicates that the refined mesh zone around the crack tip region advances simultaneously to the crack front.

Figure 4.20 compares the time histories of DSIFs (K_I, K_{II}) achieved by the proposed model with numerical results obtained by Belytschko and Tabbara (Belytschko and Tabbara, 1996), Ooi et al. (Ooi et al., 2013) and Yan et al. (Yan et al., 2021). Regarding K_{II}, the figure shows that the results of the present approach are in line with the predictions of other numerical approaches. Concerning K_I, one observes that it has two different behaviors. The first occurs between $0 \le t \le 25\,\mu s$ and denotes a notable agreement between the predictions of the proposed approach and those of other numerical strategies. The second develops from $t = 25\,\mu s$ until the end of the analysis. The predictions of the proposed method diverge from those associated with other numerical approaches in this time interval. Indeed, ΔX varies from 1.16% to 23.20% and 0.14%-15.93% for Belytschko and Tabbara (Belytschko and Tabbara, 1996) and Ooi et al. (Ooi et al., 2013), respectively. These differences are slight, thus confirming the reliability and effectiveness of the ALE formulation of the dynamic *M*-integral to extract DSIFs at the crack front under mixed-mode fracture conditions.

4.3.3.1 Non-uniform crack tip velocity

Several works in the literature have analyzed the Kalthoff and Winkler test without fixing the crack front velocity equal to $\dot{a} = 0.15\, c_s$, but assuming it as an unknown variable of the fracture problem to be evaluated. Belytschko et al. (Belytschko et al., 2003) have simulate the fracture behavior of the plate using the XFEM method. Rabczuk et al. (Rabczuk et al., 2010) have reproduced the crack propagation mechanism by adopting the Cracking-Particle Method (CPM), and Lee et al. (Lee et al., 2016) have employed the Particle Difference Method (PDM). All Authors provide comparable results in terms of crack path and crack tip velocity. It was found that crack onset conditions hap-

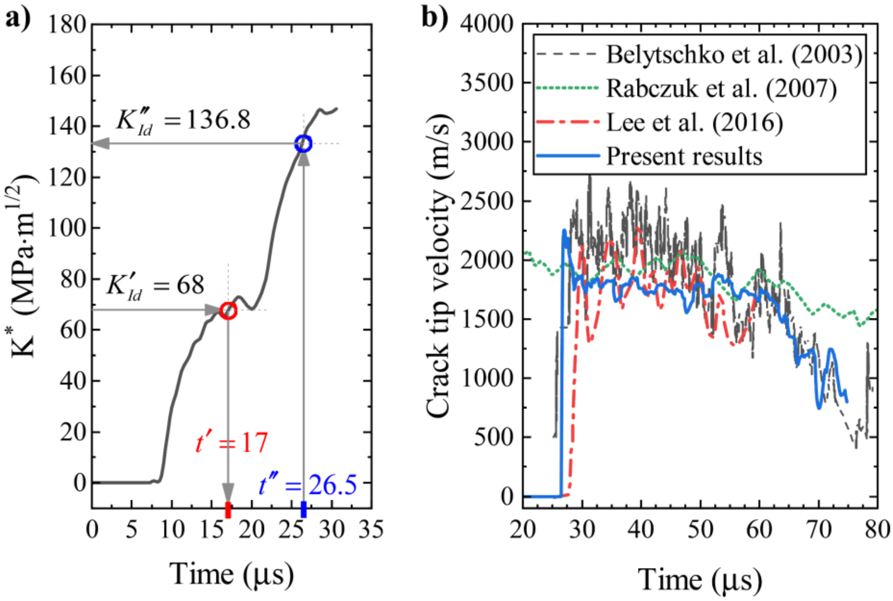

Figure 4.21. The Kalthoff-Winkler impact test: (a) variation over the time of the equivalent Stress Intensity Factors K* with no crack propagation mechanisms; (b) comparison in terms of the time histories of crack tip velocity between the present method and numerical predictions of Belytschko et al. (Belytschko et al., 2003), Rabczuk et al. (Rabczuk et al., 2010), and Lee et al (Lee et al., 2016).

pened at almost $t = 26.5\,\mu s$. Then, the crack tip velocity suddenly increases and oscillates within 1500 m/s and 2200 m/s for $40\,\mu s$. Finally, it progressively decreases, and the analysis stops around $t = 78\,\mu s$ since the crack front approaches the top boundary of the plate.

Proper calibrations of the dynamic crack initiation (K_{Id}) and arrest (K_{IA}) toughness, and the shape parameter m for defining the dynamic crack growth (K_{ID}) toughness (Eq. (4.34)) are necessary to reproduce the fracture behavior predicted by other Authors.

The requirement for a novel value for K_{Id} relies on the fact that the initial threshold $K_{Id} = 68\,MPa\sqrt{m}$ implies crack onset conditions occurring at $t' = 17\,\mu s$. This condition emerges from Figure 4.21-a, which depicts the variation over the time of the equivalent Stress Intensity Factors (K^*) evaluated through a numerical simulation of the plate without considering crack propagation events. In addition, Figure 4.21-a shows that K^* at $t'' = 26.5\,\mu s$ is equal to $K^* = 136.8\,MPa\sqrt{m}$. For this reason, it is assumed $K_{Id} = 136.8\,MPa\sqrt{m}$ in the numerical model to ensure crack onset conditions like those predicted by other Authors. The value of K_{IA} has been selected through a parametric study in terms of different values for K_{IA} lower than K_{Id}. Based on other numerical strategies, $K_{IA} = 54.7\,MPa\sqrt{m}$ provides the best fit with the results. Finally, m is assumed equal to 3.

Figure 4.21-b compares the time history of the crack tip velocity obtained by the proposed method with numerical results reported in Belytschko et al. (Belytschko et al., 2003), Rabczuk et al. (Rabczuk et al., 2010), and Lee et al. (Lee et al., 2016). The results show that the present procedure agrees well with the predictions of Rabczuk et al. (Rabczuk et al., 2010) and Lee et al. (Lee et al., 2016) because in the time interval comprised between *t*=30 μs and *t*=50 μs, the proposed method predicts an average velocity of about 1800 m/s, while the one of the other Authors oscillates around 2000 m/s (just over 11%). Within the same time interval, Belytschko et al. (Belytschko et al., 2003) achieve a crack tip velocity fluctuating around 2200 m/s, which is higher than that obtained by the present method of 22%. After this time interval, the curve of the proposed method and that achieved by Belytschko et al. (Belytschko et

al., 2003) match each other. In particular, in both cases, the crack tip velocity decreases from 1800 m/s to 1000 m/s.

These results demonstrate the applicability of the proposed method in evaluating the crack tip velocity for dynamically advancing crack fronts under mixed-mode fracture conditions.

5

CONCLUSIONS

The main goal of the present thesis was to develop a novel FE-based modeling approach for simulating crack propagation phenomena in homogeneous and heterogeneous structural materials under general loading conditions. In particular, the proposed method has been developed to simulate the failure behavior of material components because of thermo-mechanical actions in static and dynamic contexts.

The proposed modeling approach relies on the enhancement of a standard FE setting through a Moving Mesh (MM) technique consistent with the Arbitrary Lagrangian-Eulerian Formulation (ALE) for tracing the evolutions of the geometry domain caused by the growth of internal material defects.

The ALE formulation uses proper smoothing (or rezoning) equations that properly relocate mesh nodes during mesh motion, avoiding excessive distortions for the finite elements of the computational mesh. This feature ensures the consistency of the mesh nodes' movement, thus reducing the possibility of losses of accuracy issues in the numerical solution. Besides, unlike traditional FE-based procedures that reproduce crack propagation mechanisms by performing remeshing actions for each increment of the crack front, the ALE formulation updates the computational mesh exclusively when the finite elements suffer from relevant distortions. Such an aspect provides the significant benefit of reducing the overall amount of computational efforts.

In the proposed approach, the computational nodes around the crack front move according to the conditions dictated by classical fracture criteria developed in the context of Fracture Mechanics. Such criteria define the fundamental conditions for identifying crack onsetting, the propagation direction, and the crack propagating speed.

Such conditions are generally expressed in terms of fracture variables at the crack front, such as Stress Intensity Factors (SIFs). Consequently, a proper evaluation of the SIFs in static and dynamic conditions is essential to ensure reliable predictions of the fracture behavior of materials. To this end, the proposed model adopts the Interaction Integral method (i.e., the M-integral) to extract mixed-mode SIFs or dynamic SIFs (DSIFs) at the crack front. It is worth noting that the M-integral accuracy depends on the arrangement of the computational mesh in the region around the crack tip. Usually, fine and regular mesh configurations are necessary for ensuring accurate results. Because the proposed method alters the computational mesh during the crack propagation event, the ALE formulation of the *M*-integral is implemented. Hence, the integration is carried out on deforming elements because of the motion of the computational mesh. In particular, the ALE formulation of the *M*-integral permits extracting SIFs (or DSIFs) simultaneously as the crack front advances, thus obtaining smooth crack trajectories.

The proposed method has been implemented in the commercially available software COMSOL Multiphysics. This software has helpful apps that permit expanding the basic functionalities. Among the different apps available, the LiveLink for MATLAB platform has been used to define a homemade script code that automatically manages the several steps to reproduce crack propagation mechanisms inside the material (and then the motion of the computational mesh).

The validity of the proposed approach has been assessed by analyzing several benchmark cases. In particular, comparisons with alternative numerical methodologies, experimental predictions, and analytical data available in the literature have been performed. Besides, the robustness of the proposed model has been checked through sensitivity analyses in terms of mesh configurations and setting parameters involved in the M-integral method.

With reference to the obtained numerical results in terms of final crack trajectories, load versus displacement curves, extracted SIFs and DSIFs, and crack tip velocity, the following conclusions can be drawn:

- the proposed model is able to correctly reproduce the fracture behavior of material components in both static and dynamic frameworks;
- the results show that the proposed method is in good agreement with analytical solutions, experimental findings, and predictions provided by other numerical methodologies;
- the agreement with prominent experimental results reported in the literature concerning the crack tip velocity highlights the capabilities of the proposed strategy in reproducing the kinematics of dynamic crack propagation processes;
- unlike existing formulations available in the literature, the ALE formulation, through rezoning methods, considerably reduces the recourse to re-meshing actions, which typically involve substantial computational costs;
- parametric analyses have revealed that the proposed approach ensures acceptable accuracy in numerical predictions and excellent computational efficiency;
- the proposed model avoids the finer mesh discretization for the entire computational domain. In fact, the proposed method permits using mesh configuration with refined zones only around the crack tip regions, leaving the remaining zones coarser. It represents a valid strategy to reduce the weaknesses of standard

FEM procedures, in terms of numerical complexities and computational efforts;

- the ALE formulation of the *M*-integral extends the advantages of classic *M*-integral method (e.g., accuracy and easiness of use) to the case of moving computational mesh, thus avoiding the necessity of extremely regular discretization.

- finally, the proposed methodology represents a simple and robust approach to reproduce complex crack propagation mechanisms in articulated geometries.

5.1 Future perspectives

As future perspectives of this thesis, the following research directions could be explored:

- in the current form, the proposed method reproduces the evolution of pre-existing cracks inside the material. Then, it can effectively perform failure analysis of fractured materials. An important improvement could be the implementation of a proper strategy for identifying the location of potential failure starting from an intact material. Such a possible additional functionality could permit analyzing the behavior of a structural system, from the undamaged status up to the complete failure;

- extension of the proposed fracture approach for analyzing crack propagation mechanisms in 3D geometries;

- regarding dynamic fracture mechanics, the capabilities of the proposed method could be extended to reproduce crack branching phenomena, which usually occur in quasi-brittle materials when the crack tip velocity reaches about 60% of the Rayleigh wave speed.

Bibliography

Ai, W., Augarde, C.E., 2019. Thermoelastic fracture modelling in 2D by an adaptive cracking particle method without enrichment functions. International Journal of Mechanical Sciences 160, 343–357. https://doi.org/10.1016/j.ijmecsci.2019.06.033

Ai, W., Bird, R.E., Coombs, W.M., Augarde, C.E., 2019. A configurational force driven cracking particle method for modelling crack propagation in 2D. Engineering Analysis with Boundary Elements 104, 197–208. https://doi.org/10.1016/j.enganabound.2019.03.008

Ammendolea, D., Greco, F., Lonetti, P., Luciano, R., Pascuzzo, A., 2021. Crack propagation modeling in functionally graded materials using Moving Mesh technique and interaction integral approach. Composite Structures 269, 114005. https://doi.org/10.1016/j.compstruct.2021.114005

Anderson, Ted L., Anderson, T. L., 2005. Fracture Mechanics: Fundamentals and Applications, Third Edition, 3rd ed. CRC Press, Boca Raton. https://doi.org/10.1201/9781420058215

Barretta, R., Luciano, R., Willis, J.R., 2015. On torsion of random composite beams. Composite Structures 132, 915–922. https://doi.org/10.1016/j.compstruct.2015.06.069

Baton, U.N., 1986. Advanced fracture mechanics,by M. F. Kanninen and C. H. Popelar. Strain 22, 83–83. https://doi.org/10.1111/j.1475-1305.1986.tb00597.x

Bayesteh, H., Mohammadi, S., 2013. XFEM fracture analysis of orthotropic functionally graded materials. Composites Part B: Engineering 44, 8–25. https://doi.org/10.1016/j.compositesb.2012.07.055

Bazant, Z.P., Planas, J., 2019. Fracture and Size Effect in Concrete and Other Quasibrittle Materials. Routledge, New York. https://doi.org/10.1201/9780203756799

Belytschko, T., Black, T., 1999. Elastic crack growth in finite elements with minimal remeshing. International Journal for Numerical Methods in Engineering 45, 601–620. https://doi.org/10.1002/(SICI)1097-0207(19990620)45:5<601::AID-NME598>3.0.CO;2-S

Belytschko, T., Chen, H., Xu, J., Zi, G., 2003. Dynamic crack propagation based on loss of hyperbolicity and a new discontinuous enrichment. International Journal for Numerical Methods in Engineering 58, 1873–1905. https://doi.org/10.1002/nme.941

Belytschko, T., Tabbara, M., 1996. Dynamic Fracture Using Element-Free Galerkin Methods. International Journal for Numerical Methods in Engineering 39, 923–938. https://doi.org/10.1002/(SICI)1097-0207(19960330)39:6<923::AID-NME887>3.0.CO;2-W

Bouhala, L., Makradi, A., Belouettar, S., 2012. Thermal and thermo-mechanical influence on crack propagation using an extended mesh free method. Engineering Fracture Mechanics 88, 35–48. https://doi.org/10.1016/j.engfracmech.2012.04.001

Chen, H., Wang, Q., Liu, G.R., Wang, Y., Sun, J., 2016. Simulation of thermoelastic crack problems using singular edge-based smoothed finite element method. International Journal of Mechanical Sciences 115–116, 123–134. https://doi.org/10.1016/j.ijmecsci.2016.06.012

Chen, H., Wang, Q., Zeng, W., Liu, G.R., Sun, J., He, L., Bui, T.Q., 2019. Dynamic brittle crack propagation modeling using singular edge-based smoothed finite element method with local mesh rezoning. European Journal of Mechanics - A/Solids 76, 208–223. https://doi.org/10.1016/j.euromechsol.2019.04.010

Cheng, A.H.-D., Cheng, D.T., 2005. Heritage and early history of the boundary element method. Engineering Analysis with Boundary Elements 29, 268–302. https://doi.org/10.1016/j.enganabound.2004.12.001

Cherradi, N., Kawasaki, A., Gasik, M., 1994. Worldwide trends in functional gradient materials research and development. Composites Engineering 4, 883–894. https://doi.org/10.1016/S0961-9526(09)80012-9

Clough, R., 1960. The Finite Element Method in Plane Stress Analysis.

Dai, S., Augarde, C., Du, C., Chen, D., 2015. A fully automatic polygon scaled boundary finite element method for modelling crack propagation. Engineering Fracture Mechanics 133, 163–178. https://doi.org/10.1016/j.engfracmech.2014.11.011

Erdogan, F., Sih, G.C., 1963. On the Crack Extension in Plates Under Plane Loading and Transverse Shear. Journal of Basic Engineering 85, 519–525. https://doi.org/10.1115/1.3656897

Freund, L.B., 1990. Dynamic Fracture Mechanics, Cambridge Monographs on Mechanics. Cambridge University Press, Cambridge. https://doi.org/10.1017/CBO9780511546761

Freund, L.B., Clifton, R.J., 1974. On the uniqueness of plane elastodynamic solutions for running cracks. J Elasticity 4, 293–299. https://doi.org/10.1007/BF00048612

Funari, M.F., Greco, F., Lonetti, P., 2018a. Sandwich panels under interfacial debonding mechanisms. Composite Structures 203, 310–320. https://doi.org/10.1016/j.compstruct.2018.06.113

Funari, M.F., Greco, F., Lonetti, P., Luciano, R., Penna, R., 2018b. An interface approach based on moving mesh and cohesive modeling in Z-pinned composite laminates. Composites Part B: Engineering 135, 207–217. https://doi.org/10.1016/j.compositesb.2017.10.018

Greco, F., Ammendolea, D., Lonetti, P., Pascuzzo, A., 2021. Crack propagation under thermo-mechanical loadings based on moving mesh strategy. Theoretical and Applied Fracture Mechanics 114, 103033. https://doi.org/10.1016/j.tafmec.2021.103033

Greco, F., Lonetti, P., 2009. Mixed mode dynamic delamination in fiber reinforced composites. Composites Part B: Engineering 40, 379–392. https://doi.org/10.1016/j.compositesb.2009.03.003

Grégoire, D., Maigre, H., Réthoré, J., Combescure, A., 2007. Dynamic crack propagation under mixed-mode loading – Comparison between experiments and X-FEM simulations. International Journal of Solids and Structures 44, 6517–6534. https://doi.org/10.1016/j.ijsolstr.2007.02.044

Hussain, M.A., Pu, S.L., Underwood, J., n.d. Strain Energy Release Rate for a Crack Under Combined Mode I and Mode II, in: Fracture Analysis: Proceedings of the 1973 National Symposium on Fracture Mechanics, Part II. Presented at the National Symposium on Fracture Mechanics, ASTM International, pp. 2–28. https://doi.org/10.1520/STP33130S

Jin, Z.-H., Paulino, G.H., Dodds, R.H.,. Jr.,., 2002. Finite Element Investigation of Quasi-Static Crack Growth in Functionally Graded Materials Using a Novel Cohesive Zone Fracture Model. Journal of Applied Mechanics 69, 370–379. https://doi.org/10.1115/1.1467092

Kalthoff, J., Beinert, J., Winkler, S., 1977. Measurements of Dynamic Stress Intensity Factors for Fast Running and Arresting Cracks in Double-Cantilever-Beam Specimens 161-161–16. https://doi.org/10.1520/STP27387S

KANDULA, S.S.V., ABANTO-BUENO, J., GEUBELLE, P.H., LAMBROS, J., 2005. Cohesive modeling of dynamic fracture in functionally graded materials. Int J Fract 132, 275–296. https://doi.org/10.1007/s10704-005-1207-0

Kim, J.-H., Paulino, G.H., 2007. On Fracture Criteria for Mixed-Mode Crack Propagation in Functionally Graded Materials. Mechanics of Advanced Materials and Structures 14, 227–244. https://doi.org/10.1080/15376490600790221

Kim, J.-H., Paulino, G.H., 2004a. Simulation of Crack Propagation in Functionally Graded Materials Under Mixed-Mode and Non-Proportional Loading. Mechanics and Materials in Design 1, 63–94. https://doi.org/10.1023/B:MAMD.0000035457.78797.c5

Kim, J.-H., Paulino, G.H., 2004b. Consistent Formulations of the Interaction Integral Method for Fracture of Functionally Graded Materials. Journal of Applied Mechanics 72, 351–364. https://doi.org/10.1115/1.1876395

Kim, J.-H., Paulino, G.H., 2003. T-stress, mixed-mode stress intensity factors, and crack initiation angles in functionally graded materials: a unified approach using the interaction integral method. Computer Methods in Applied Mechanics and Engineering 192, 1463–1494. https://doi.org/10.1016/S0045-7825(02)00652-7

Koh, H.M., Lee, H.S., Haber, R.B., 1988. Dynamic crack propagation analysis using Eulerian-Lagrangian kinematic descriptions. Computational Mechanics 3, 141–155. https://doi.org/10.1007/BF00297441

Kuna, M., 2013. Finite Elements in Fracture Mechanics, Solid Mechanics and Its Applications. Springer Netherlands, Dordrecht. https://doi.org/10.1007/978-94-007-6680-8

Lee, S.-H., Kim, K.-H., Yoon, Y.-C., 2016. Particle difference method for dynamic crack propagation. International Journal of Impact Engineering, SI: Experimental Testing and Computational Modeling of Dynamic Fracture 87, 132–145. https://doi.org/10.1016/j.ijimpeng.2015.06.001

Liao, M., Deng, X., Guo, Z., 2018. Crack propagation modelling using the weak form quadrature element method with minimal remeshing. Theoretical and Applied Fracture Mechanics 93, 293–301. https://doi.org/10.1016/j.tafmec.2017.09.012

Menouillard, T., Belytschko, T., 2010. Smoothed nodal forces for improved dynamic crack propagation modeling in XFEM. International Journal for Numerical Methods in Engineering 84, 47–72. https://doi.org/10.1002/nme.2882

Menouillard, T., Song, J.-H., Duan, Q., Belytschko, T., 2010. Time dependent crack tip enrichment for dynamic crack propagation. Int J Fract 162, 33–49. https://doi.org/10.1007/s10704-009-9405-9

Moës, N., Belytschko, T., 2002. Extended finite element method for cohesive crack growth. Engineering Fracture Mechanics 69, 813–833. https://doi.org/10.1016/S0013-7944(01)00128-X

Moran, B., Shih, C.F., 1987. Crack tip and associated domain integrals from momentum and energy balance. Engineering Fracture Mechanics 27, 615–642. https://doi.org/10.1016/0013-7944(87)90155-X

Nilsson, F., 1974. A note on the stress singularity at a non-uniformly moving crack tip. J Elasticity 4, 73–75. https://doi.org/10.1007/BF00042404

Ooi, E.T., Natarajan, S., Song, C., Tin-Loi, F., 2015. Crack propagation modelling in functionally graded materials using scaled boundary polygons. Int J Fract 192, 87–105. https://doi.org/10.1007/s10704-015-9987-3

Ooi, E.T., Shi, M., Song, C., Tin-Loi, F., Yang, Z.J., 2013. Dynamic crack propagation simulation with scaled boundary polygon elements and automatic remeshing technique. Engineering Fracture Mechanics 106, 1–21. https://doi.org/10.1016/j.engfracmech.2013.02.002

Ooi, E.T., Song, C., Tin-Loi, F., Yang, Z., 2012. Polygon scaled boundary finite elements for crack propagation modelling. International Journal for Numerical Methods in Engineering 91, 319–342. https://doi.org/10.1002/nme.4284

Ponthot, J.-P., Belytschko, T., 1998. Arbitrary Lagrangian-Eulerian formulation for element-free Galerkin method. Computer Methods in Applied Mechanics and Engineering, Containing papers presented at the Symposium on Advances in Computational Mechanics 152, 19–46. https://doi.org/10.1016/S0045-7825(97)00180-1

Prasad, N.N.V., Aliabadi, M.H., Rooke, D.P., 1994. Incremental crack growth in thermoelastic problems. International Journal of Fracture 66, R45–R50.

Rabczuk, T., Zi, G., Bordas, S., Nguyen-Xuan, H., 2010. A simple and robust three-dimensional cracking-particle method without enrichment. Computer Methods in Applied Mechanics and Engineering 199, 2437–2455. https://doi.org/10.1016/j.cma.2010.03.031

Rice, J., 1968. Mathematical analysis in the mechanics of fracture.

Rousseau, C.-E., Tippur, H.V., 2000. Compositionally graded materials with cracks normal to the elastic gradient. Acta Materialia 48, 4021–4033. https://doi.org/10.1016/S1359-6454(00)00202-0

Shahani, A.R., Amini Fasakhodi, M.R., 2009. Finite element analysis of dynamic crack propagation using remeshing technique. Materials & Design 30, 1032–1041. https://doi.org/10.1016/j.matdes.2008.06.049

Shen, H.-S., 2009. Functionally Graded Materials: Nonlinear Analysis of Plates and Shells. CRC Press, Boca Raton. https://doi.org/10.1201/9781420092578

Shih, C.F., Moran, B., Nakamura, T., 1986. Energy release rate along a three-dimensional crack front in a thermally stressed body. Int J Fract 30, 79–102. https://doi.org/10.1007/BF00034019

Sih, G.C., 1962. On the Singular Character of Thermal Stresses Near a Crack Tip. Journal of Applied Mechanics 29, 587–589. https://doi.org/10.1115/1.3640612

Steigemann, M., Specovius-Neugebauer, M., Fulland, M., Richard, H.A., 2010. Simulation of crack paths in functionally graded materials. Engineering Fracture Mechanics, International Conference on Crack Paths 2009 77, 2145–2157. https://doi.org/10.1016/j.engfracmech.2010.03.022

Tilbrook, M.T., Moon, R.J., Hoffman, M., 2005. Finite element simulations of crack propagation in functionally graded materials under flexural loading. Engineering Fracture Mechanics 72, 2444–2467. https://doi.org/10.1016/j.engfracmech.2005.04.001

Tilbrook, M.T., Rozenburg, K., Steffler, E.D., Rutgers, L., Hoffman, M., 2006. Crack propagation paths in layered, graded composites. Composites Part B: Engineering, JCOM 731 " Nanoengineered composites and Ceramic Laminates" Special Issue 37, 490–498. https://doi.org/10.1016/j.compositesb.2006.02.012

Tomlinson, R.A., Olden, E.J., 1999. Thermoelasticity for the analysis of crack tip stress fields — a review. Strain 35, 49–55. https://doi.org/10.1111/j.1475-1305.1999.tb01125.x

Yan, F., Zhang, W., Pan, P.-Z., Li, S.-J., 2021. Dynamic crack propagation analysis combined the stable scheme and continuous-discontinuous cellular automaton. Engineering Fracture Mechanics 241, 107390. https://doi.org/10.1016/j.engfracmech.2020.107390

Yang, Z.J., Wang, X.F., Yin, D.S., Zhang, C., 2015. A non-matching finite element-scaled boundary finite element coupled method for linear elastic crack propagation modelling. Computers & Structures 153, 126–136. https://doi.org/10.1016/j.compstruc.2015.02.034

Yau, J.F., Wang, S.S., Corten, H.T., 1980. A Mixed-Mode Crack Analysis of Isotropic Solids Using Conservation Laws of Elasticity. Journal of Applied Mechanics 47, 335–341. https://doi.org/10.1115/1.3153665

Yu, H., Kuna, M., 2021. Interaction integral method for computation of crack parameters K–T – A review. Engineering Fracture Mechanics 249, 107722. https://doi.org/10.1016/j.engfracmech.2021.107722

Yu, H., Wu, L., Guo, L., Du, S., He, Q., 2009. Investigation of mixed-mode stress intensity factors for nonhomogeneous materials using an interaction integral method. International Journal of Solids and Structures 46, 3710–3724. https://doi.org/10.1016/j.ijsolstr.2009.06.019